

Dorian S. H. Brandmüller, BSc

Evaluation of acoustical resolution photoacoustic microscopy: Simulations and experiments

MASTER'S THESIS

to achieve the university degree of

Diplom-Ingenieur

Master's degree programme: Technical Physics

submitted to

Graz University of Technology

Supervisor

Mag. Dr.rer.nat Robert Nuster

Institute of physics

University of Graz

Graz, August 2021

AFFIDAVIT

I declare that I have authored this thesis independently, that I have not used other than the declared sources/resources, and that I have explicitly indicated all material which has been quoted either literally or by content from the sources used. The text document uploaded to TUGRAZonline is identical to the present master's thesis.

Date, Signature

Abstract

Imaging techniques are of great importance in biomedical sciences, especially in medicine to investigate different kinds of diseases. Most of the known methods are either costly to use, limited by their depth of penetration, or have to resort to ionizing radiation to overcome these constraints. Instead, photoacoustic imaging combines the contrast achieved by the absorption of intensity modulated light with the resolution that results from the detection of ultrasonic waves from deep tissue regions.

The possibility of addressing a wide variety of absorbing chromophores in the sample through the targeted selection of the excitation wavelength not only allows the sample specific composition to be quantified but also to extract functional information such as the oxygen level in biological samples.

The goal of this work is the evaluation of acoustical resolution photoacoustic microscopy (AR-PAM) using simulations and experiments. A special focus is put on the possibility to image comparatively small blood vessels in liver tissue.

First, a review of the theory in general was conducted, considering the differences between PAM implementations. This theoretical background was then used to implement algorithms for the simulation of the full problem, including light and acoustic wave propagation, signal post-processing and image reconstruction.

A Monte-Carlo algorithm was used to investigate the propagation of light in turbid media and thereby calculate the absorption of energy by different samples depending on the used wavelength.

Further, a free-to-use Matlab toolbox (k-wave) was used to perform acoustic wave propagation simulations, which lead to signals representing those of a real experiment. Another program was written to correct some of the most common artifacts.

Some of the results gained from these simulations were checked against experimentally attained data. The outcomes of these experiments comply with the knowledge gained from the simulations to a large degree.

Kurzzusammenfassung

Bildgebende Verfahren spielen in den Biowissenschaften eine entscheidende Rolle, speziell in der Medizin, wo sie zur Untersuchung von Krankheiten genutzt werden. Die meisten bekannten Methoden sind entweder kostenintensiv, leiden unter einer geringen Eindringtiefe oder müssen auf ionisierende Strahlung zurückgreifen, um diese Einschränkungen zu überwinden. Stattdessen kombiniert die photoakustische Bildgebung den Kontrast, welcher durch die Absorption von intensitätsmoduliertem Licht ermöglicht wird, mit der Auflösung, welche durch die Detektion von Ultraschallwellen aus tiefen Gewebeschichten erreicht wird.

Die Möglichkeit viele verschiedene absorbierende Chromophore in einer Probe, durch die gezielte Wahl einer Wellenlänge, anzuregen, erlaubt es, nicht nur die probenspezi-

fische Zusammensetzung zu analysieren, sondern auch funktionale Informationen zu extrahieren, zum Beispiel den Sauerstoffgehalt in biologischen Proben.

Das Ziel der vorliegenden Arbeit ist die Beurteilung von akustisch aufgelöster photoakustischer Mikroskopie (AR-PAM) mittels Simulationen und Experimenten. Der Fokus liegt dabei auf der Abbildung von vergleichsweise kleinen Blutgefäßstrukturen in Lebergewebe.

Zuerst wurde ein Überblick über die allgemeine Theorie gegeben, wobei Unterschiede zwischen den PAM Implementationen hervorgehoben wurden. Dieser theoretische Hintergrund wurde danach genutzt, um Algorithmen zu implementieren, mit welchen das komplette Problem simuliert werden konnte.

Ein Monte-Carlo Algorithmus wurde implementiert, damit die Lichtausbreitung in trüben Medien untersucht und die Energieabsorption verschiedener Proben, abhängig von der genutzten Wellenlänge, berechnet werden konnte.

Danach wurde eine free-to-use Matlab Toolbox (k-wave) genutzt, um Simulationen der Ausbreitung von akustischen Wellen zu berechnen. Diese führten zu Signalen, welche sich mit Datensätzen aus Experimenten vergleichen ließen. Ein weiteres Programm, zur Korrektur von verfahrensbedingten Artefakten, wurde ebenfalls geschrieben.

Einige der dadurch gewonnenen Ergebnisse wurden durch Experimente überprüft. Die Resultate dieser Experimente stimmen zu einem großen Grad mit jenen der Simulationen überein.

Acknowledgment

First, I would like to thank my supervisor Dr. Robert Nuster, who has, beginning with my Bachelor's thesis in 2019, lead my way into the world of research and photoacoustics especially. Having an experienced scientist by my side, who is as focused on doing good scientific work as he is fascinated by unexpected results, has proven to be the greatest motivation during the work on this thesis.

Further, I am eternally grateful for my friends and family. Especially my parents, who made it possible for me to study without major concerns, supporting me not only financially but also morally and in every other fathomable way.

Being a friend of mine might be exasperating at times and I therefore thank everyone who held on until now. I sadly can not promise any improvement in the future. I would like to use the opportunity to point out Dr. Jochen Schachenreiter and Dr. Dieter Krainz, who have been dear friends of mine for many years and have supported me in my early and earliest education, respectively.

This work has received funding from the Austrian Research Promotion Agency (FFG, Project: OMiPPAB, No. 877103)

Contents

1. Introduction and Motivation	1
2. Theory of photoacoustic imaging techniques	5
2.1. Light matter interaction	5
2.1.1. Optical coefficients	8
2.2. Numerical treatment of light propagation	9
2.2.1. Initialization and step size	10
2.2.2. Photon movement, absorption and scattering	11
2.2.3. Photon termination	12
2.3. The wave equation	15
2.4. Numerical treatment of the wave propagation using the k-space pseudospectral method	17
2.4.1. k-space pseudospectral method	17
2.4.2. Solving first order equations on a staggered grid	18
2.4.3. Perfectly matched layer	19
2.5. Photoacoustic microscopy	20
2.5.1. Spatial resolution of PAM-systems	24
2.6. Resolution limitation caused by focusing	25
2.6.1. Origin of artifacts	26
2.6.2. Correction of the artifacts	27
3. Simulations for photoacoustic microscopy	33
3.1. Monte-Carlo algorithm for light propagation in turbid media	34
3.1.1. Implementation of the algorithm	34
3.1.2. Discussion of selected simulations	38
3.2. Wave propagation simulation using the k-wave toolbox	41
3.2.1. Implementation of the method	44
3.2.2. Exemplary simulations	48
3.2.3. Comparison of a simulated signal with a measured signal	50
3.3. Artifact correction using a Fourier domain algorithm	52
3.3.1. Implementation of the algorithm into the existing framework	53
3.3.2. Exemplary reconstruction of simulated data	53
3.4. Results of complete simulations	55
3.4.1. Complete simulation	56
3.4.2. Focused sensor	60
3.4.3. Depth dependence for planar sensor	64

3.4.4. Negative contrast	65
4. Experimental study of photoacoustic microscopy	67
4.1. Experimental setup	67
4.1.1. Beam characterization	70
4.2. Measurements and evaluation	71
4.2.1. Initial measurement on an artificial leaf	72
4.2.2. Resolution characterization	73
4.2.3. Evaluation of reconstruction algorithm	75
4.2.4. Investigation of the multispectral capabilities	77
4.2.5. In vivo experiments	78
5. Conclusion and outlook	83
A. Measurement class	85
B. Fourier Domain reconstruction algorithm	89

1. Introduction and Motivation

The field of photoacoustics is a vast one. It can be divided into many areas, each with their own peculiarities and applications. Although each of these areas has their unique properties and therefore also the motivation differs between them in detail, which will become apparent during the examination of some of them, they all rely on the same principle. This principle can be easily deduced by an analysis of its name.

The two parts the name is made up of are “photo” on the one hand, which stems from the Greek word for light, and acoustics on the other hand, which can be traced back to mean “hearing” in Greek. These fields in physics are normally not thought of as belonging together. The first one is most often described by the theories on electromagnetism, while the latter, assuming some restrictions, can be described by classical mechanics.

Bringing those two fields together is a concept first thought of by Alexander Graham Bell in 1880. He invented the so-called photophone, a device capable of transmitting sound signals (like spoken words) over vast distances, aided by their conversion into light signals. This was achieved by modulating a light source by a mirror attached to a mouthpiece. The vibrations created by speaking into this contraption cause a change in the light intensity, which can be propagated over a long range. The detection was then performed by focusing this signal onto some absorbing material, inducing vibrations, which directly correspond to sound. These vibrations were either heard directly or were transformed into electrical signals [1]. Figure 1.1 represents a schematic of the setup used by Bell.

A more detailed description of the underlying physical effects will be given later on. It is nevertheless instructional to start with a rough explanation: When the light, which in the experiments conducted by Bell most often came from the sun, hit the absorbing material, its energy was converted to heat by means of the thermoelastic effect. If this happens rather rapidly, the process is adiabatic, which means that the generated heat cannot escape the material. This inevitably leads to an expansion of the material that in turn, considering the intensity modulation of the light, yields the needed vibrations. This effect is the most fundamental principle of all photoacoustic methods.

The discoveries of Bell in 1880 have since then led to a lot of research in different areas of physics. One large part of this research is photoacoustic spectroscopy, which will not be examined further but should be mentioned, nevertheless. This technique mainly consists of using different wavelengths of light to excite a material and examining the materials response. Since various materials react differently to a range of frequencies, a spectroscopic examination can be performed by measuring the thereby generated soundwaves. This can be used to characterize materials [2].

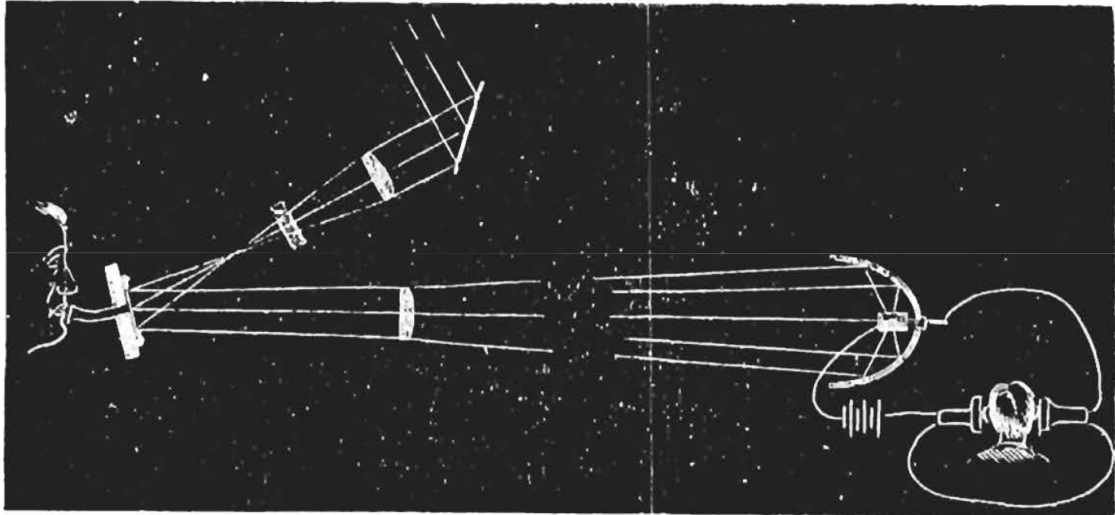


Figure 1.1.: *Schematic drawing of Bells photophone [1].*

The main topic of this thesis however, are techniques which yield an image, the focus lying on photoacoustic microscopy. These image acquisition techniques are summarized under the term of photoacoustic imaging (PAI), where the spectroscopic properties of the material are combined with the high resolution made possible by ultrasound detection. Thereby the contrast between the materials can be made visible. The resolution of such approaches depends on the exact method used but can generally go down to the micrometer regime. One of the main advantages of PAI compared to conventional ultrasound or optical techniques is the combination of this fine resolution with a large penetration depth in turbid media such as biological tissue [3].

Further, parameters, otherwise inaccessible by different methods, can be examined. It is for example possible to determine the blood oxygenation level, which changes the absorption of certain wavelengths of light. Assumptions on blood flow and temperature can also be made from PA measurements. The application in medicine is aided by the non-destructive non-ionizing radiation, which is being used, contrary to some more widely known methods including the use of x-rays. PAI experiments are mainly conducted using light generated by lasers in a wide range of wavelengths, mostly staying under the ANSI¹ limits for the fluence when working with biological materials [3].

A further advantage of PAI lies in the possibility to capture three dimensional images quite easily. One way to achieve this is by utilizing photoacoustic tomography (PAT). This method relies on the excitation of a large volume in the sample and more or less complex detector setups to measure the generated soundwaves. One way to detect the signals is using a full-field approach exploiting a phase plate and a CCD-camera to visualize differences in the refractive index of water, stemming from the propagating waves. The thereby generated pictures can be seen as Radon transformations of the pressure dis-

¹Americal National Standards Institute

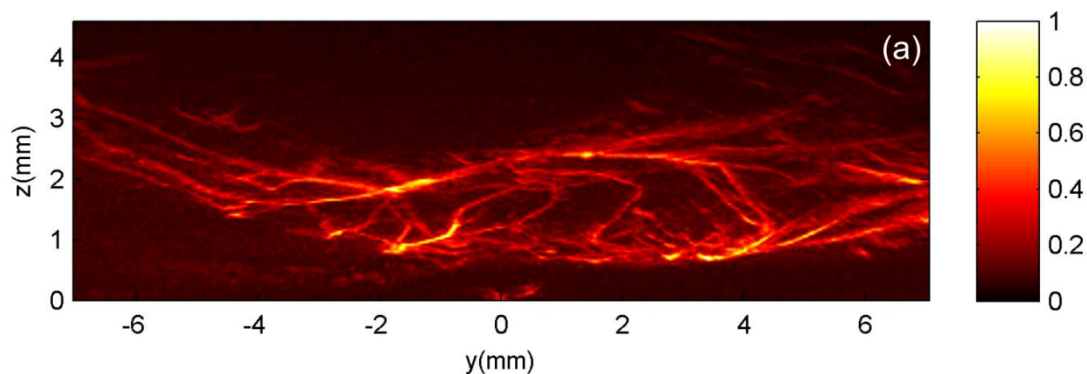


Figure 1.2.: *Maximum amplitude projection of the hind leg of an imaged mouse, using a full field CCD-camera ultrasound detection approach [5].*

tribution. Several reconstruction algorithms can be employed to gain the initial pressure distribution [4]. The results of such a measurement can be seen in figure 1.2.

Photoacoustic microscopy (PAM), on the other hand, relies on the excitation of small areas inside of the sample and some sort of focusing, which can either be achieved by a tightly focused beam (optical resolution PAM [OR-PAM]) or by a tightly focused acoustic sensor (acoustic resolution PAM [AR-PAM]). While two dimensions of the final data set are usually gained by scanning the sensor and the excitation source over the sample in one way or another, the third dimension is directly correlated to the time domain of the measured signals [3].

In theory, this approach is less demanding than a complicated PAT setup, since the reconstruction is more fundamental, which is a benefit. However, there are some difficulties when considering the focus of the setup. As with all imaging setups, this focus is only optimal in a very narrow region (strictly speaking only in the focus plane), features lying outside of this region will produce artifacts, which call for reconstruction algorithms [3]. Simulating these measurements and implementing algorithms for a quick and efficient correction of the artifacts is one main goal of this thesis. Further, the results were compared against experiments.

The overall goal of this thesis is the investigation of the possibility to image biological tissue. A special focus was put on human organs such as the human liver. These organs often get transplanted, because this posts the only viable treatment option for some diseases, and are subject to some deterioration during the time outside of the body. Gaining a deeper insight into this quality loss would provide a large benefit in medicine, since some conclusions could be made on how to extend the life-time of these organs.

This thesis summarizes the first steps, which had to be taken in order to develop a system that works in a clinical environment. In the end, this should provide some knowledge for the interdisciplinary project titled "OMiPPAB" that started in 2020. This project is set at the intersection of physics, medicine and industry, combining everything necessary for the development of a fully functioning setup, from the scientific ground work, which was the main target of this thesis, to the setup ready for clinical tests.

2. Theory of photoacoustic imaging techniques

In this chapter the focus will be put on the theoretical background of photoacoustic imaging techniques. The fundamentals, which were already mentioned in the introduction, are the same for all measurement techniques and will therefore be discussed in the beginning. Since computer simulations play an essential role in this thesis, an analysis of the numerical treatments of the underlying physical effects should be given as well as some insight into the analytical problems. Coming from this broad background it will be possible to narrow down on the specific problems at hand and show how the discussed theory is applied in more defined applications and use cases.

The principle of all PAI techniques can be most easily explained in four steps:

1. The excitation of the sample is performed using an intense light source, in most cases this is done by a laser (1 in figure 2.1).
2. This light gets absorbed. Depending on the exact properties of the material, which differ for different regions (e.g. liver tissue and blood vessels), more or less energy gets stored inside of the material.
3. If the above process happens fast enough (stress and thermal confinement are fulfilled), the stored energy will cause an increase in temperature and therefore a rise in pressure. This will ultimately lead to the generation of sound waves.
4. These sound waves can be detected and analyzed in various ways, giving the opportunity to generate images (2 and 3 in figure 2.1).

These steps are shown schematically in figure 2.1.

2.1. Light matter interaction

The first thing, which shall be discussed is the interaction of light with matter and how constants can be defined, which influence it. The main interest lies within the physical transfer of energy through a medium caused by electromagnetic radiation. This is usually described as *radiative transfer*. There are three phenomena which influence this propagation of light: Emission, absorption and scattering [7]. A simple depiction of these processes is shown in figure 2.2. Emission is an additive process which converts energy stored within the material (energy conservation has to be fulfilled) into radiation and therefore strengthens the radiation field. Absorption, on the other hand, is responsible

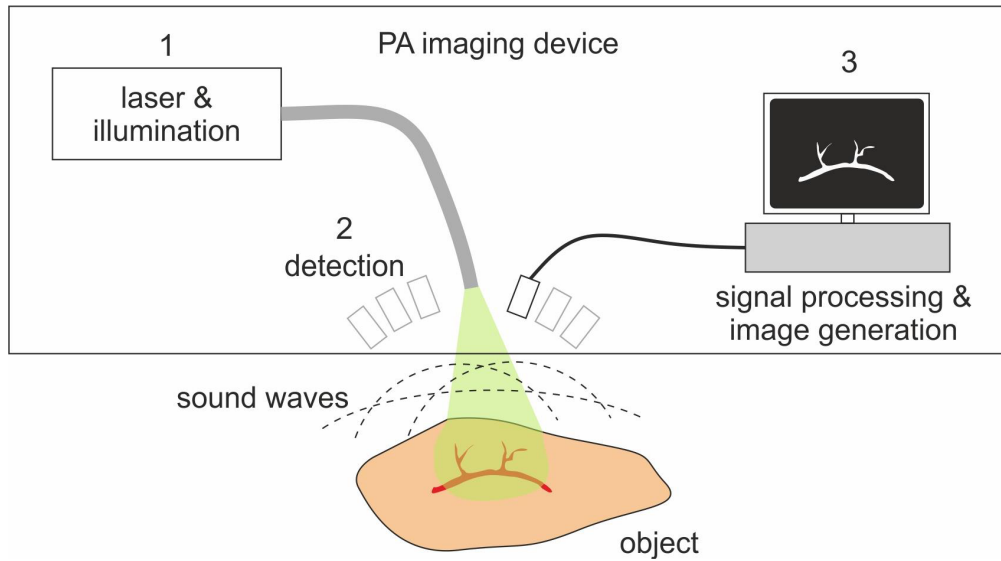


Figure 2.1.: *Schematic of the general process used by photoacoustic imaging devices [6].*

for the inverse effect. It describes the reduction of the radiative energy through its absorption into the material by a conversion to other forms of energy. This conversion, to heat for example, is a key part of the photoacoustic effect. The third part, scattering, can be seen as a redistribution of energy. Depending on the direction the light is scattered into, it can either strengthen the beam in question or weaken it. When talking about a laser beam propagating through a turbid medium, as in the case of most photoacoustic applications, scattering is responsible for the widening of the beam inside of the material, which yields a characteristic pear shape, of the absorbed energy.

An example of such an interaction of light with matter can be seen in figure 2.3, where a strong flashlight was shone through a hand. The beam was attenuated by a large amount and scattering took place. Although being only a rough experiment, it shows some blood vessels in the hand, which leads to the conclusion that these structures have different optical properties than the rest of the tissue.

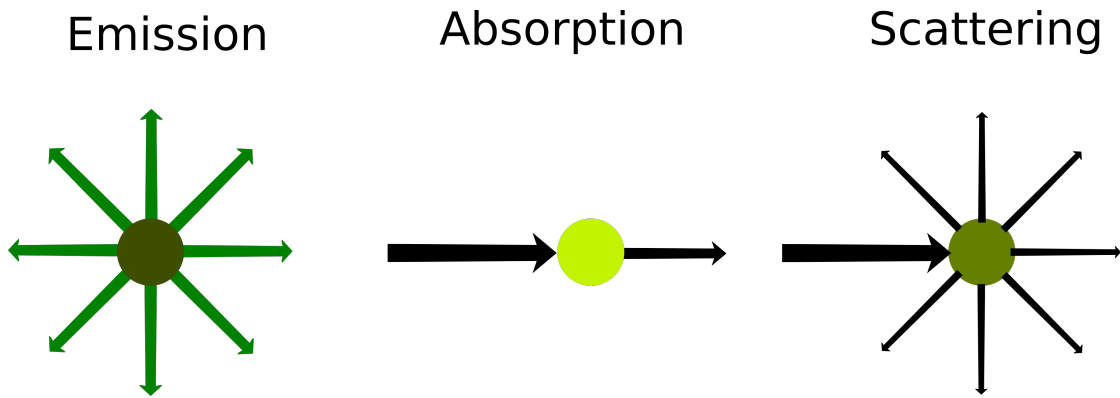


Figure 2.2.: *Schematic of the general processes happening during the interaction of light with matter.*



Figure 2.3.: *Picture of a flashlight shining through a hand.*

All of the above effects can be combined into one differential equation, which describes the whole process [8]:

$$\frac{\partial I_{\mathbf{v}}(\mathbf{r}, t)}{\partial t} + \nabla_{\mathbf{v}} I_{\mathbf{v}}(\mathbf{r}, t) + \left(\frac{1}{\tau_{abs}} + \frac{1}{\tau_{scat}} \right) I_{\mathbf{v}}(\mathbf{r}, t) = S(\mathbf{r}, t) + \int d\hat{\mathbf{v}}' W(\mathbf{v}, \mathbf{v}') I_{\mathbf{v}'}. \quad (2.1)$$

$I_{\mathbf{v}}(\mathbf{r}, t)$ is the specific intensity of the photon flow at position \mathbf{r} and time t , with a velocity $\mathbf{v} = c\hat{\mathbf{v}}$. The propagation is described by the first two terms on the left side, the absorption rate is given by $\frac{1}{\tau_{abs}}$ while the scattering rate to other directions is given by $\frac{1}{\tau_{scat}}$. $S(\mathbf{r}, t)$ describes the emission and $W(\mathbf{v}, \mathbf{v}')$ the scattering coming from other directions per solid angle [8].

This so-called *radiative transfer equation* can be solved analytically for some special cases. Especially when looking at homogeneous media and omitting scattering, solutions can be found. These calculations are cumbersome and are of no real benefit regarding the tasks discussed in this thesis. Therefore, only a source for such calculations will be given: S. Chandrasekhar. *Radiative Transfer* (1960) [7].

2.1.1. Optical coefficients

Since an analytical examination of the problem at hand has proven to be very difficult, if not impossible for the goal of this thesis, other methods will be used, which will be described in section 2.2. First, some coefficients have to be defined that characterize the properties of a material regarding its interaction with light. Three main coefficients will be of importance for the simulations: The *absorption coefficient* μ_a , the *scattering coefficient* μ_s and the anisotropy factor g .

Attenuation coefficients

Any attenuation of a beam can be defined¹ as:

$$\mu = -\frac{1}{\Phi_e} \frac{d\Phi_e}{dz} \quad (2.2)$$

with Φ_e being the radiant flux and z being the length the beam has traveled.

The dependence of the radiant flux on the length traveled through a medium can be derived by solving this differential equation. Using an integrating factor of the form (μ is z dependent):

$$e^{\int_0^z \mu(z') dz'}. \quad (2.3)$$

One arrives at:

$$\frac{d\Phi_e(z)}{dz} e^{\int_0^z \mu(z') dz'} + \mu(z) \Phi_e(z) e^{\int_0^z \mu(z') dz'} = 0. \quad (2.4)$$

¹ISO 9288:1989

Making use of the product rule this will condense to:

$$\frac{d}{dz} \left(\Phi_e(z) e^{\int_0^z \mu(z') dz'} \right) = 0, \quad (2.5)$$

which finally can be integrated, yielding the well known Lambert-Beer-law:

$$\Phi_e^t = \Phi_e^i e^{-\int_0^l \mu(z) dz}, \quad (2.6)$$

where Φ_e^t is the transmitted radiation flux and Φ_e^i is the incident radiation flux.

For our case μ splits into two parts, according to: $\mu = \mu_a + \mu_s$. Where μ_a , as mentioned before, stems from losses due to absorption inside of the material, while μ_s stems from losses due to scattering into different directions. Both have units of inverse length ($\frac{1}{\text{m}}$) [9]. Sometimes μ is also denoted as μ_t , indicating that the total attenuation coefficient is used.

Anisotropy factor

The third parameter, the anisotropy factor, is tightly related to the scattering coefficient. It describes the mean change of direction after a scattering event took place. If an axis is defined on which an incoming photon travels, it gets deflected by an angle θ . The projected length of this new direction onto the original axis is given by $\cos(\theta)$. The unitless anisotropy factor is then defined as $g = \langle \cos(\theta) \rangle$ [9].

The parameter is in a range from -1 to 1, where 1 would be forward and -1 would be backward scattering. All values in-between show some preference for one, the other or non at all. The geometrical dependence of the deflection angle and thereby the anisotropy factor is depicted in figure 2.4.

2.2. Numerical treatment of light propagation

In the last section it has been shown that photon transport can be described by radiative transfer, since equation 2.1 can also be written in terms of μ_a , μ_s and g (see [10]).

Nevertheless, a more statistical approach has been chosen to be used for this works calculations. It mainly revolves around Monte-Carlo methods and is closely build on the work of L. Wang, S. L. Jacques and L. Zheng (see [11]).

Since this method strongly relies on the generation of random numbers, it should be at least noted that there are many ways in which uniform random numbers can be generated. These numbers will in the following be denoted as ξ . They were then used in various ways to sample from non-uniform random number distributions (e.g. the exponential distribution used in section 2.2.1). A detailed description of such methods and some examples for pseudo random number generators can be found in [12].

There are two interacting parts which are important for these simulations. The medium in which the light propagates on the one hand and the photon packets, on the other hand. The medium can be divided into several regions, each with individual values for

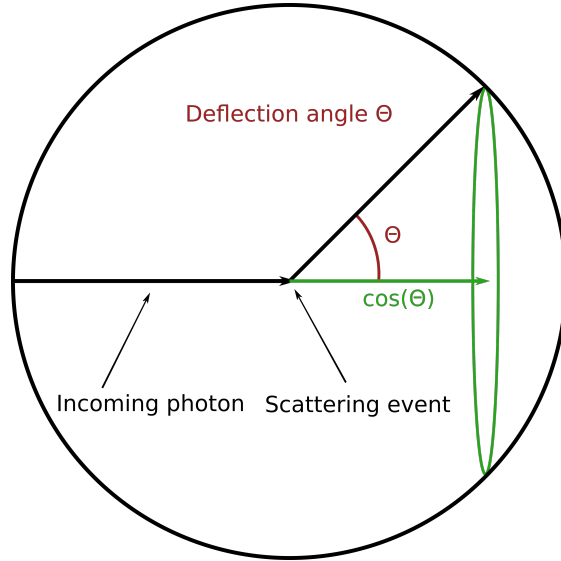


Figure 2.4.: *Schematic of the geometrical dependence of the deflection angle θ on the scattering event.*

the optical coefficients. Each photon packet is described by several parameters of its own: Position (x, y, z) , flight direction (u_x, u_y, u_z) and a weight W , which describes the relative amount of energy still left ($W \in [0, 1]$). It was assumed that both position and momentum of the photon packets were exactly known at any time. This can be seen as an approximation, neglecting any uncertainty.

Since each photon packet can be considered individually, one photon packet will be used in the following for an exemplary description. For ease of reading the term „packet“ will be omitted, which should be mentioned as to not cause any confusion.

2.2.1. Initialization and step size

First, the photon has to be initialized, assigning it an initial position and direction to travel in. For numerous photons these parameters will vary, depending on the beam geometry, which will be discussed in the next chapter.

Secondly, a dimensionless step size s has to be defined. This step size is dependent on a random number ξ and is connected to the path length the photon will travel as follows [11]:

$$P \{s \geq s_{sum}\} = e^{-\sum_i \mu_{ti} s_i}, \quad (2.7)$$

where P denotes the probability for the term inside of $\{\}$ to hold, $s_{sum} = \sum_i s_i$, μ_{ti} are the absorption coefficients for the region i and s_i are the distances traveled in the according regions.

Using the inversion method [12] and some rearranging one ends up with:

$$\sum_i \mu_{ti} s_i = -\ln(\xi). \quad (2.8)$$

The step size s is then initialized by $s = -\ln(\xi)$ and only after traveling this dimensionless „distance“ the photon will interact with the surrounding material. Why this step size was chosen to have no dimension will become apparent in the next section.

2.2.2. Photon movement, absorption and scattering

After the initialization, the distance to the nearest boundary of the current region d_b is calculated, with respect to the direction the photon is traveling in. Whether the photon hits this boundary and will therefore change its position into a new region, with differing optical properties, can be determined by the following equation [11]:

$$d_b \mu_t \leq s. \quad (2.9)$$

Here it becomes clear, why s was chosen to be dimensionless, since it can now be used to evaluate the inequation above, in any region of the computational domain.

Should the condition be true, the photon will be moved by the amount d_b and the remaining path length will be shortened according to $s \leftarrow s - d_b \mu_t$, no absorption or scattering will take place in this case. There is, in theory, a probability for a reflection of the photon from the boundary between regions. Simulating this was omitted, since it proves to be difficult for arbitrary three dimensional structures inside of the material. Should the condition not hold, interaction takes place after moving the photon by the amount $\frac{s}{\mu_t}$.

Absorption

First the relative amount of energy, which is lost at the interaction site has to be determined [11]:

$$\Delta W = \left(\frac{\mu_a}{\mu_t} \right) W. \quad (2.10)$$

This value, with its corresponding coordinates, is saved additively into an array. Further, the photon weight has to be reduced by this amount $W \leftarrow W - \Delta W$.

Scattering

After the absorption has been dealt with, the photon will be scattered. This scattering is described by two angles. The deflection angle $\theta \in [0, \pi)$ and the azimuthal angle

$\psi \in (0, 2\pi)$. Relying on a work by Henyey [13], Wang et al. expressed the deflection angle, dependent on a random variable ξ , as [11]:

$$\cos \theta = \begin{cases} \frac{1}{2g} \left\{ 1 + g^2 - \left[\frac{1-g^2}{1-g+2g\xi} \right]^2 \right\} & \text{if } g \neq 0 \\ 2\xi - 1 & \text{if } g = 0, \end{cases} \quad (2.11)$$

while the azimuthal angle is uniformly distributed: $\psi = 2\pi\xi$. Using these results the new direction of the photon can be calculated [11]:

$$\mu'_x = \frac{\sin \theta (\mu_x \mu_z \cos \psi - \mu_y \sin \psi)}{\sqrt{1 - \mu_z^2}} + \mu_x \cos \theta, \quad (2.12)$$

$$\mu'_y = \frac{\sin \theta (\mu_y \mu_z \cos \psi + \mu_x \sin \psi)}{\sqrt{1 - \mu_z^2}} + \mu_y \cos \theta, \quad (2.13)$$

$$\mu'_z = -\sin \theta \cos \psi \sqrt{1 - \mu_z^2} + \mu_z \cos \theta. \quad (2.14)$$

If the photon is traveling mainly in the z-direction (e.g. $|\mu_z| > 0.9999$), then the following equations should be used [11]:

$$\mu'_x = \sin \theta \cos \psi, \quad (2.15)$$

$$\mu'_y = \sin \theta \sin \psi, \quad (2.16)$$

$$\mu'_z = \text{SIGN}(\mu_z) \cos \theta. \quad (2.17)$$

2.2.3. Photon termination

After the photon has traveled some distance and has either interacted with the medium or not, a check is performed, which determines if the photon will travel further or if it will be terminated. The main parameter this depends on is the photons weight W . If it is zero, the photon can be seen as dead and will therefore travel no further. If, on the other hand, the photons weight is large $W \gg 0$, it will travel further to interact with the medium again. After each interaction the step size is set to zero and for surviving photons a new step size is generated, as was described for the initialization. A photon with a weight falling under a certain threshold, which can be defined, will undergo a so-called roulette. This has to be done in order to ensure conservation of energy.

Defining some chance $(\frac{1}{m})$ (e.g. $m = 10$), photons have some probability to survive as [11]:

$$W \leftarrow \begin{cases} mW & \text{if } \xi \leq 1/m \\ 0 & \text{if } \xi > 1/m. \end{cases} \quad (2.18)$$

All the above is performed for a large amount of photons (e.g. 10^5), which in turn yields an array filled with the relative weights of the absorbed energy Q . Normalizing this array with respect to volume and the number of photons and multiplying it by the incident

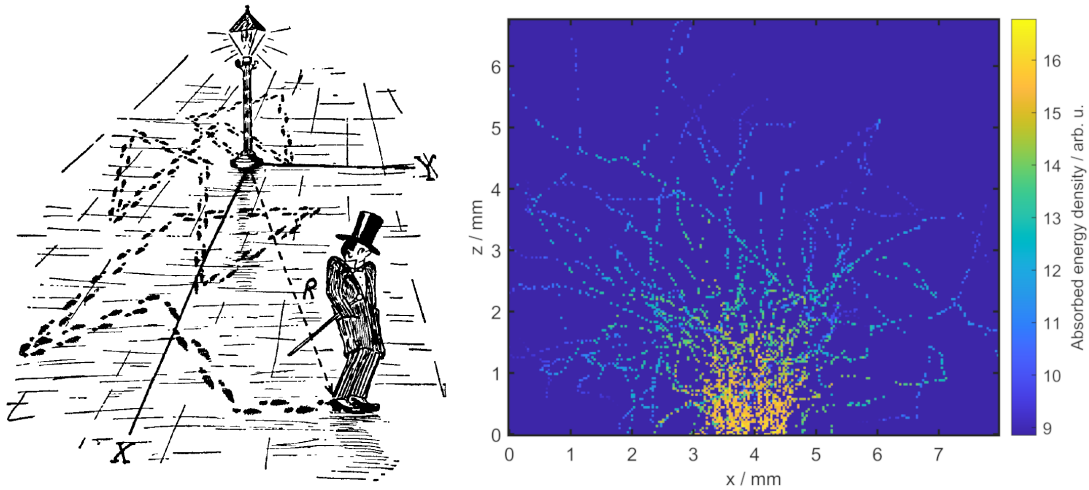


Figure 2.5.: *Drunkard problem compared to a simple Monte-Carlo simulation. Artistic depiction of the drunkard problem (left) [14] and MAP of a Monte-Carlo simulation of photon packets propagating through a homogeneous medium (right).*

beam energy, yields an energy distribution throughout the sample in $\frac{J}{m^3}$, which can be used in further steps. A schematic of the whole Monte-Carlo algorithm can be found in figure 2.6.

This algorithm resembles a popular problem from probability theory known as random walk. It is also often introduced as the drunkards problem, which stems from a nice analogy to a drunken sailor walking around in a random fashion. This problem often is concerned with the distance this drunkard travels from the tavern he was drinking at, considering that the direction he travels in changes randomly after every step he took. Although the distance the photons travel during the simulations is not the main concern, they behave in a matter similar to the drunken sailor, changing their direction of travel in a probabilistic fashion. The effect of this can easily be seen when performing such simulations with few photon packets, making it possible to identify some of their individual paths. The result of such a simulation, performed with 60 photon packets in a homogeneous medium, can be seen in figure 2.5. Next to it is an artistic depiction of the drunkard problem.

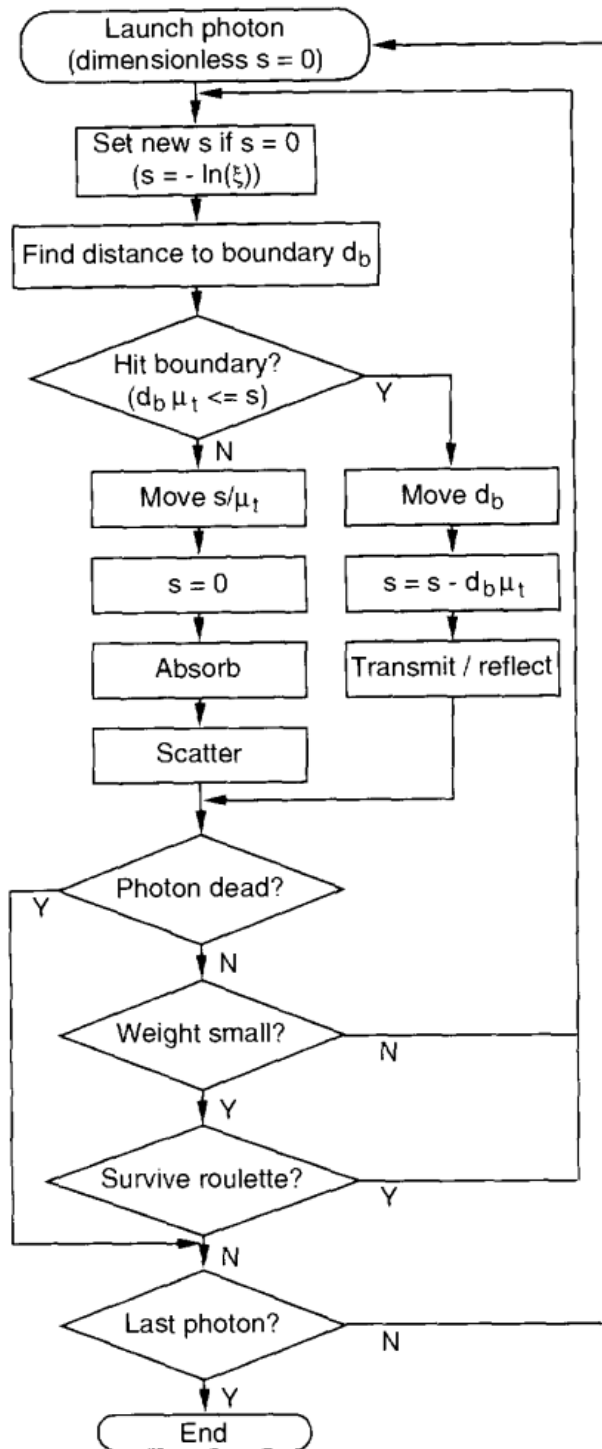


Figure 2.6.: Schematic of the photon propagation Monte-Carlo algorithm [11].

2.3. The wave equation

After having spent some time with the description of how light interacts with matter and having gained a detailed understanding of how to calculate an energy distribution caused by this interactions, utilizing a Monte-Carlo algorithm, the next step involves the reaction of the medium to the disturbance caused by this. It is therefore necessary to take a look at the fluid dynamics of the system at hand.

The simulations, which build upon the theory discussed in this section, will include many effects, such as frequency dependent damping and heterogeneities in the material, which are cumbersome in notation and of no real benefit for the understanding of the underlying principle. Therefore, these effects will be left out in this short discussion of the theory behind the propagation of acoustic waves. Nevertheless, one equation should be mentioned, as it describes said absorption [15]:

$$\alpha = \alpha_0 \omega^y, \quad (2.19)$$

where α is the absorption coefficient, α_0 a constant prefactor, ω the frequency and y the power law exponent. This equation is generally referred to as the frequency power law of acoustic attenuation.

Considering a lossless homogeneous fluid medium, three first-order differential equations can be found, which describe small alterations in the materials properties, dependent on time and space. These equations are given by [16, 17]:

$$\frac{\partial \mathbf{u}}{\partial t} = - \frac{1}{\rho_0} \nabla p, \quad (2.20)$$

$$\frac{\partial \rho}{\partial t} = - \rho_0 \nabla \mathbf{u}, \quad (2.21)$$

$$p = c_0^2 \rho. \quad (2.22)$$

The first one being the equation for *momentum conservation*, connecting the time derivative of the particle velocity \mathbf{u} with the gradient of the acoustic pressure p , considering the equilibrium density ρ_0 . The second one describing *mass conservation* and the third being the *pressure-density relation*, connecting the pressure to the density ρ and the speed of sound c_0 .

Although these equations can be solved and characterize the propagation of a wave through a medium, they do not include terms which describe the origin of this wave. These source-terms can be added, yielding slightly differing differential equations [17]:

$$\frac{\partial \mathbf{u}}{\partial t} = - \frac{1}{\rho_0} \nabla p + \mathbf{S}_F, \quad (2.23)$$

$$\frac{\partial \rho}{\partial t} = - \rho_0 \nabla \mathbf{u} + S_M, \quad (2.24)$$

$$p = c_0^2 \rho, \quad (2.25)$$

where \mathbf{S}_F is a force source-term and S_M is a mass source-term. These three equations can be combined to form a second-order differential equation, generally known as the wave equation. To arrive at the wave equation with regards to pressure, one uses the third equation from above to substitute for ρ in the second equation. Taking the derivative with respect to time of this second equation and swapping $\frac{\partial}{\partial t}$ and ∇ in front of \mathbf{u} , one gains the opportunity to set the momentum conservation (first equation) equal to the mass conservation (second equation), after taking the divergence of the first equation (multiplying by ∇). One ends up with:

$$\nabla^2 p - \frac{1}{c_0^2} \frac{\partial^2 p}{\partial t^2} = \rho_0 \nabla \mathbf{S}_F - \frac{\partial}{\partial t} S_M. \quad (2.26)$$

This equation can be transformed further, aiding a description of thermoacoustic effects. The assumptions necessary for this are the following: At the time of excitation the fluid is stationary and the generation of heat is only owed to the photoacoustic effect. Further, heat conduction is negligible, the same is true for the materials viscosity. Heat conduction can of course only be neglected, if the heating occurs on a time scale which is generally much shorter than the acoustic travel time (stress confinement is fulfilled). It is then possible to neglect \mathbf{S}_F and write $S_M(\mathbf{x}, t) = \mathbf{Q}(\mathbf{x}, t) \frac{\beta}{C_p}$, where β is the volume thermal expansivity, C_p is the specific heat capacity for constant pressure and \mathbf{Q} is given by $\mathbf{Q}(\mathbf{x}, \mathbf{t}) = Q(\mathbf{x})\delta(t)$ (Q is the heat energy absorbed per volume, as defined in section 2.2). This results in a more well known wave equation for photoacoustic excitation [18]:

$$\nabla^2 p - \frac{1}{c_0^2} \frac{\partial^2 p}{\partial t^2} = -\frac{\beta}{C_p} \frac{\partial Q}{\partial t}. \quad (2.27)$$

It is further possible to define an initial pressure distribution $p_0(\mathbf{x}) = p(\mathbf{x}, t = 0)$, making use of the Grüneisen parameter Γ , which is a dimensionless quantity describing the efficiency of the conversion from heat to pressure [18]:

$$p_0(\mathbf{x}) = \left(\frac{\beta c_0^2}{C_p} \right) Q(\mathbf{x}) = \Gamma Q(\mathbf{x}). \quad (2.28)$$

It has been shown that equation (2.27) is solvable on the basis of Green's functions. The fundamental solution regarding the wave function reads as follows [18]:

$$\nabla^2 G - \frac{1}{c_0^2} \frac{\partial^2 G}{\partial t^2} = \delta(\mathbf{x} - \mathbf{x}')\delta(t - t'), \quad (2.29)$$

where the solution G can be written as:

$$G(\mathbf{x}, t; \mathbf{x}', t') = \frac{\delta[|\mathbf{x} - \mathbf{x}'| - c_0(t - t')]}{4\pi|\mathbf{x} - \mathbf{x}'|}. \quad (2.30)$$

After some calculations, which can be found in reference [18], the solution, regarding the initial value problem presented in equation (2.27), turns out to be:

$$p(\mathbf{x}, t) = \frac{1}{(2\pi)^3} \int p_0(\mathbf{k}) \cos(ckt) e^{i\mathbf{k}\mathbf{x}} d\mathbf{k}, \quad (2.31)$$

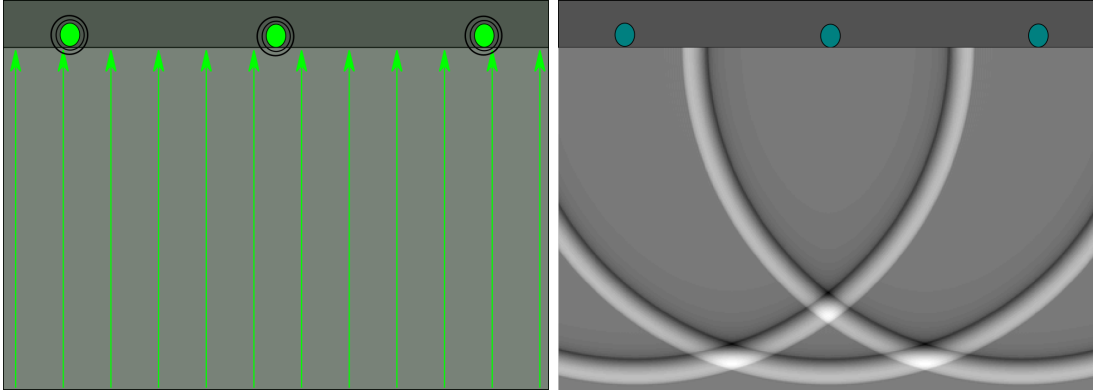


Figure 2.7.: *Snapshot of a calculated wave propagation. The absorption of a laser beam (indicated in green), by spherical absorbers at $t = 0$ (left), consequential wave propagation at a point in time $t > 0$ (right).*

where \mathbf{k} stems from a Fourier transformation and therefore denotes spatial frequencies. By utilizing this formula, it is possible to calculate the pressure distribution anywhere in space and at any time, given an initial pressure distribution p_0 . The result of a calculation for such a wave propagation is shown in figure 2.7.

2.4. Numerical treatment of the wave propagation using the k-space pseudospectral method

The analytical solution discussed in section 2.3 can be used in some cases (e.g. for the reconstruction of full field signals in PAT [5]), relying on it for inhomogeneous media on the other hand is not feasible. It is therefore indicated to resort to numerical methods for solving the differential equations at hand, when dealing with complex problems. There are numerous ways in which such equations can be solved numerically, the idea discussed in this section was chosen with regard to the work of Treeby et al. [19]. Since the simulations of wave propagation performed for this thesis highly depend on the free-to-use k-wave toolbox², its inner workings shall be discussed briefly. For a more in depth discussion the reader is referred to [19, 20, 21, 22].

2.4.1. k-space pseudospectral method

The algorithms implemented by Treeby et al. rely on the pseudospectral k-space method. This method was chosen because general finite difference (FD) methods usually require a large amount of grid points in order to achieve acceptable accuracy [12]. Using approximately 10 points per wave length would cause huge arrays, which cannot be handled

²<http://www.k-wave.org/>

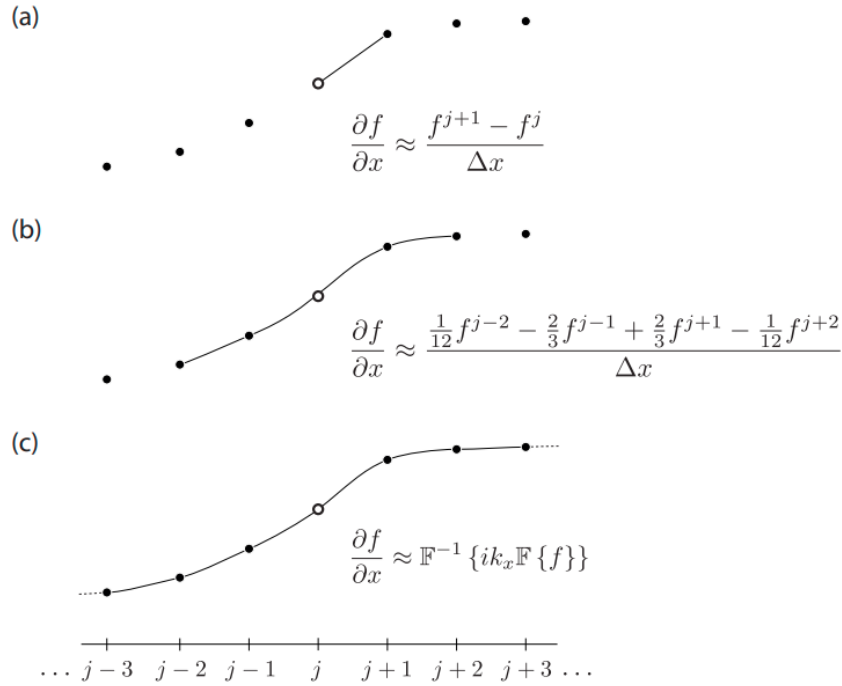


Figure 2.8.: *Schematic of the calculation of spatial gradients in one dimension. First-order forward difference method (a). Fourth-order central difference method (b). Fourier collocation spectral method (c) [22].*

when simulating broadband acoustic waves in heterogeneous media in three-dimensional space. This problem can be overcome by said method, since it is a combination of spatial derivatives performed using the Fourier collocation method and expressing the time propagation in the frequency domain [19]. With this method one is able to fit a Fourier series to all of the data points, which makes it a more global method than conventional FD methods [20]. Using sinusoidal functions, this only requires two grid points per wavelength, drastically minimizing the needed amount of memory. The method further relies on the fact that derivatives of bounded functions can be expressed in Fourier space:

$$\mathcal{F} \left\{ \frac{\partial}{\partial x} f(x) \right\} = -\frac{1}{2\pi} \int f(x) (-ik_x) e^{-ik_x x} dx = ik_x \mathcal{F} \{f(x)\}, \quad (2.32)$$

where \mathcal{F} denotes the Fourier transform. A schematic of this relation is depicted in figure 2.8.

2.4.2. Solving first order equations on a staggered grid

The method discussed in section 2.4.1 can be used to solve second-order differential equations such as equation (2.26). Nevertheless, the Matlab k-wave toolbox instead

solves the coupled first order equations, using a staggered grid scheme, in order to achieve higher accuracies and to stabilize the algorithm [23, 19].

A more detailed description of the procedure can be found in the k-space manual (see [22]), a rough understanding of the necessary steps can be gained from figure 2.9. From this schematic it becomes apparent that besides space being staggered, also the time domain gets discretized in finer steps than usual.

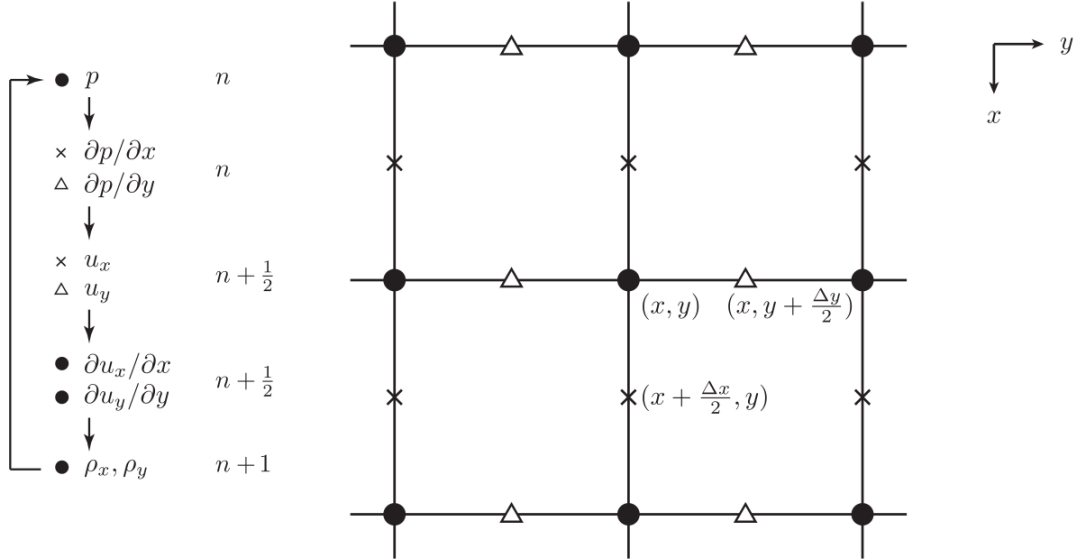


Figure 2.9.: Schematic showing the steps necessary in the computation of solutions to coupled first order differential equations on a staggered grid in two dimensions. The staggered grid points are represented by crosses in the x -direction and triangles in the y direction. The corresponding quantities calculated there can be seen on the left hand side. The staggering in time is represented by $n, n + \frac{1}{2}$ and $n + 1$ [22].

2.4.3. Perfectly matched layer

One thing, which particular care has to be taken about when performing numerical calculations on wave-equations, are boundary conditions. In most cases open boundary conditions are strived for, which poses a problem to the inherently periodic k-space models. Calculations performed by these methods result in waves propagating from one end of the region of interest (ROI) to the other end, as if the two were connected (think about a string for a one-dimensional problem, or a torus for a two-dimensional one). Expanding the grid size, to a point where this effect poses no problem to a simulation, is highly ineffective. Therefore, the proposition of a perfectly matched layer (PML) surrounding the ROI has been made [24].

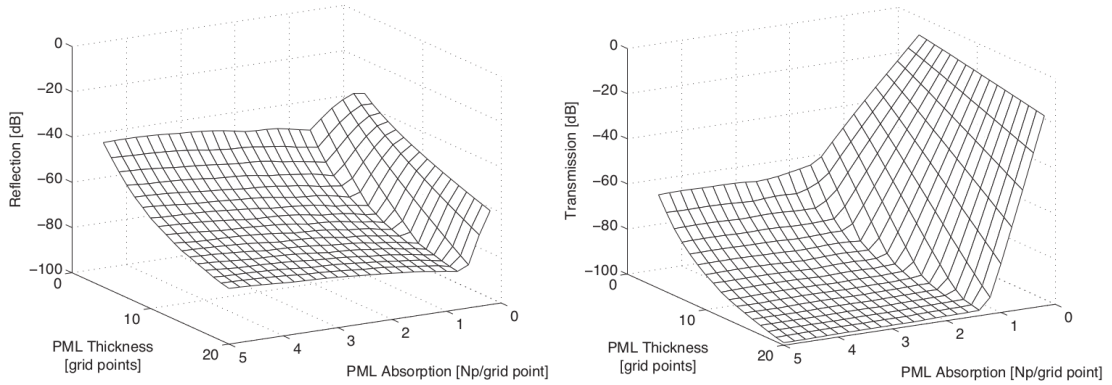


Figure 2.10.: *Graphs showing the behavior of the PML for different thicknesses and absorption coefficients. Reflection (left) and transmission (right) [22].*

This PML is thin compared to the rest of the ROI but highly absorbing. This causes the incoming waves to decay quickly, which hinders them from reaching the other side of the grid. Although other versions of PMLs exist, the k-wave toolbox uses the split-field PML proposed by Berenger in 1994, getting its name from the splitting of the incoming waves components into parallel and perpendicular to the PML [19, 24].

The main idea behind this layer is that it absorbs outgoing waves well enough to keep them from wrapping around the computational domain and additionally it must not reflect any part of the waves back into the ROI. This calls for nonphysical equations, which split the density (or pressure) into Cartesian coordinates ($\rho = \rho_x + \rho_y + \rho_z$). At a boundary to the PML, only the component perpendicular to the boundary is absorbed. These equations were implemented into the linear differential equations solved by the k-wave toolbox [19]. The right value for the absorption of the PML has to be chosen carefully, as to absorb waves well enough, in order to keep them from reaching the end of the PML. On the other side, choosing an absorption which is too strong, yields reflections back into the computational domain. The main reason for these reflections are numerical problems, which arise when the gradient across the PML boundary is too large. This subtle interplay can be seen in figure 2.10.

2.5. Photoacoustic microscopy

The physical effects described in the sections preceding this one are universal for all photoacoustic methods. The method which is the main topic of this thesis is photoacoustic microscopy (PAM), which makes use of these phenomena to gain high resolution images from a sample. In detail this can be achieved in many ways but the main idea is to excite a defined region of a sample, respectively, focus a beam of light tightly onto the sample and measure acoustic signals from that same region. This of course results in an interplay between two kinds of foci. On the one hand, there is the optical focus arising

from focusing the light (mainly laser beams are used for PAM [25, 26]) onto the sample. On the other hand, one can gain an additional region of focus by using acoustic lenses, which focus the acoustic waves emitted from the sample onto the detector. Depending on which focus is mainly responsible for the resolution achievable with the microscope, it is either classified as an acoustic resolution (AR-PAM) or optical resolution (OR-PAM) photoacoustic microscope. Generally it is tried to align both of these foci axially, as this yields the highest sensitivity [25]. There are different ways in which one can exploit both of this foci, according to the field of application, some of which will be discussed during the course of this section.

Using conventional optical microscopy poses one crucial problem when dealing with turbid media, from which depth information is of interest: Its performance mainly relies on the ability to focus sharply onto the object of interest. Considering samples with high scattering coefficients, this is only possible in a very shallow region at the surface of the sample and when reaching larger depths (~ 1 mm) the incoming photons have undergone several scattering events, which leads to a significant broadening of the incoming beam as a whole [26]. Overcoming this restriction separates PAM from purely optical-microscopy, which still is the most widely used imaging technique for biomedical investigations [27]. The reason for this advantage regarding PAM is that scattering is about three orders of magnitude weaker (considering human tissue) for ultrasonic waves than for photons [10]. This means PAM combines the good contrast gained by the difference in optical properties of materials, differing even with respect to the used excitation wavelength, and the resolution of ultrasound detection in deep layers of turbid media. As an example the absorption of oxygenated (HbO_2) and not oxygenated Hemoglobin (Hb), dependent on the wavelength of light, can be seen in figure 2.11.

Achieving a coaxial setup for the two foci is no simple task and many systems have been designed in order to approach this problem. Some of these experimental configurations are depicted in figure 2.12, combined with notes on their advantages and disadvantages. It can be seen that one of the easiest methods to implement overlapping foci is to place the ultrasound detector and the incoming laser beam off-axis. Although easy to implement, this setup limits the field of view and also axial resolution is limited [29].

Another system which shall be briefly mentioned, since it was used to gather some experimental data for this thesis, is the coaxial configuration based on an opto-ultrasound beam-combiner. This beam-combiner enables the spatial separation of the ultrasound transducer from the laser beam. While the laser beam travels straight through this glass element, sound waves get reflected twice at boundaries, before reaching the detector. This double reflection should in theory not cause any large distortion to the signal, although there is a loss in energy caused by the acoustic impedance mismatch [25]. One main advantage of such a setup is its versatility, as it is even possible to build systems which can easily switch between OR-PAM and AR-PAM [30].

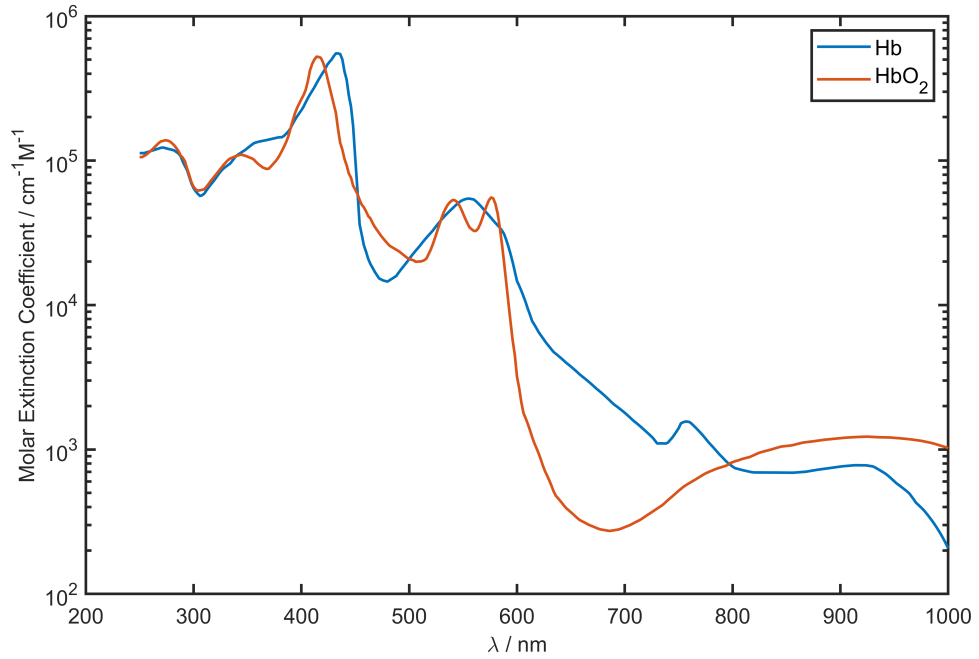


Figure 2.11.: *Molar extinction coefficient for Hemoglobin dependent on the wavelength of light [28].*

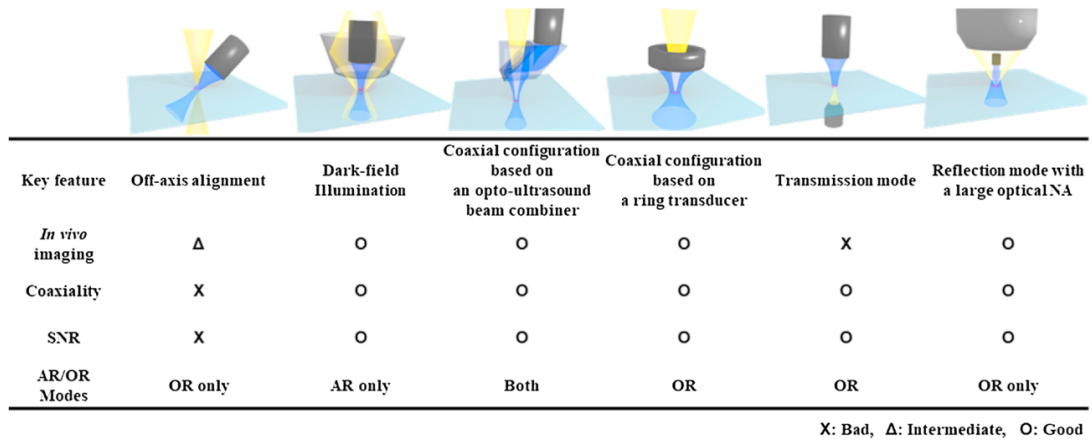


Figure 2.12.: *Schematic depictions of different PAM setups including some of their advantages and disadvantages [25].*

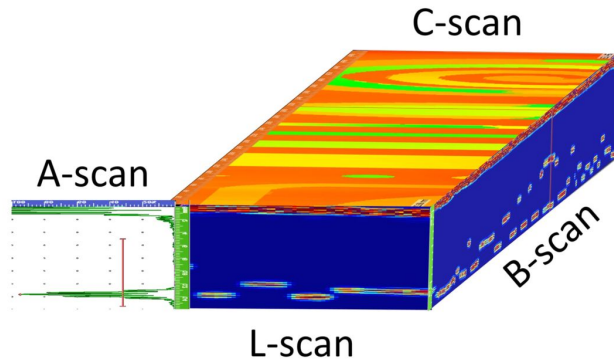


Figure 2.13.: *Schematic depiction of a sample indicating the definitions of A-scan, B-scan, C-scan and L-scan [33].*

Having chosen a setup for the detection of ultrasound signals one usually is confronted with another problem. A non-moving PAM-setup is only capable of gathering a single time signal from one point in space. This is called an A-line, from which technically speaking no image can be formed. Although this can in some rare cases be sufficient, for example if the sample under investigation is changing its characteristics over time and therefore a measurement series at one spatial position over a certain time-frame yields expressive results, it is more common to gather signals from different locations. This can be achieved in different ways. A simple way is to mount the scan-head or the sample onto movable stages, which allow signals to be recorded on a line or a grid. Signals recorded on a line are commonly referred to as a B-scan image, combining several of those images yields a three dimensional dataset, where two dimensions are given by the spatial separation between individual measurement points and the third dimension is given by the time domain gained from the ultrasound sensor. A depiction of these different ways to display the measured data is given in figure 2.13. In addition to the A-scans and B-scans, C-scans and L-scans are defined. While a C-scan can be seen as a slice in the time domain, a L-scan is very similar to a B-scan except for it not being acquired in the scanning direction. Such scanning techniques are easy to implement and therefore widely used, especially in areas where speed and size are no major concern [31].

Faster scanning approaches have been implemented for specific tasks which require high data throughput. An example for this would be micro-electro-mechanical systems (MEMS), which allow for much faster scanning [32].

It should be noted that talking about ultrasound sensors generally refers to many types of sensors, which can use different physical principles for pressure detection. Since the measurement of rapidly changing pressure fields is a huge topic of its own, the details will not be discussed here. Nevertheless, it shall be mentioned that one of the most commonly used ultrasound detector types is one relying on piezoelectric materials, where a deformation of the sensing crystal structure results in a measurable voltage.

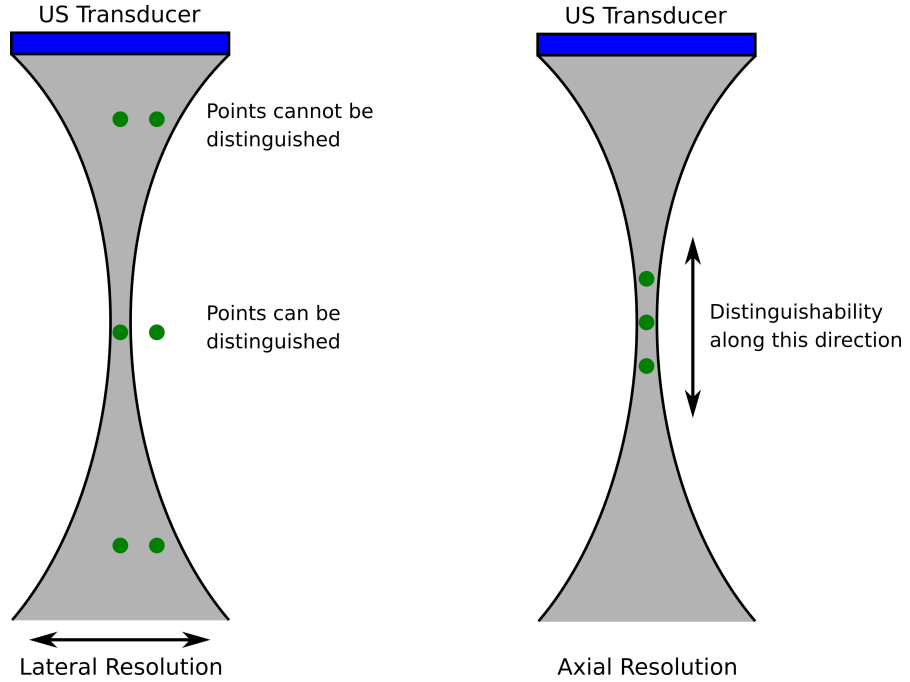


Figure 2.14.: Schematic showing the definitions of lateral and axial resolution.

2.5.1. Spatial resolution of PAM-systems

One of the most important parameters regarding any optical system intended for microscopy is the possible resolution which can be achieved. Since the PAM-systems described above are in general capable of capturing three-dimensional datasets, it is important to distinguish between two directions of resolution. One direction, which will be referred to as axial, is the direction parallel to the excitation beam, respectively, the direction of detection. The other one is perpendicular to the first one and is commonly called lateral. A schematic depiction of these geometrical dependencies can be seen in figure 2.14.

Since the axial resolution (AR) is mainly determined by the acoustic bandwidth of the ultrasound detector, it can be seen as equal for both OR-PAM and AR-PAM and is given by the following relation [25]:

$$AR_{OR-AR-PAM} = 0.88 \frac{c_0}{\Delta f_c}, \quad (2.33)$$

where c_0 is the speed of sound (roughly $1540 \frac{\text{m}}{\text{s}}$ for biological tissue) and Δf_c is the bandwidth of the PA signal that lies in a range of 1 MHz to 100 MHz, which is much wider than the bandwidth of conventional piezoelectric transducers [34]. This allows for the substitution $\Delta f_c \approx f_0$, where f_0 is the transducers central frequency.

Acoustic resolution photoacoustic microscopy

For AR-PAM the acoustic focus spot is smaller than the optical one. This means that for the best possible lateral resolution (LR) the center frequency f_c of the PA signal plays an important role, as well as the acoustic numerical aperture NA_a . The equation describing the dependence on the above parameters reads as follows [25]:

$$LR_{AR-PAM} = 0.71 \frac{c_0}{NA_a \cdot f_c} \quad (2.34)$$

From this it becomes clear which parameters of the system have to be altered in order to gain a better resolution. On the one hand, it would be possible to increase the center frequency of the ultrasound detector. The advantage of a higher resolution would be coupled to the disadvantage of higher acoustic attenuation for higher frequencies, which can be argued from equation (2.19). On the other hand, one could increase the acoustic numerical aperture, which would come with the disadvantage of reducing the resolution in out of focus areas.

Optical resolution photoacoustic microscopy

Contrary to AR-PAM, OR-PAM relies on the focusing of the excitation beam, which means that only a very small region of the sample gets illuminated. This changes the characteristics of the lateral resolution, since the optical parameters are now of a higher importance. This resolution can be defined in different ways, one of them that can easily be used for an experimental evaluation is the full width half maximum of the point spread function. The equation describing this relationship is the following [25]:

$$LR_{OR-PAM} = 0.51 \frac{\lambda_O}{NA_O}, \quad (2.35)$$

where λ_O is the optical wavelength and NA_O is the optical numerical aperture. Using this principle it is possible to reach high lateral resolutions by focusing the excitation beam tightly. However, as mentioned before, one is confined by scattering effects, which limit the penetration depth.

2.6. Resolution limitation caused by focusing

The theory discussed in the last section gave the framework for performing PAM measurements in one, two or three dimensions. While the one dimensional data is gained from the time of flight of ultrasound signals, the second and third dimensions are gained from some sort of spatial deviation. For simplicity it will be assumed that the transducer together with the excitation beam are being scanned over the sample in question to gain this space dependent information.

Taking a look at figure 2.14, one can see that the final resolution is highly dependent on the focusing of the excitation beam (OR-PAM), ultrasound detector (AR-PAM) or a combination of both. Features of the sample lying directly in the depth-plane of the focus can be resolved much better than ones lying above or below this focus-plane. Most samples that will be analyzed using PA techniques will have a distribution of features in three-dimensional space, which in turn means that the position of the focus-plane has a large impact on the final data.

It would theoretically be possible to scan a sample multiple times with varying positions of the focus-plane. For obvious reasons this would counteract some of the most important benefits of photoacoustic microscopy and is therefore not a favorable approach. Hence, this section will be used to discuss the resolution limiting effects further and to review some of the methods to counteract them.

2.6.1. Origin of artifacts

First, it is instructive to discuss the origin of artifacts which will be seen, when recording data with a PAM setup. Although these effects are generally three-dimensional, it is easier to discuss them in two dimensions, which can be expanded to a third one effortlessly. Further, for the first part of the discussion, it is assumed that the focus plane lies at the top of the sample ($z = 0$).

Directly at the focus plane, any feature in the sample would only produce a measurable signal, if the detector was directly above said detail. However, regarding points not in the focus plane (i.e. $z > 0$), the shape of the focus allows signals to be detected, which do not stem from the direct line of sight of the detector. These signals are then delayed in time by a certain amount [35]. If the detector is scanned in the x -direction, the detail lies at point $\mathbf{x}_p = (x_p, z_p)$ and the detection point resides at $\mathbf{x}_n = (x_n, 0)$, the time (t_p) the wavefront, generated by the feature, needs to reach the point of measurement is given by:

$$t_p(\mathbf{x}_n) = \frac{1}{c_0} |\mathbf{x}_p - \mathbf{x}_n| = \frac{1}{c_0} \sqrt{(x_n - x_p)^2 + z_p^2}. \quad (2.36)$$

This relation can be easily understood when looking at figure 2.15.

This is the well known formula for a hyperbola. In other words, if the sample only is comprised of one point-like feature, which lies below the focus plane, one would gain a B-scan image which would show a hyperbola, where the apex is indicative of the real position of the detail. The interpretation of such a dataset would be quite trivial. Real samples however are comprised of a large number of different geometrically complex structures, each of which can be thought of as a sum of point sources. This yields very complex datasets, which need well thought out algorithms for reconstruction. Two such techniques will be discussed in the next section.

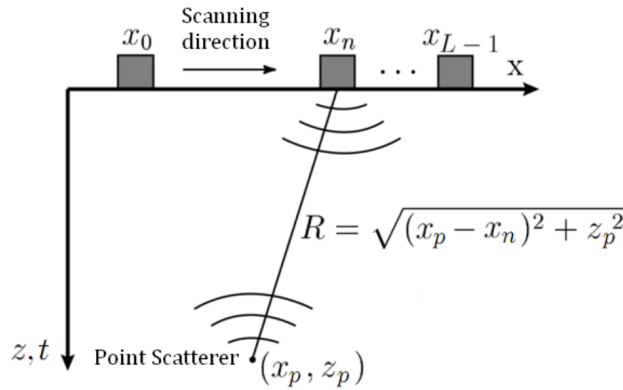


Figure 2.15.: *Graphical representation of sensor-feature distance relationship [35].*

2.6.2. Correction of the artifacts

Considering the relatively simple form of the mathematical description of the mentioned artifacts (see equation (2.36)), some sophisticated algorithms have been implemented to overcome the limitations caused by them. It is, however, useful to first take a look at simpler forms of correction, such as delay and sum (DAS) methods and then go on to more complex calculations such as Fourier domain algorithms.

Many of these schemes are connected to the term synthetic aperture focusing technique (SAFT) [36, 37]. This can be a little misleading, since the setups described in this thesis already are focusing the detection in one way or another. However, looking at the schematic in figure 2.16, it can be seen that this focusing results in a geometry, which can be interpreted by introducing the concept of a virtual detector. This virtual detector lies in the focus plane of our actual detector and has cone like detection volumes extruding downwards as well as upwards from it [36]. Both of these half spaces can be corrected as if the detector would really reside at the focus plane.

Delay and Sum

One of the most easily comprehensible ways to correct for the hyperbolic artifacts that were described in the last section, is the so-called delay and sum (DAS) method. It considers the virtual detector described above as the detector for PA signals, which come from a defined angular range [36]. At each scan position, i.e., for each acquired A-scan, the reconstruction is carried out by shifting the adjacent A-lines by the correct amount (according to equation (2.36)) and taking the sum over them as follows [36, 37]:

$$f_{DAS}(t) = \sum_{i=1}^N s_i(t - \Delta t_i), \quad (2.37)$$

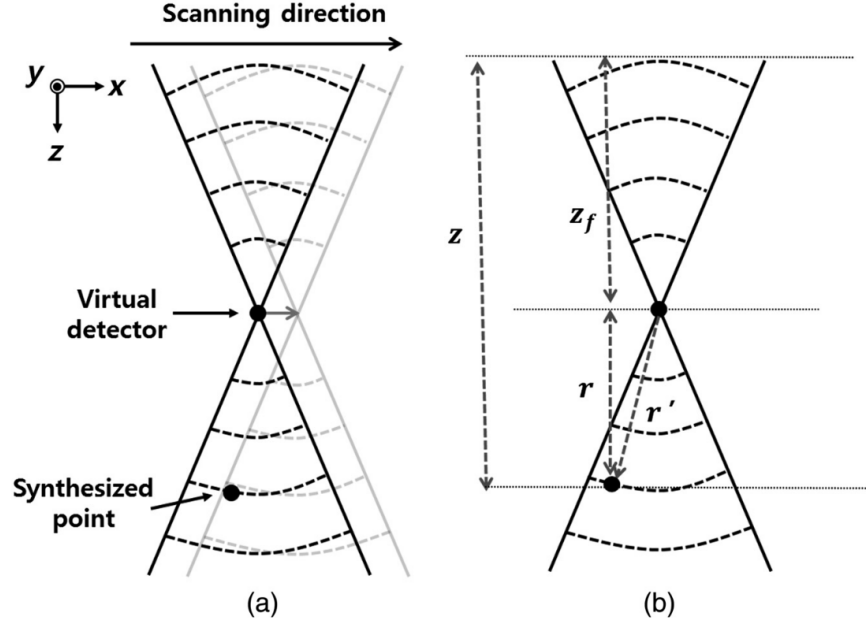


Figure 2.16.: Schematic showing the concept of the virtual detector [36]. z being the depth of the synthesized point, z_f the focal depth of the used detector and r and r' are the distance to the focal plane and the distance to the virtual detector, respectively.

where f_{DAS} is the new signal, s_i is the original signal of the i 'th scan and N is the number of scan lines to be used in the calculation. N depends on the angular range of the virtual detector. The wider this range is, the more lines should be considered for reconstruction [37].

According to the distances denoted in figure 2.16, Δt_i is calculated as follows:

$$\Delta t_i = \text{SGN}(z - z_f) \cdot \frac{(r - r')}{c_0}, \quad (2.38)$$

where z is the depth of the synthesized point, z_f is the focal depth and r and r' are the distance to the focus plane and the distance to the virtual detector, respectively. The focal depth can be attributed to the focusing characteristics of the actual detector. This of course translates to the description in section 2.6.1 quite easily.

Having delayed these signals (i.e., $s_i(t) \leftarrow s_i(t - \Delta t_i)$), one can further improve the quality of the reconstruction by introducing a coherence factor (CF) [36]. This factor reduces the influence of off-axis details, which cause the individual time-delayed signals to be out of phase. The factor can be defined as:

$$CF(t) = \frac{|\sum_{i=1}^N s_i(t)|^2}{N \sum_{i=1}^N |s_i(t)|^2}. \quad (2.39)$$

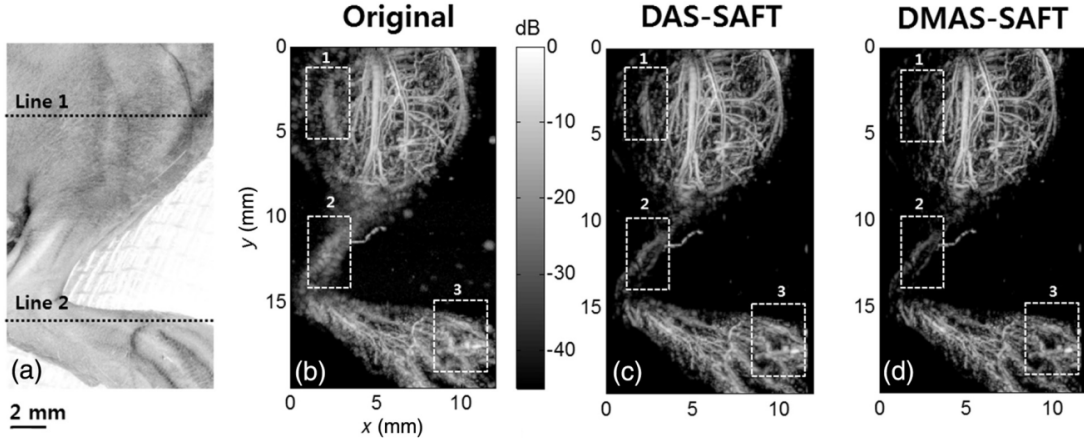


Figure 2.17.: AR-PAM images of a mouse leg. (a) Photo of the leg. (b), (c) and (d) maximum amplitude projections of the leg, processed with different methods [36].

CF can be seen as a multiplicative factor, since its value ranges from 0, for no coherence of the signals, to 1 for total coherence. This then yields the final reconstructions as:

$$f_{DAS-CF}(t) = CF(t) \cdot f_{DAS}(t). \quad (2.40)$$

Over the years this method has seen some improvements. More sophisticated algorithms have been implemented, such as delay multiply and sum algorithms (DMAS) [38] and further advances on that such as filtered-DMAS(F-DMAS) [39]. This filtering involves some further processing and thereby improves the lateral resolution, the signal to noise ratio by noise rejection and the contrast resolution. A study on the performance of DAS and DMAS, using an AR-PAM, was carried out by Park et al. [36]. Some of their results can be seen in figure 2.17.

When dealing with discrete signals, such as recorded in practice, all these operations have to be carried out on a pixelwise basis. This is computationally expensive, especially because it involves interpolations for calculating the time delay of the signals. A method which improves on the speed of the calculation is based on fast Fourier transformations and will be discussed next.

Frequency Domain Reconstruction

The method described in this section overcomes some of the downfalls of the DAS methods from above. The reconstruction of measured signals in the frequency domain (also referred to as Fourier space), can be seen as a global method, since it is able to alter the signals in one step and has no need for a pixelwise operation. It has been derived theoretically [40] and its effectiveness has also been proven in experiments [41].

Starting with the (acoustical) wave equation, which was discussed in section 2.3, a procedure for the reconstruction, relying on the use of the dispersion relation, was derived by Xu et al. [40]. The main idea behind the algorithm can be explained via a three-step process:

1. The measured signals $p_d(x, y, t)$ are Fourier transformed with respect to x, y and t , which yields $P_d(k_x, k_y, k_t)$.
2. Considering a constant speed of sound c_0 , a dispersion relation can be formulated,

$$k_z = \sqrt{\left(\frac{k_t}{c_0}\right)^2 - k_x^2 - k_y^2}, \quad (2.41)$$

which is used to map the signals in Fourier space according to the following relation [41]:

$$P_0(k_x, k_y, k_z) = \frac{2c_0 k_z}{\text{SGN}(k_z) \sqrt{k_x^2 + k_y^2 + k_z^2}} P_d\left(k_x, k_y, c_0 \cdot \text{SGN}(k_z) \sqrt{k_x^2 + k_y^2 + k_z^2}\right) \quad (2.42)$$

3. After this remapping in the frequency domain, the final reconstruction can be attained by performing the inverse Fourier transformation in all three dimensions.

A schematic of this approach for a two-dimensional problem can be seen in figure 2.18. This approach works well in theory but there are some difficulties attached to it. One of the main problems is the need to discretize the problem in some way, since the data is only given at certain points. This calls for some interpolation routines, which can cause artifacts, when being performed in the frequency domain. Some efforts have been made to overcome these issues (see for example [42]).

Comparison of the methods

In a work by Spadin et al. it has been shown that the frequency domain and delay and sum methods, for the reconstruction of photoacoustic images, yield practically the same results. The artifacts usually attributed to performing interpolations in the Fourier space have been successfully mitigated by using zero padding and truncated regularized inverse k-space interpolation. This means that the frequency domain algorithm is especially suited for large datasets, mainly caused by it being the faster method. This speed enhancement mainly stems from it being a global method, where calculations are carried out on the whole dataset at once, not pixelwise as is the case for DAS algorithms. Further, said calculations involve a Fourier transformation, which can be computed comparatively fast utilizing fast Fourier transformation algorithms (FFT). These can even be run on GPUs, improving the calculation times further. Spadin et al. have shown, that this can almost yield a factor five speedup (DAS→0.23 s/B-scan, FD→0.05 s/B-scan) [43].

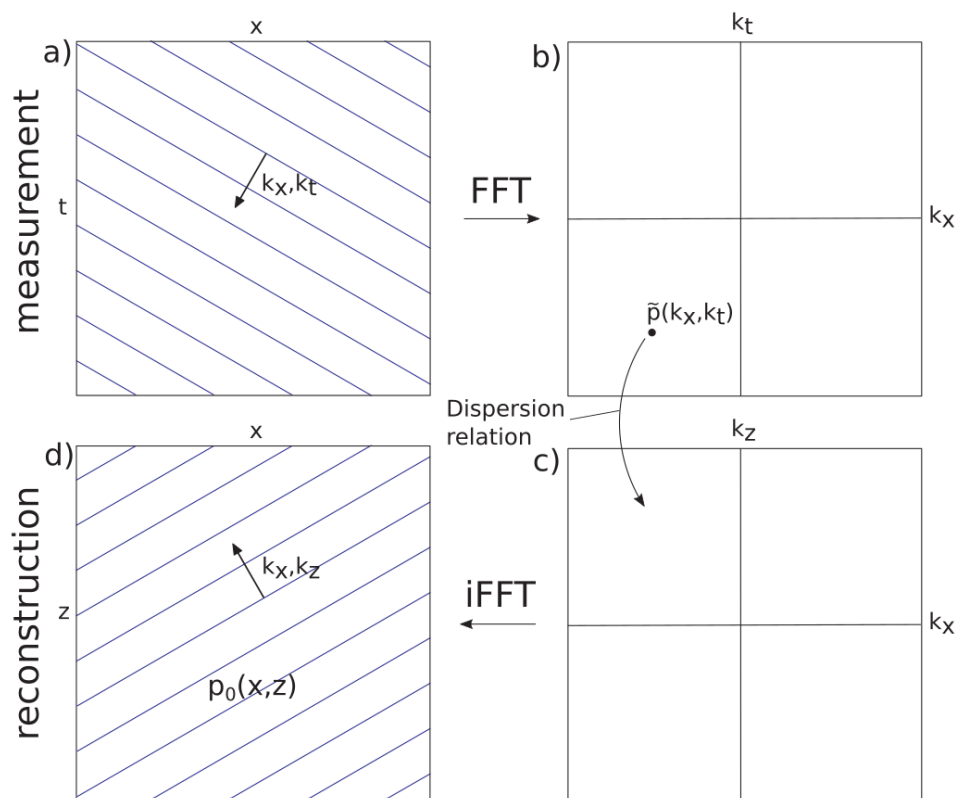


Figure 2.18.: Schematic showing the principle behind the Fourier domain reconstruction algorithm on a single plane wave. a) measured signal, b) signal in the frequency domain (FFT...Fast Fourier Transformation), c) reconstruction in the frequency domain, d) reconstructed final image (iFFT...inverse Fast Fourier Transformation) [43].

Moreover, it has been shown that the coherence factor does not alter the lateral resolution. An overview of some of the results is given in figure 2.19. Here two crossed gold wires were imaged using a photoacoustic microscope setup. Afterwards the different reconstruction techniques were applied and the outcomes were compared [43].

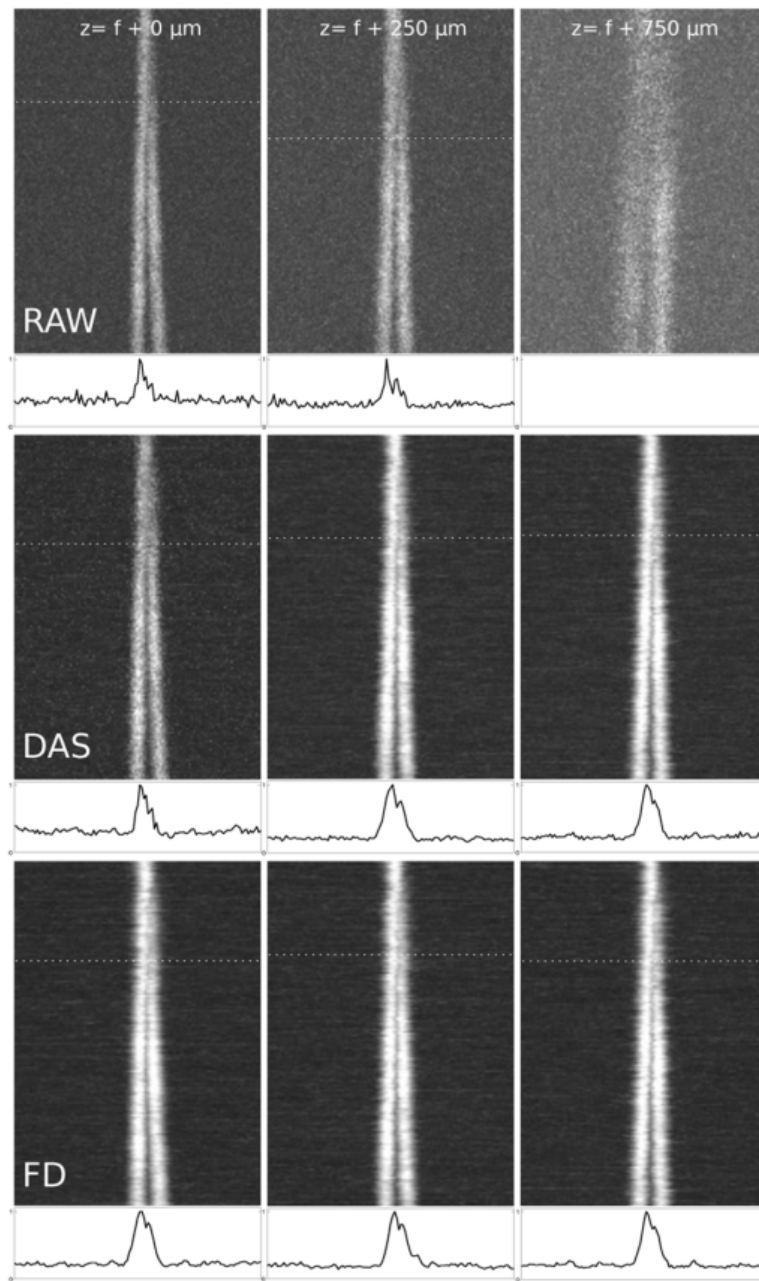


Figure 2.19.: *Maximum amplitude projections of the optoacoustic signal of gold wires in a scattering medium at different heights compared to the focal plane [43].*

3. Simulations for photoacoustic microscopy

The last chapter dealt with the theory of photoacoustic techniques in general and their advantages as well as disadvantages in particular. One of the main topics of this theory chapter was the treatment of numerical methods that can be used for simulating certain experimental processes.

Simulations have become a large part of physics, so much so that a whole area of physics is dedicated just to them, it is called computational physics. One of the reasons for this is the often cumbersome nature of performing experiments, which need a lot of time and preparation. Simulating some scenarios beforehand can drastically shorten the time spent on real world experiments, since configurations, which would probably not lead to any interesting results, can often be ruled out quicker. On the other hand, some setups can be optimized before building them, again saving some time.

Simulations can be performed numerous times, using the exact same set of parameters. This yields the opportunity for great predictability and very exact conditions, which can not be achieved in a real experimental environment. Having simulations that correspond to real world applications can therefore be helpful in finding experimental shortcomings and errors.

This chapter will now deal with such simulations, using the methods described in the theory chapter. This will be done by performing Monte-Carlo simulations to gain an understanding of the propagation of light inside of turbid materials and using k-space methods to simulate the propagation of soundwaves. Having dealt with both of those simulations separately, they will be combined to gain a more complete understanding of an photoacoustic microscopy setup and its properties regarding different samples. All of these simulations were programmed and performed in MATLAB¹.

¹The Math Works, Inc. MATLAB. Version 2020a

3.1. Monte-Carlo algorithm for light propagation in turbid media

This section will deal with the first part of the simulations, light from a laser hitting the sample and propagating through it, while encountering absorption and scattering effects.

3.1.1. Implementation of the algorithm

The program was written in the framework of object-oriented programming (OOP), in order to give the algorithm a suitable structure. This structure allows an interchangeability of parts of the simulation, which can aid the processing of many slightly varying configurations. There are three main classes for which objects can be created:

- A class describing the sample (`MC_phantom`)
- A class describing the laser beam (`MC_beam`)
- A class for performing the simulation (`MC_sim`)

While the first two are mainly descriptive, meaning that their main purpose is to hold information, the third one combines information from the other two, in order to perform calculations. A more detailed description of each class can be found below.

Phantom class

The phantom class is almost a purely descriptive one, holding all the information about the sample one wants to perform simulations on. For the calculations the sample is represented by three-dimensional matrices, containing several parameters, which describe the optical as well as acoustic properties of the sample. All of those matrices are of the same size and represent a geometrical distribution of these values. The geometrical extent of these matrices, in other words the size of the sample, including the distance of individual voxels to each other, is also stored in any object of the class `MC_phantom`, using vectors (x , y and z).

Detailed descriptions of the stored parameters can be found in sections 2.1 and 2.3. They are:

- absorption coefficient μ_a
- scattering coefficient μ_s
- anisotropy factor g
- Grüneisen parameter Γ
- speed of sound c
- frequency power law prefactor α_0
- frequency power law exponent y (only given as a scalar)
- materials density ρ

The four values on the right side can be left empty, which will lead to a simulation omitting any physical effects caused by them.

Although technically the inputs are not restricted, usually SI-units were used, in order to keep everything compatible with each other. This is true for the optical and acoustic parameters as well as for the vectors describing the dimensions (x , y and z).

Beam class

The next important class is the beam class (`MC_beam`). It stores the information about the laser beam. The stored variables mainly characterize the initial properties of the photon packets, which are used in the statistical approach to the light matter interaction (see section 2.2).

Contrary to the phantom class, objects from the beam class are also used to perform some basic calculations, as well as some calculations based on random numbers, which are utilized to randomize the initial photon packet configurations. A short overview of this will be given below.

The main properties of this class are:

- The shape of the beam (circular, ring or elliptical)
- Some parameters describing the geometry of the beam (dependent on the beam shape; see table 3.1)
- The initial weight of each photon packet (usually the default value of 1 is used)
- The wavelength λ of the used light
- The fluence H_{in} of the beam
- The area of the beam at the surface of the sample (calculated automatically from the beam parameters)
- The incident energy Q_{in} (calculated automatically using the area and H_{in})

The last two parameters are not defined by a user input since they can be calculated from the other variables easily. In theory, arbitrary beam shapes could have been implemented. The three chosen ones (circular, ring and elliptical) describe beams, which are commonly used in photoacoustic setups (see figure 2.12). Which input parameters are necessary for the respective beam geometry can be seen in table 3.1. While the circular and the ring-shaped geometries are self explanatory, the elliptical shape needs some explanation. It is assumed that the beam originating from the laser, after passing through a waveguide, is circular in shape. This beam then hits the surface of the sample at a certain angle, which causes the shape at this surface to become elliptical. This is the reason why the according properties were chosen as an input. Any effects due to the polarization of the light were neglected, as their impact on the results was assumed to be minimal for the use case at hand.

A graphical representation of this is shown in figure 3.1.

Another very important characteristic is the wavelength of the used light and the fluence of the beam (H_{in}). These two properties are connected since the ANSI limits for the use

Table 3.1.: *Necessary input values for different beam geometries.*

Circular	Ring-shaped	Elliptical
Wavelength	Wavelength	Wavelength
Radius	Inner radius	Radius
	Outer radius	Angle of incidence

of light in biomedical applications depends on the wavelength. Although it is possible to define the input fluence manually, omitting an input is often the best option, as the program defaults to the correct ANSI limit value for the chosen wavelength.

The main function of the beam class is, as was mentioned before, the generation of initial conditions for photon packets. For this purpose a method² was written, which is called `r_phot`.

This function takes some of the parameters discussed above, an object of the class `phantom` and the number of photons to generate as an input. The `phantom` object is necessary, as the function needs to know the dimensions of the sample, in order to generate the photons positions. These locations, together with the directions of the photons, are the outputs of the method. They are calculated by using random numbers and a parameterization for the circular and ring geometries, while the elliptical geometry was realized by using a rejection method. This yields results, which can be seen in figure 3.2, where a phantom with a surface of 1 cm^2 was used. From this figure, in particular part a) of it, the random distribution of photons becomes visible.

Simulation class

The final class, which needs to be discussed here is the simulation class itself. This class can be seen as a container, taking objects of the former mentioned classes and using them to perform the simulation. In detail, this means that `MC_sim` needs three input arguments:

- A phantom object
- A beam object
- The number of photon packets N_{photon}

In the end, one output can be gained by running the method `MC_sim.simulation`. This output is the energy density absorbed by the material, after the light has propagated through it, as was seen in section 2.3. This energy density Q is given in units of energy per volume (e.g. $\frac{\text{J}}{\text{m}^3}$).

²A method is a function specific to a class [44].

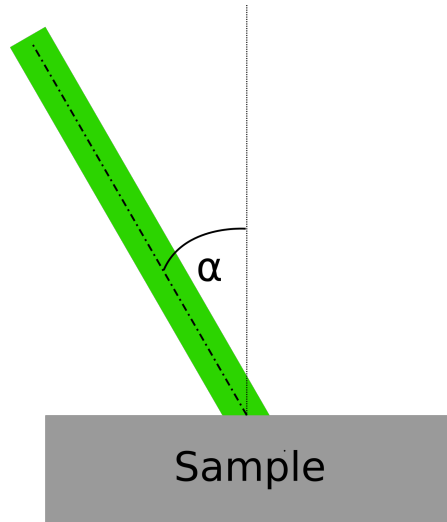


Figure 3.1.: *Graphical representation of a circular beam with an angle of incidence α onto the sample surface, yielding an elliptical shape at this surface.*

This quantity is gained by performing a calculation modeled after the algorithm described in section 2.2. It is implemented as a method of the simulation class and can be executed via `MC_sim.simulation`. Further, some small routines were implemented, which make the depiction of results more practical.

In some cases it might have been easier to just reference the beam and phantom objects, instead of including them into a new object. This would especially have saved memory. Nevertheless, it was decided that the benefit of having a one-object-structure, containing all the necessary information and thereby being able to save multiple combinations of phantoms, beams and number of photons separately, outweighed the memory saving aspect.

Simulation times vary by some amount, depending on the phantom and beam in question and of course the number of photons. The time it takes to simulate one photon packet is mostly dependent on the number of interactions of this photon with the phantom. Therefore, the exact optical parameters of the phantom have an effect on the simulation times. Since a thorough optimization of the algorithm was not a part of this thesis, no detailed study on the speed dependencies of the algorithm were carried out. Nevertheless, it should be noted that on a desktop machine³ usual calculations for 1×10^5 photons took several minutes. Although a parallelization of the algorithm is certainly feasible, the calculation times accomplished were good enough for the use case at hand.

³Intel Xeon CPU E5-1620 v3, 16 GB RAM, NVIDIA Quadro K2200

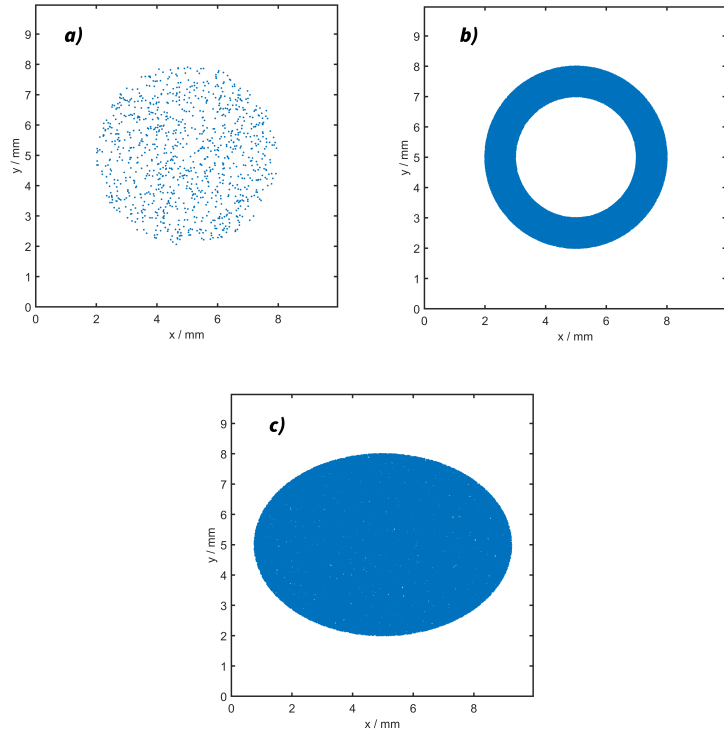


Figure 3.2.: *Positions of photons at the samples surface, for different beam geometries and different number of photons N_{photon} . a) circular geometry with a radius of 3 mm ($N_{photon} = 1 \times 10^3$), b) ring geometry with an outer radius of 3 mm and an inner radius of 2 mm ($N_{photon} = 1 \times 10^5$), c) elliptical geometry with a beam diameter of 6 mm and an incident angle of 45° ($N_{photon} = 1 \times 10^5$).*

3.1.2. Discussion of selected simulations

In order to gain a more thorough understanding of this part of the simulations, some results will be presented and discussed. In general the algorithm was written in a way, which allows a quantitative analysis of any material, given some real world parameters. Since this thesis is tightly connected to the scientific project OMiPPAB, which started in 2020 at the Karl-Franzens-University of Graz, specific parameters will be chosen for most of the simulations. The main goal of this project is to examine photoacoustic microscopy as an imaging approach in a biomedical setting.

Parameters used in simulations

A special interest is put on human organs, which are to be transplanted and therefore, need to be monitored closely, while being preserved in a perfusion system. One organ of

Table 3.2.: Values for the absorption coefficient μ_a , the scattering coefficient μ_s and the anisotropy factor g , for liver tissue, blood and the contrast agent ICG, with a concentration of $650 \mu M$ in plasma, at three different wavelengths [46, 47, 48].

λ / nm	$\mu_a / \frac{1}{\text{mm}}$			$\mu_s / \frac{1}{\text{mm}}$			g		
	Liver	Blood	ICG	Liver	Blood	ICG	Liver	Blood	ICG
532	0.78	21.96		10.12	68.62		0.95	0.96	
800	0.28	0.34	15.52	8.76	81.55		0.97	0.98	
1064	0.28	0.47		7.96	66.72		0.97	0.97	

particular interest is the human liver. This is why acoustic and optical parameters for liver tissue and for blood will be used during these simulations. These parameters are of course wavelength dependent and also vary slightly from source to source [45]. Some important values can be seen in table 3.2 [46, 47]. This table also contains the values for a popular contrast agent: Indocyanine green (ICG) [48]. ICG is only used at certain wavelengths and is assumed not to alter the scattering coefficient and the anisotropy factor. This is the reason for the omission of many values regarding it in table 3.2. The values have been taken from interpolated spectra, the uncertainties are hard to estimate but one should not expect more than two digit accuracy.

The table gives some insight into the tissues properties, which can be exploited, in order to perform photoacoustic measurements.

Taking a look at the values for a wavelength of 532 nm, one can immediately see the large difference between the absorption coefficients for blood and liver tissue. Since blood has an absorption, which is larger by two orders of magnitude in this regime, the theory would predict much larger energy depositions in regions where blood is present, compared to ones where bloodless liver tissue is the main medium. This increased absorption should then also yield a contrast for those regions.

Further, the scattering coefficient in this regime is also larger for blood by a significant amount, which aids the distribution of photons in blood filled regions. Concerning the anisotropy factor no real difference can be seen, for none of the examined wavelengths. Nevertheless, it can be noted that most photons will be scattered in the forward direction since $g \approx 1$.

A slightly different picture presents itself when going to longer wavelengths. Here the difference between the absorption coefficients of pure liver tissue and blood are nearly the same, which should mean a loss in contrast. However, when adding ICG to the blood, the absorption can be influenced by orders of magnitude. This again boosts the contrast by a large amount, hence the name contrast agent.

Simulation results

Using the parameters discussed in the last section, especially the values in table 3.2, some simulations were run to show the behavior of the algorithm graphically. In order to do so, a phantom had to be designed first.

This phantom, as all phantoms, which can be used for the simulation, is a cuboid. In this case it had the following dimensions: $4 \times 4 \times 2.8 \text{ mm}^3$. It was divided into a grid with the following number of grid points: $256 \times 256 \times 168$. This in turn gives a distance of $16.9 \mu\text{m}$ between voxels in each direction. The number of photon packets for each simulation was set to 1×10^6 .

The base matrix, in other words the bulk of the phantom's material, was set to be made up of liver tissue, with the according optical parameters. This stayed the same throughout the simulations. For this first calculations, simple features were thought of, which can easily be distinguished from the bulk material. Spheres of equal size (radius = 0.17 mm) were set in different heights ($z = \{0.5 \text{ mm}, 1.4 \text{ mm}, 2.5 \text{ mm}\}$), centered with regard to the incoming beam. These spheres were given the optical properties of blood or blood with ICG, according to table 3.2. The values with the contrast agent were only chosen for a wavelength of 800 nm , since, as mentioned before, this is the working wavelength for this particular chemical. A general depiction of this phantom, before any calculations have been performed, can be seen in figure 3.3 at the top left.

Initially, the beam was chosen to have a circular geometry with a radius of 0.5 mm . Three different wavelengths were investigated ($\lambda = \{532 \text{ nm}, 800 \text{ nm}, 1064 \text{ nm}\}$). The results of these simulations can be seen in figure 3.3, where the logarithm of the absorbed energy is depicted. These depictions show the mean over ten slices, located in the middle of the output matrix.

It can clearly be seen that there is a contrast between the base material and the spheres placed inside of the sample. The spheres have absorbed much more energy, for all three cases, which was expected. An important thing to note is that the cases c) and d) would look very similar, if no contrast agent had been used. As became apparent in the last section, this contrast agent makes a large difference for the optical parameters, this is now confirmed by the simulation leading to case c).

A detailed view of the situation in b) can be seen in figure 3.4. This graph shows the absorbed energy with respect to the distance inside of the sample, at the center of the matrix, regarding the x and y coordinates (dashed green line in figure 3.3 b). Three distinct peaks are visible, which denote the outer edge of the spherical features inside of the sample. The height of these peaks differs by a large amount. This can be attributed to the absorption inside of the material, which should roughly follow the Lambert-Beer law. It is also clear from this that the spheres are not uniformly lit, which makes an exact reconstruction more difficult. This effect is more pronounced when operating in a setting, where the absorption is very large, since many photons will be absorbed by the shell of the sphere, before entering the center of it.

This graph can also be used to approximate the temperature increase caused by the absorption of energy by the material. This is an important parameter in biomedical applications, since a large increase in temperature would cause damage to the tissue. This temperature rise can be approximated by the following formula [49]:

$$\Delta T = \frac{Q}{C_p \rho}, \quad (3.1)$$

where Q is the absorbed energy density, C_p is the specific heat capacity and ρ is the materials density. Using the values gained from the simulation and some values from literature ($Q = 3 \times 10^{-3} \frac{\text{J}}{\text{mm}^3}$, $C_p = 3590 \frac{\text{J}}{\text{kgK}}$ [50] and $\rho = 1060 \frac{\text{kg}}{\text{m}^3}$ [51]) one gains an increase of $\Delta T = 0.79 \text{ K}$. This momentary temperature difference is of no harm to biological tissue.

Another important thing to learn from these initial light propagation simulations, is the penetration depth of the laser beam. Naturally this highly depends on the absorption of the material. In the presented example the laser beam with a wavelength of 532 nm does not reach into the material far enough to really light up the third sphere. On the other hand, the contrast for the first and, to some extent, the second sphere is quite good. Looking at case d) this situation has changed to the opposite. The beam penetrates way beyond the third sphere but the contrast is reduced by a large amount. Case c) seems to fulfill both demands quite well but it should again be mentioned that it can only be achieved by using a contrast agent, which is not feasible in every situation. Overall a decision on the right setting has to be made, mainly considering the purpose of the examination.

One last simulation has been run, using a slightly different beam geometry. For figure 3.5 the laser beam was shone onto the sample at an angle of 15° , otherwise the parameters were equal to case c) from figure 3.3. Generally no huge changes are visible for this simulation, compared to the ones before. The slight shift of the intensity, attributed to the angle of incidence quickly loses its importance, since the scattering results in a characteristic pear shape after approximately 1 mm.

One further aspect, which can be seen for all simulations, is the shadowing effect. Since the features absorb a lot of energy and the scattering is mainly focused in the forward direction, there are regions behind the spheres, where there is a lack of absorbed energy. This can play a role, when features lie close together. Features residing inside of these shadowed regions may not receive enough energy to be properly lit up.

3.2. Wave propagation simulation using the k-wave toolbox

Having dealt with the light propagation simulations, this section will focus on the acoustic waves propagating through a medium. Since the initial conditions for this propagation are given by the simulations discussed in the last section, some of the knowledge gained by performing them will also be used during the following discussion.

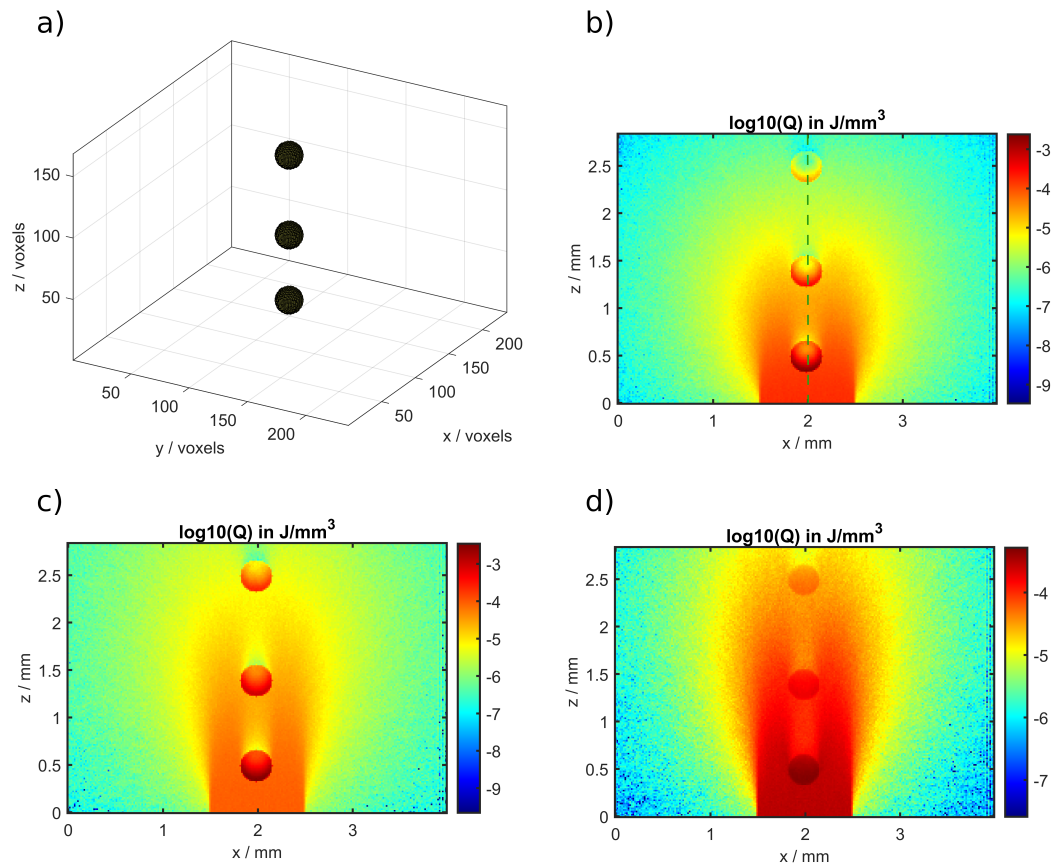


Figure 3.3.: a) Three-dimensional depiction of a phantom with three embedded absorbent and scattering spheres within a differently absorbent and scattering medium. b), c) and d) logarithm of the absorbed energy density Q , for a circular beam shape, with a radius of 0.5 mm, at 532 nm, 800 nm (including ICG) and 1064 nm, respectively. The spheres in c) differ from the ones in a) and b), regarding their optical properties.

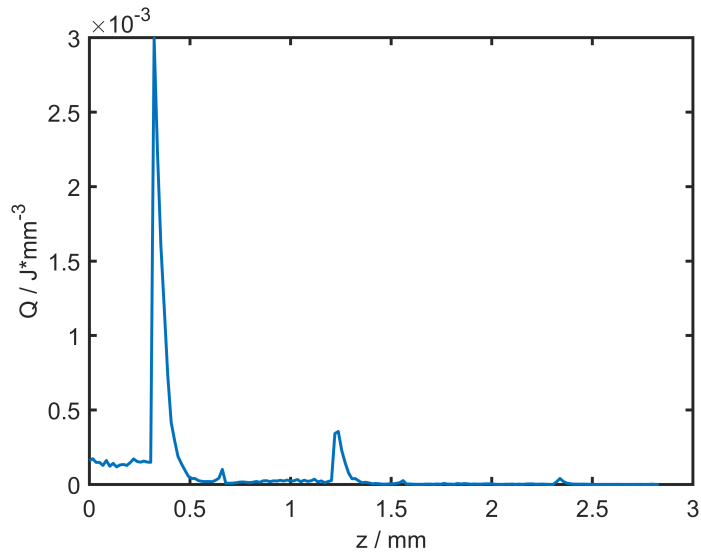


Figure 3.4.: Absorbed energy density Q along a line through the center of the sample in z -direction. Taken from the simulation depicted in figure 3.3 b) (dashed green line).

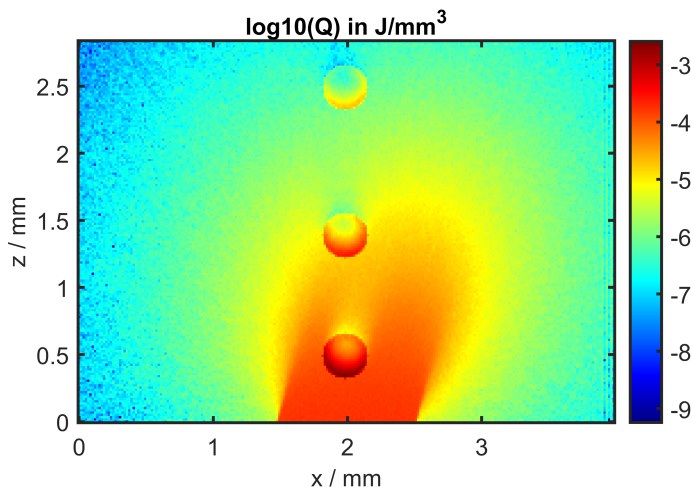


Figure 3.5.: Logarithm of the absorbed energy density Q , for the three-sphere sample at a wavelength of 532 nm under an incident angle of 15° .

Further, this section will have a tight relation to the actual experiments. This is caused by the vicinity of the two areas. Both the actual experiments and the simulations of the pressure waves moving through the tissue are performed in order to gain time-dependent pressure signals. A detailed description of this can be found in sections 2.3 and 2.4. This is the reason why this part will start with an overview of the programming, which was done to store measurement data in a structured manner. The resulting algorithms were used for the simulation as well as for actual measurements.

In the following some basic simulations will be discussed, in order to gain an understanding for the tools that were used for this part of the thesis. These will further be used to perform more sophisticated simulations on datasets, similar to the ones discussed in section 3.1.

3.2.1. Implementation of the method

Most of the algorithm, which was used for the following simulations, was introduced by Treeby et al. and is available as a MATLAB toolbox [19, 22]. Nevertheless, some work went into the design of a structured storage class for some of the more complex three-dimensional results.

Measurement class

As mentioned already, this class was not purely meant for the simulation of pressure signals but was initially created with the experimental setup in mind. This is an important aspect when looking at some of the features, which are included in the class `PAM_mes`.

This class serves two main purposes. On the one side, it's objects are used to store recorded pressure signals. On the other side, these stored signals can be reconstructed according to algorithms presented in section 2.6.2 via methods, which were implemented into the class. How this was realized in detail will be discussed in a separate section.

The main properties of the class are the following:

- The mean speed of sound in the sample
- Three vectors describing the positions of the captured datapoints in the x, y and z directions
- A vector describing the time dimension of each recorded signal (this is tightly related to the space vector in the z -direction)
- The depth of the focus plane
- Three-dimensional matrices storing the recorded and reconstructed signals
- A matrix for storing the energy of the laser pulse at each spatial position (can be used for improving the signals)

Further, a dimension structure can be defined that holds the units for the length and time dimensions. These are used for plots, which are directly generated from an object.

Since the class was written with an experimental setting in mind, the creation of an object is not intended to be done by simply passing all of the above arguments to the construction method. An object is first initialized by only defining the dimensions of the resulting matrix, the focus-depth and the speed of sound. This, at this point more or less empty object, is then filled with captured signals. It is possible to capture all signals at once and pass the whole matrix to the corresponding object. This is often done when performing simulations, since previously recorded signals are still used in the calculations.

For experiments on the other hand, an appending method was written (`PAM_mes.append_bscan`). This enables the user to append one B-scan after the other to the full matrix. There are some benefits to performing the storage in this way. The recorded signals often need a large amount of memory, it is therefore convenient to store them iteratively. Further, in the event of any failure during the measurement, all the B-scans up to the point of failure are still saved and can likely be recovered.

In addition to the properties and methods discussed above, some methods for representing the data graphically were implemented. These will not be discussed here in detail, as they were not of importance for the general usage of the class.

The source code of this class, not including the aforementioned representation methods, is depicted in appendix A. This includes the Fourier domain algorithm, which was implemented for the reconstruction of the signals and was discussed in section 2.6.2 (see appendix B).

Using the k-wave toolbox

Having discussed the way in which signals can be stored, the next step is to generate those signals via computer simulations. All parameters necessary for this are included in any simulation class object. Taking a detailed view, the acoustic parameters are stored inside of the phantom object, which describes the whole sample. The initial pressure distribution can be gained, after running the Monte-Carlo light simulation on the simulation object, by multiplying the absorbed energy Q by the Grüneisen parameter Γ , as was discussed in section 2.3.

A very detailed description of how to use these values for calculations with the Matlab k-wave toolbox can be found in the corresponding manual [22]. Nevertheless, a brief outline of the necessary steps shall be given here:

1. A computational grid has to be defined. It holds the information about the dimensions of the domain the calculation will be run on, as well as the number of timesteps and the time between them. This forms the basis for all computations.
2. A medium structure has to be defined, which essentially is made up of all the parameters included in the phantom class. `medium.sound_speed`, `medium.density`, `medium.alpha_coeff` and `medium.alpha_power` correspond to the speed of sound

- c , the materials density ρ , the frequency power law prefactor α_0 and the frequency power law exponent y .
3. A sensor geometry has to be defined. In general each voxel of the calculation grid can be defined as a singular sensor point. In order to simulate an extended sensor, an array of such singular voxels is used. After the simulation the mean value of all signals for each point in time is calculated.
The position of each sensor-voxel is defined in a binary three-dimensional matrix, which has the same size as the computational grid.
 4. The initial pressure distribution can easily be calculated from the former light-interaction simulations, as was already briefly mentioned ($p_0(\mathbf{x}) = \Gamma Q(\mathbf{x})$). It could of course also be given in other ways, depending on the problem at hand. Once again, it has to be given as a three-dimensional matrix, being of equal size as the computational grid.
 5. All of the above parameters have to be passed to the function actually performing the simulation (`kSpaceFirstOrder2D` [for two-dimensional problems] or `kSpaceFirstOrder3D` [for three-dimensional problems]). These functions can take a wide array of optional arguments, all of which are described in some detail in the k-wave documentation [22]. One important functionality is the ability to run the calculations in single precision, which is most often precise enough and they can even be run on a GPU instead of the CPU, which yields way faster computation times.

These steps can perhaps be comprehended more easily, when looking at figure 3.6, where all necessary components are depicted with the corresponding fields of the objects. Some of these fields are not obligatory and might therefore have not been discussed to this point.

Acoustic parameters used for simulations

Analog to the optical parameters, which were discussed in one of the preceding sections, also acoustic parameters for the tissues of interest have to be assumed. This was again done by thorough research of existing literature on the properties in question. Table 3.3 shows these values. It has to be noted at this point, once again, that ICG was assumed not to alter the acoustic properties in any major way, and is therefore not a real concern for this part of the simulations. The values depicted here are the exact values used in the calculations, a detailed error analysis proved to be difficult and was therefore omitted. Before some sample simulations will be performed, which are intended to aid the understanding of the underlying method, a quick analysis of the parameters presented in table 3.3 shall be performed.

These parameters have a different relation to each other than the optical parameters do. It can be seen quite easily that most of the values for liver tissue and for blood lie in the same region. They are in fact so close to each other that the difference might fall into

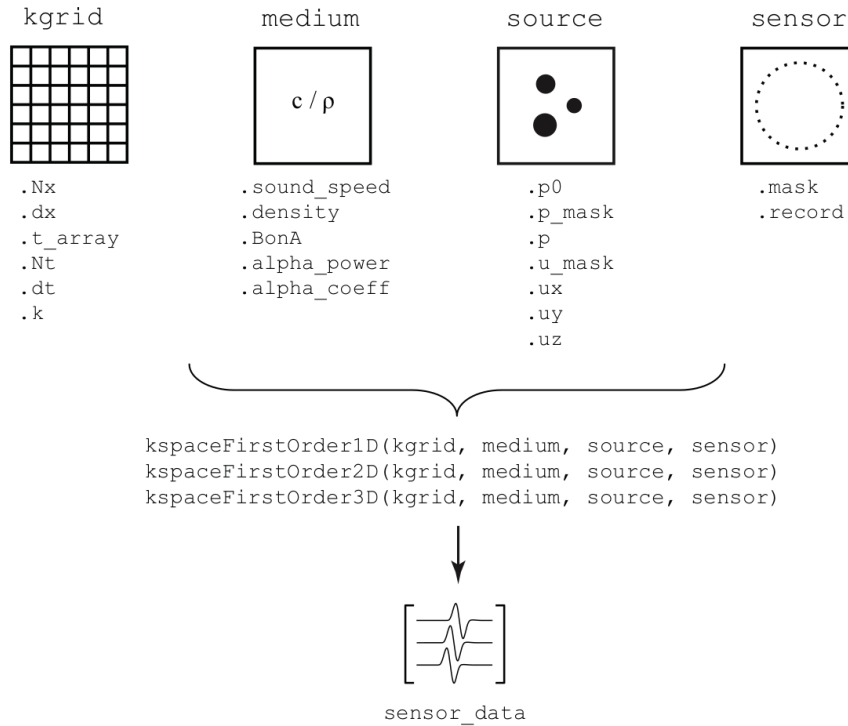


Figure 3.6.: Schematic overview of the input structures necessary for calculating the wave propagation using the k-wave toolbox [22].

the uncertainty of the values, especially considering their dependence on environmental factors such as the ambient temperature. Due to this close proximity they can basically be seen as equal for both, blood and liver tissue.

While equal values for the optical parameters would not allow any measurements to take place, since their difference is the basis for contrast, the small difference between the acoustic parameters ensures that almost no reflections and other unwanted effects at the boundaries take place. This in turn means that the generated pressure waves can travel through the media almost as if they were homogeneous, which was one of the assumptions made in section 2.3. More importantly this also plays a major role in the reconstruction of the signals, as some of the same assumptions were made when deriving the reconstruction methods discussed in section 2.6.2. It can therefore be said that the assumptions, which were made in the theory section, were justified for the special case at hand.

If not stated otherwise, these values will be used whenever the corresponding materials are simulated. The next section however, will deal with very simple calculations in two dimensions, as to show the general function of the k-wave toolbox in practice. One of the following sections will be dedicated to the simulation of start to end simulations, including both, the optical and the acoustic parts.

Table 3.3.: *Acoustic parameters for liver tissue and blood, according to various sources in literature. With Γ being the Grüneisen parameter, c_0 the speed of sound, α_0 the attenuation power law prefactor, y the attenuation power law exponent and ρ the materials density.*

	Liver	Blood
Γ	0.19 [52]	0.17 [53]
c_0 / $\frac{\text{m}}{\text{s}}$	1590 [54]	1530 [51]
α_0 / $\frac{\text{dB MHz}}{\text{cm}}$	0.52 [55]	0.14 [51]
y	1.2 [51]	1.2 [51]
ρ / $\frac{\text{kg}}{\text{m}^3}$	1050 [56]	1060 [56]

3.2.2. Exemplary simulations

A simple simulation in two-dimensional space was chosen to show the general functionality of the k-wave toolbox. This of course can easily be extended to three dimensions, as will be shown later on. Nevertheless, the graphical representation of the simulations is a lot simpler in lower dimensional spaces, this is the reason for the simplifications in this example.

Following the steps from the last section, these parameters were chosen for the simulation:

1. The computational grid was decided to have 256×128 grid points, with a distance of $50 \mu\text{m}$ between them in each direction. The calculation encompassed 600 time steps, with a stepsize of 10 ns, which yields a total physical time of $600 \cdot 10 \text{ ns} = 6 \mu\text{s}$.
2. The medium was chosen to be water with a homogeneous sound speed of $1500 \frac{\text{m}}{\text{s}}$ and a density of $1000 \frac{\text{kg}}{\text{m}^3}$. The absorption was selected to have $\alpha_0 = 0.75 \frac{\text{dB MHz}}{\text{cm}}$ and $y = 1.5$.
3. The sensor was assumed to be a line sensor, made up of individual point like sensors (261 of such point sensors were used). It was put at a distance of 21 grid points from the boundary. This line like array can also be interpreted as a single sensor moving along one dimension and thereby obtaining a B-scan image.
4. Three circular discs were used as pressure sources. Each with a radius of 0.25 mm and an arbitrarily chosen initial pressure of $p_0 = 5 \text{ Pa}$. This value had no physical background, it was mainly chosen to gain results which can be plotted easily. The sources were placed at a distance of 2 mm to the sensor, with a distance of 3 mm between each of them.
5. The function `kspaceFirstOrder2D` was used to run the simulation with single precision variables. A movie was recorded during the simulations⁴.

⁴See the full animation at http://brandmueller.at/physics/pai_poster/

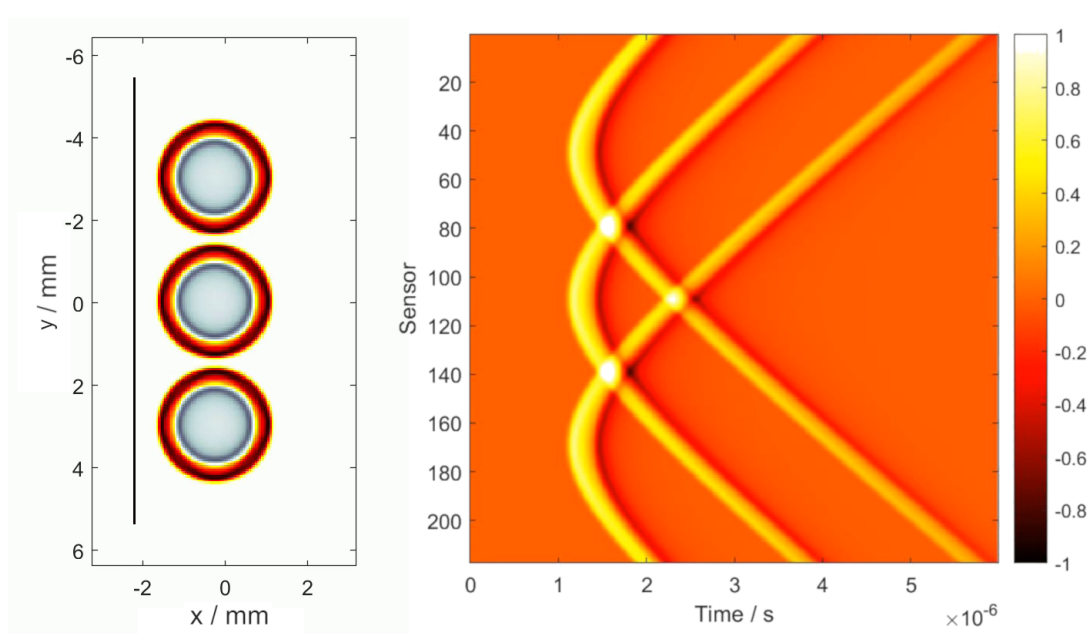


Figure 3.7.: *Results of a wave propagation simulation in two spatial dimensions. Depiction of the wave-fronts at some time $t > 0$ (left) and normalized pressure-signals recorded by the sensors (right). The black vertical line in the left picture indicates the position of the line detector relative to the pressure sources.*

Figure 3.7 shows some of the results from this simulation. The left side is a screenshot from the recorded movie, less than 1 μ s after the initialization. It can be seen quite easily that the pressure waves have not yet reached the sensors.

The picture on the right side shows the normalized pressure signals of all 216 sensors with respect to time. Close inspection reveals that each initial source yields one hyperbola. The peaks of the three hyperbolae lie where the pressure waves hit the sensors first and denote the real position of the pressure sources. This form of the signals was expected, it was derived in section 2.6.1.

To drive this point further one can take a look at the recorded signal from one single sensor, which is depicted in figure 3.8. This sensor sits at position 50 in figure 3.7, placing it at a y-position of -2.9 mm. Nevertheless, the signal shows three distinct peaks, one for each pressure source. The amplitude of those signals gets smaller over time due to the distance from the sensor. This is also the reason for their time delay.

All the results of this simulation coincide with the expected outcomes derived in the theory chapter.

This simple simulation can of course only show a very small part of the capabilities of this toolbox. Nevertheless, some insight into the inner workings of such simulations have been gained that can be used for further, more complex, calculations.

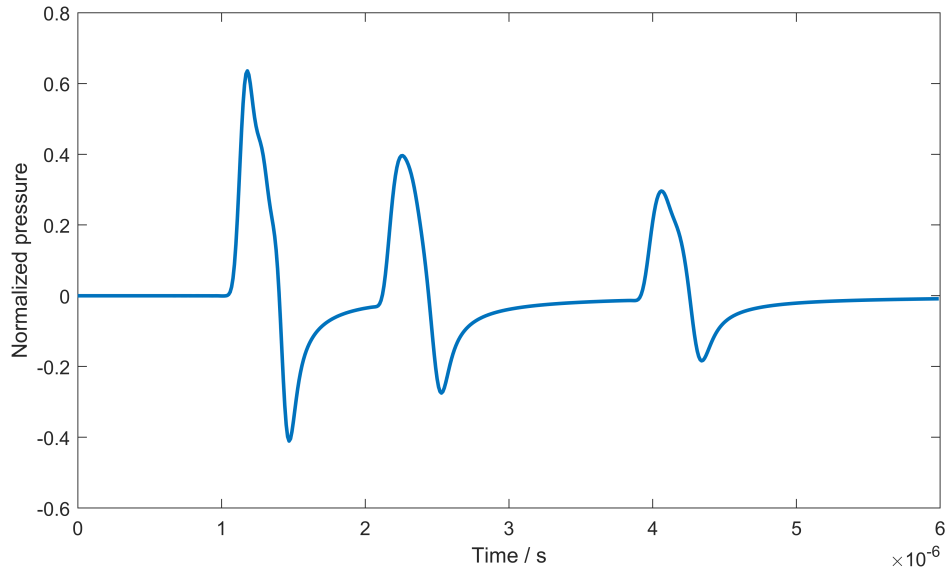


Figure 3.8.: *Time dependent normalized pressure signal of one distinct point-like sensor. The signal was taken from the sensor at position 50 in figure 3.7.*

3.2.3. Comparison of a simulated signal with a measured signal

One further thing, which shall be discussed here, is the comparison of simulation results with real measured signals. The experimental setup is described in detail in section 4.1. It was used to measure one signal, stemming from a highly absorbing, uniform sample. The result of this measurement can be seen in figure 3.9.

The simulated signal was generated by running the k-wave toolbox using a focused sensor. A detailed description of this sensor setup can be found in section 3.4.2. The initial pressure distribution was assumed to be in the form of a uniform sphere, with a diameter of 0.5 mm and an initial pressure of 1 kPa. This sphere was placed in the focus spot of the sensor and the simulation was run long enough to capture the entire signal, which is depicted as the blue curve in figure 3.10.

Although this pressure distribution does not mimic the experimental setting perfectly, it should suffice for a comparison.

The simulated signal resembles an N-shape signal, which is to be expected [49]. However, this signal does not match the experimentally attained signal. This is mainly attributed to the fact that the ultrasound transducer used in the experiment has a frequency dependent response, which the sensor elements in the simulations usually do not.

This transducer property can be introduced by convolving the signal gained from the simulation with a function modeling said frequency dependence. This is equivalent to multiplying the Fourier spectrum of this signal with the convolution kernel. Both, the spectrum of the simulated signal and the used convolution kernel, in this case assuming

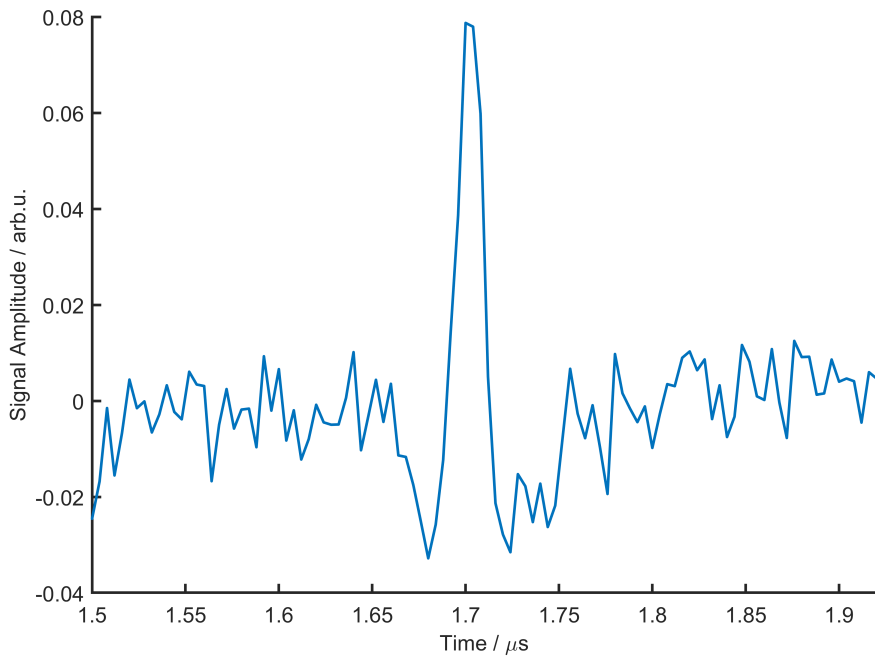


Figure 3.9.: Experimentally measured pressure signal captured from a highly absorbing sample, using the setup described in section 4.1.

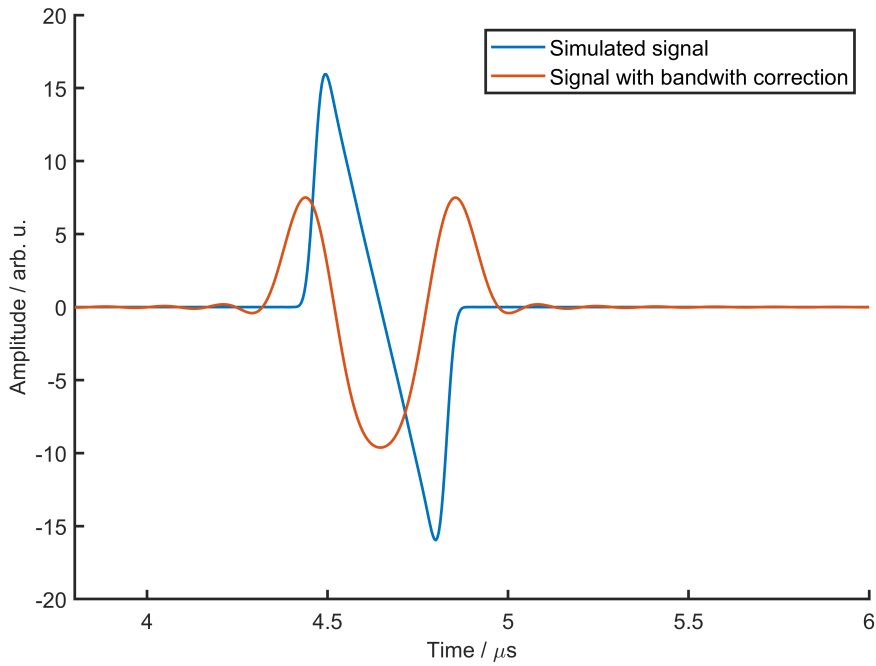


Figure 3.10.: Pressure signal simulated for a spherical initial pressure distribution using a focused sensor. The sensor being the same as in section 3.4.2.

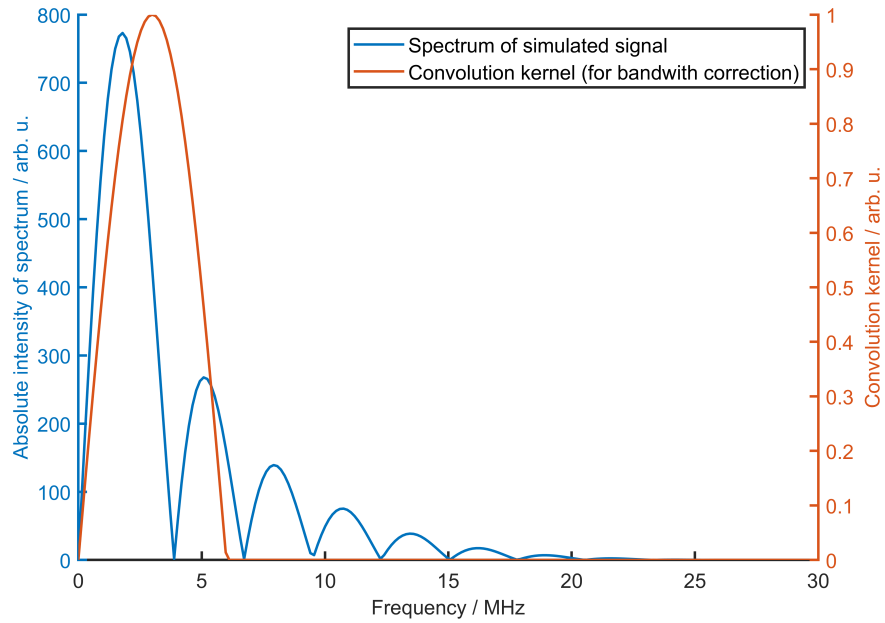


Figure 3.11.: *Fourier spectrum of the simulated signal and the used convolution kernel.*

a center frequency of 3 MHz and a FWHM of 4 MHz, are depicted in figure 3.11. These values do not coincide with the ones of the real transducer (center frequency 50 MHz with a bandwidth of 75%), but were chosen with respect to the simulation.

Applying this kernel in the frequency domain and performing the back transformation into the time domain, one gains the orange signal depicted in figure 3.10. This result resembles the experimentally obtained signal to a large degree, albeit being inverted, which has no physical meaning.

By this it was shown that the wave propagation simulations do in fact deliver results comparable to experimental signals. Although it has to be stated, that the frequencies supported by most of the simulations were somewhat lower than the ones which were worked with during the experimental part of the thesis. This however, should have no effect on the general statements made by these calculations.

3.3. Artifact correction using a Fourier domain algorithm

Having seen what signals are to be expected, the next step is to improve the quality of those signals. Looking at the example with three circular discs, it is obvious where the original discs were, even though the generated signals are distorted to some degree. This of course changes when more complex features have to be examined, since the gained signals will no longer show the clear hyperboloids of simple structures. Hence, an algorithm is necessary to regain the original structure of a sample. How this program

works in theory was discussed in section 2.6.2 and will therefore not be repeated in detail. Nevertheless, a short explanation of the theories implementation into the existing program structure and a simple example of the algorithms effect shall be given here.

3.3.1. Implementation of the algorithm into the existing framework

Since the algorithm should work on measured signals, it was implemented as a method to the measurement class (`PAM_mes`). All necessary input parameters are already given by this class, therefore, the method takes no additional information from the user, neither does the function have an output which the user can directly assign to a variable. The reconstructed signals get stored inside of the measurement object itself (`PAM_mes.image_rec`). This approach was mainly chosen due to its ease of use. A recorded measurement can be directly reconstructed with one command.

One parameter, which is of great importance for this reconstruction and that shall be mentioned explicitly, is the depth of the focal plane. The reconstruction relies heavily on this distance being set correctly. While it might be given by the used setup in some cases, it is often necessary to check the focal plane using B-scan images or other parameters for reference.

3.3.2. Exemplary reconstruction of simulated data

How this algorithm works shall be presented in this section, using a simple example, consisting of four pressure sources inside of a volume. This of course is once more a quite crude representation of an actual sample, but it is nevertheless insightful to use it in order to gain some understanding of the mechanism.

First, the signals had to be simulated, which was done using the k-wave toolbox. For this case a three-dimensional computational grid was chosen ($256 \times 256 \times 256$ grid points [including the PML layers] with a distance of $50 \mu\text{m}$ between the points in each direction). The parameters for the medium were the same as for the simulations in section 3.2.2 ($c_0 = 1500 \frac{\text{m}}{\text{s}}$, $\rho = 1000 \frac{\text{kg}}{\text{m}^3}$, $\alpha_0 = 0.75 \frac{\text{dB}}{\text{MHz cm}}$ and $y = 1.5$).

The four pressure sources were represented as spheres, which were placed at various positions inside of the computational domain⁵. A representation of this initial condition can be seen in figure 3.12. The spheres had a radius of 0.25 mm and the initial pressure was set to be $p_0 = 5 \text{ Pa}$.

Special care had to be taken regarding the sensor array used for this simulations, as it had to be chosen in a way, which emulates the focal plane of a focused sensor correctly, in order to achieve the „desired“ artifacts. This was done by regarding the focused sensor as an array of point sensors in the focal plane, which is in accordance to the virtual detector used during the derivation of the artifacts. This can also be seen in figure 2.16, where

⁵Special care has been taken as to not place them inside of the perfectly matched layer.

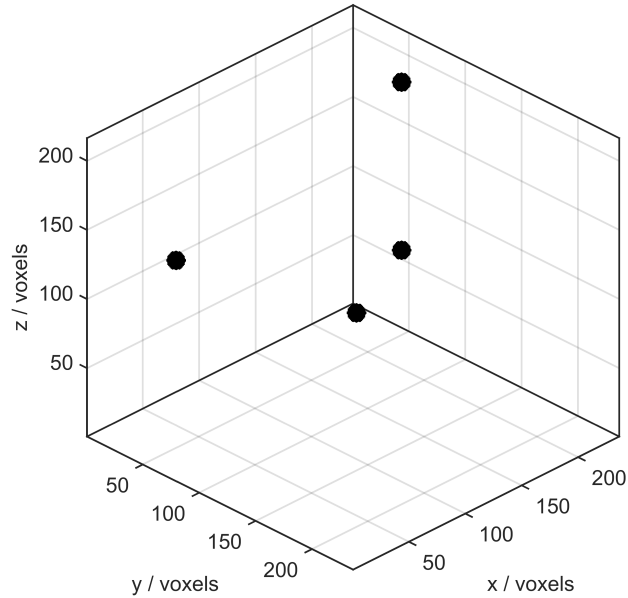


Figure 3.12.: *Three-dimensional depiction of the four spheres used as pressure sources.*

the cone of the detection area is also indicated.

Since k-wave does not support directed sensors in three dimensions, the used point sensors detected signals from all directions. This means that the depicted cone would have an opening angle of 180° . Using real sensors this would of course not be possible, since the numerical aperture is always limited in some way.

Nevertheless, a plane of voxels in the center of the z-axis was chosen as sensor points, detecting signals from all spatial angles with equal intensity. In order to achieve the right time delay for both, the space above and below the virtual sensor, the volume was split into two half-spaces. Since the actual sensor would be sitting above the whole volume, this allowed for some manipulation of the time array. This shifting and flipping of the time dimension for the lower and upper half-spaces, respectively, ensured that the final signals resembled those of an actual measurement as closely as possible, keeping in mind that some estimations have been made along the way.

The results of these simulations can be seen in the top row of figure 3.13, where maximum amplitude projections (MAPs) have been plotted for three directions. At first glance it seems like the spheres have vanished. This is of course caused by the extreme conditions mainly presented by the large angle of incidence, which can be detected from each sensor in the sensor array. As can be seen in the second and third MAP in this row, the hyperboloids stretch all the way to the edges, since the signals from the corresponding spheres get even to the most distant detectors.

Something else, which can be seen quite clearly, is that the features distance to the focus plane is of tremendous importance for the initial resolution. Looking at the first MAP in the top row (representing a MAP in the z -direction), one feature seems to be a lot clearer than the other ones. This sphere is the one closest to the focus plane and is therefore depicted quite well. Two spheres, on the other hand, nearly seem to vanish, which is caused by their distance to the virtual detectors, causing the signals to spread before reaching them.

These unwanted effects can be reversed by using the algorithm described before. The results of this can be seen in the bottom row of figure 3.13. The hyperboloids are nearly gone and most of the spheres were reconstructed quite well. One sphere, lying at $z \approx 10.5$ mm and $y \approx -4$ mm was not well reconstructed. The main reason for this was that most of the signal coming from this feature did not reach the sensors. This „cutting“ of the hyperboloids is generally one of the main reasons for artifacts, which remain after applying reconstruction methods.

In this short section it was shown that the implemented algorithm actually serves its intended purpose and is therefore capable of reconstructing the original pressure distribution p_0 from distorted signals, stemming from focused sensors. The simulations are in accordance with the theory, as far as it was tested here. These small test have no claim to completeness but it was possible to show the general idea behind the reconstruction algorithm.

3.4. Results of complete simulations

After finishing the discussion on the steps necessary for performing simulations of photoacoustic microscopy individually, this sections topic is the conduction of such simulations as a whole. This was the initial goal of this chapter, since it should give some insight into the experimental parameters and on how the final results depend on them.

There are different ways in which these individual steps can be performed but the main principle follows the order of the steps presented above chronologically. First, the medium is described with all its parameters, these are not changed during the full simulation. After that the first step is to perform the light propagation via the Monte-Carlo algorithm, which yields an initial pressure distribution, as was described in section 2.3. This pressure distribution can subsequently be used for the acoustic simulation with the k-wave MATLAB toolbox. From this the desired signals, which would similarly be measured in real experiments, are gained.

These signals are finally reconstructed by the Fourier domain algorithm that was already described in theory, including the presentation of some examples.

There are a lot of parameters, which can theoretically be adjusted during these simulations, as became apparent during the discussion of the algorithms. Since this thesis is mainly concerned with the treatment of biological tissue (especially the human liver), the properties presented in sections 3.1.2 and 3.2.1 were used throughout the simulations.

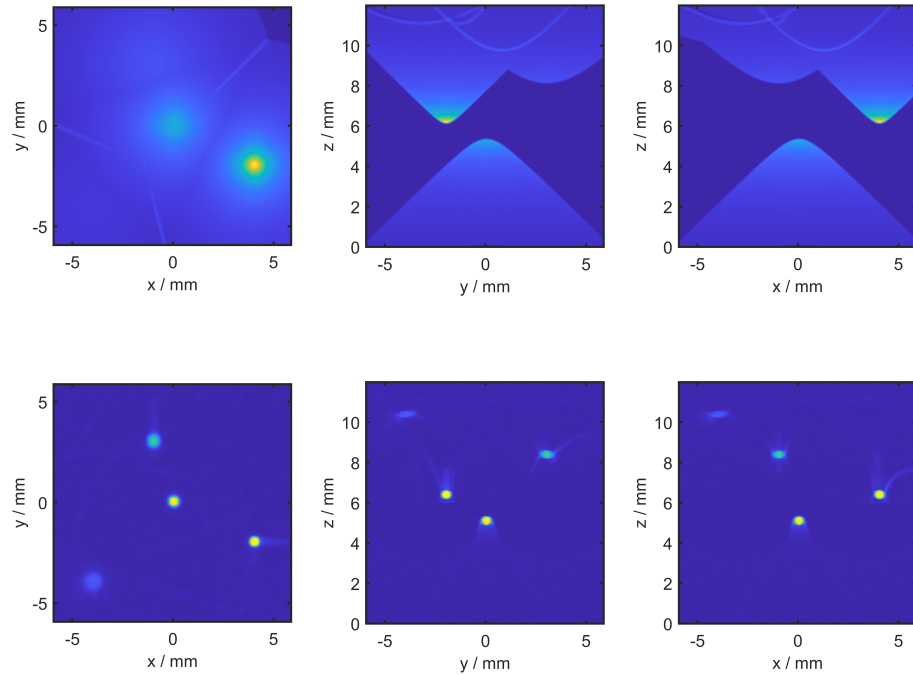


Figure 3.13.: *Maximum amplitude projections of the raw data (top row) and the reconstructed data (bottom row), gained by applying the reconstruction algorithm to the data from the k-wave simulation.*

Of course they were adapted according to the used wavelengths.

The main interest was the effect of changing the beam and sensor configuration on the outcomes of the simulation. The focus was put on acoustic resolution photoacoustic microscopy for the most part, the beams diameter was therefore chosen to be comparatively large.

Before going on to the more specialized simulations, one case shall be presented, showing the overall synergy of the individual parts of the simulation. From this an understanding of the gained information should arise, which is helpful for the other calculations.

3.4.1. Complete simulation

As was already mentioned, in this section a simulation is being discussed, which directly combines the three sub-algorithms (optical, acoustic and reconstruction). This was done by using examples similar to the ones already presented above, using a phantom which resembles real world applications more closely. This phantom consisted of three cylinders,

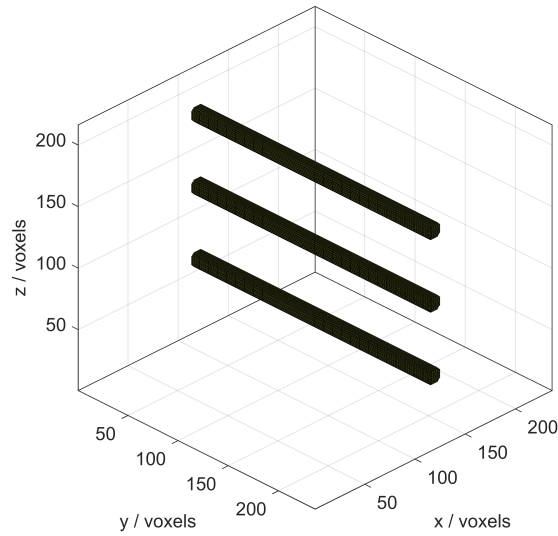


Figure 3.14.: *Three-dimensional depiction of the three cylinders used for the simulation of blood vessels.*

which will also be referred to as tubes, lying above of each other, centered with regard to the excitation beam. A three-dimensional depiction of these tubes can be seen in figure 3.14, it is also visible that the size of the computational domain is $236 \times 236 \times 216$ grid points (without the PML), with a distance of $16.9 \mu\text{m}$ between points.

The properties of the materials used resemble those of liver tissue with blood vessels embedded in it, which in this case are represented by the three tubes. The simulation was run using a beam of 1 mm in diameter and a wavelength of 532 nm, the fluence of the beam was set to be $20 \frac{\text{mJ}}{\text{cm}^2}$, according to the ANSI limit. The respective optical and acoustic parameters for this wavelength can be found in tables 3.2 and 3.3.

This calculation first led to an energy distribution, which can be seen in figure 3.15, where the logarithm of the mean values over ten slices in the x-z plane are depicted. As was expected, the intensity of light goes down drastically with distance. This leads to a large difference in the illumination of the different tubes. Further, the absorbed energy also differs inside of each individual tube. The bottom and outer most layers absorb the most energy, while the inside of each feature absorbs far less photon packets. This is most obvious in the upper tube (at $z = 3 \text{ mm}$), where the inside seems to have absorbed a similar amount of energy as the surrounding material. This effect plays an important role, since the reconstruction does not consider it, yielding reconstructions not exactly resembling the initial sample structure. It is important to note that this is not a shortcoming of the used algorithms but a physical effect. Therefore, this problem also might occur when performing experiments.

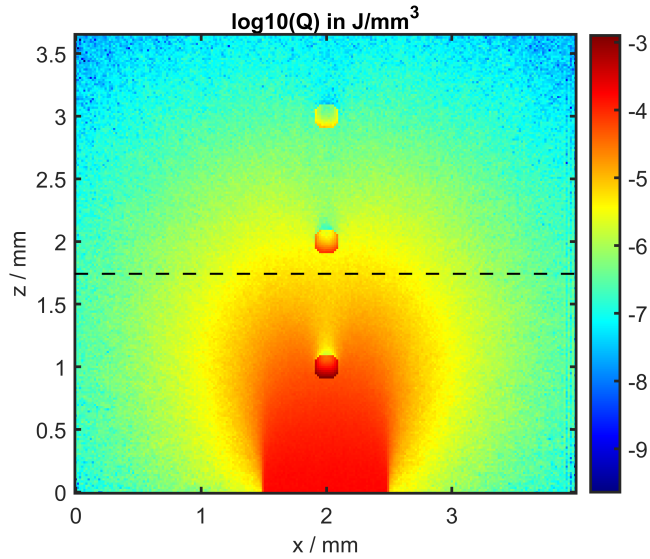


Figure 3.15.: *Logarithm of the absorbed energy Q , for the three cylinder sample, at a wavelength of 532 nm, using a circular beam geometry with a diameter of 1 mm. The dashed line indicates the plane of focus.*

Using this three-dimensional energy distribution and the initial pressure distribution calculated from it, a wave propagation simulation was performed. This was done in a similar fashion to the simulation described in section 3.3.2, using the method of a virtual detector array in the middle of the sample. Once again this can only be seen as an approximation to a real sensor, which would not be able to detect signals from all directions, but it works as a proof of concept, nevertheless.

The results of this simulation can be seen in the top row of figure 3.16. The artifacts present in these raw signals are so severe that it becomes hard to see the cylinders, which were placed inside of the sample initially.

The reconstructed MAPs can be seen in the bottom row of the same figure. The tubes became visible again, although suffering from the artifacts formerly discussed. It is also obvious that the features are only visible where the light from the excitation beam hit them. This means that their full length can not be made out here. In a real world experiment the laser beam would be scanned alongside the sensor, as was discussed in the theory chapter. This would generally solve this problem for AR-PAM but especially for OR-PAM, where the effect is even more severe.

In this depiction only two tubes are visible, since the third one was not lit well enough and was too far from the sensor array to produce a sufficiently large signal.

One further artifact, is the feature below the first tube. This pear-like structure stems from the excitation beam exciting the artificial liver tissue, mainly upon entering the sample.

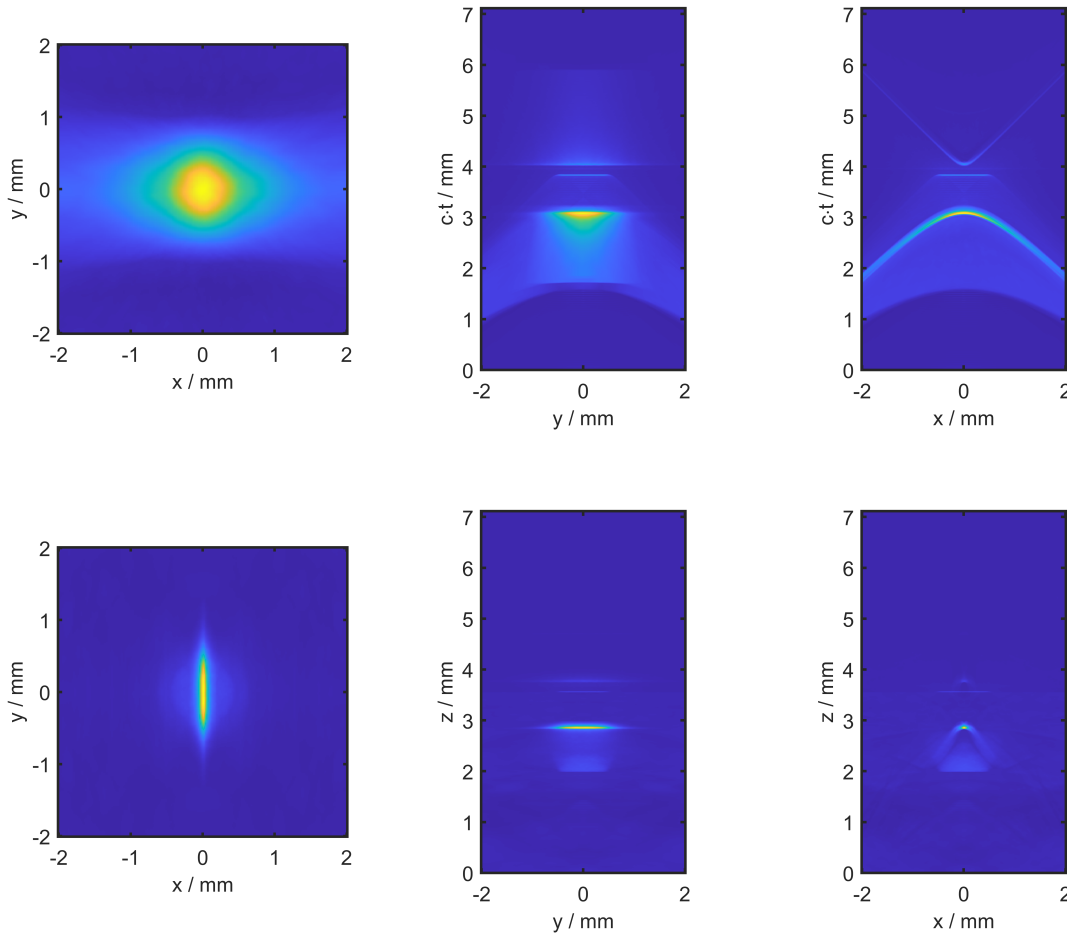


Figure 3.16.: *Maximum amplitude projections of the raw data (top row) and the reconstructed data (bottom row), gained by applying the reconstruction algorithm to the data from the k-wave simulation.*

Overall the simulations returned results which were expected. This shows that, considering the physical parameters gained from literature, an examination of liver tissue with embedded blood vessels should theoretically be possible. Of course the used methods still relied on some crude approximations of an actual setup, mainly due to computational limitations. Therefore, the next step will consist of simulating a focused sensor, which enhances signals coming from certain directions and certain distances.

3.4.2. Focused sensor

Having performed some general simulations, the next step was to look at a simulation resembling a setup that is more closely related to an actual experimental setup. The experimental setup in question was the one also used in some experiments, which will be discussed in the next chapter in detail. The main difference of this setup compared to the calculations performed before, was the focused sensor used in it. The used equipment is closely related to the depiction of the coaxial configuration based on an opto-ultrasound beam combiner shown in figure 2.12.

Although an effort could have been made to simulate this beam combiner fully, this was not done, mainly due to the computational complexity of such a system, which would not justify the benefit of the gained information. Instead the acoustic lens was approximated by a bowl shaped sensor array, having an opening diameter of 6.4 mm, thereby closely approximating the lens used in the real experimental setup. Further, the focus of this artificial lens was set to be 7 mm, by setting the radius of the sphere shaped sensor bowl to this value.

This sensor array was placed inside of a region filled with water, which was assumed to be perfectly homogeneous and non-absorbing for all wavelengths used in the computations. This region of water was coupled directly to the sample in question. This sample was similar to the one used in the last simulations. It consists of three tubes, with a distance of 5 mm, 7 mm and 9 mm to the sensor. The optical and acoustic parameters for both, the liver tissue surrounding the tubes and the tubes, which are made out of blood, can be seen in tables 3.2 and 3.3, respectively.

A visual representation of these tubes, together with the sensor array used in this case, can be seen in figure 3.17, the boarder between the region filled with water and the liver tissue is indicated accordingly, in a blueish gray color.

The computational grid was chosen to have $372 \times 372 \times 372$ grid points, spanning $9.8 \times 9.8 \times 9.8 \text{ mm}^3$, not including the PML.

The goal of this simulation was to show the dependence of one time signal, in other words one A-line, on the used wavelength of the excitation beam. The light propagation simulation was run three times to accomplish this, for 532 nm, 800 nm and 1064 nm. For the simulation with a wavelength of 800 nm the blood tubes where assumed to have been treated with ICG. The results of the calculations for the light propagation are similar to the ones depicted in figure 3.3, which was expected since the parameters used were the same. In this case no reconstruction algorithm had to be applied, since the signals in question were not combined to gain an image but singular A-scans were of interest. These can be compared to looking at the sample at one specific position, without rastering the sensor array.

The results of the simulation are depicted in figure 3.18. They were attained by taking the mean over all pressure signals, coming from the individual point like detectors making up the bowl detector, for each point in time. This was done 1675 times, with a time step of 4 ns, yielding a total recorded time of 6.7 μs .

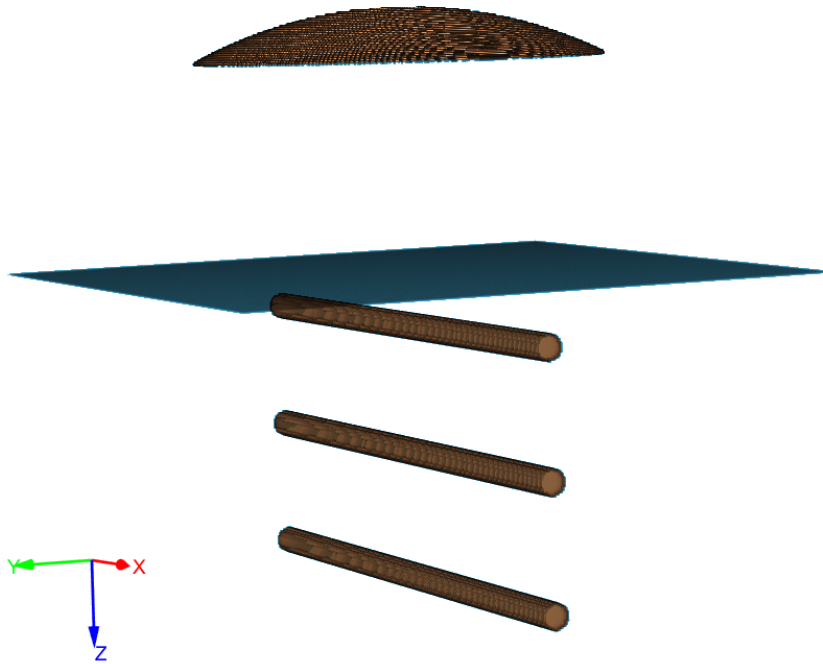


Figure 3.17.: *Three-dimensional depiction of the focused sensor simulation setup, including the bowl shaped sensor, the three tubes and an indication of the boarder between the water-liver interface.*

An analysis of these results reveals the expected outcome of the simulation. Using an approximated speed of sound of around $1500 \frac{\text{m}}{\text{s}}$, one would expect signals to be visible at $3.3 \mu\text{s}$, $4.7 \mu\text{s}$ and $6 \mu\text{s}$, for the three tubes, respectively. In a „perfect“ world these signals would be equal in amplitude, since all three tubes are structured in the same way. This of course can not be expected for the method under discussion, several reasons are responsible for the shape the signals actually took.

Looking at the upper most graph for 532 nm , it can be seen that the first signal actually arrives at the sensor array after around $2.8 \mu\text{s}$. This signal stems from the boarder between the water and liver interface, where the excitation beam first hits an absorbing material. In the case of the wavelength used here, this signal is rather large and therefore care has to be taken to interpret it correctly.

The next signal is roughly positioned at $3.3 \mu\text{s}$ and according to the quick calculation done before and its shape, should stem from the upper most tube in the sample. Its large amplitude can be attributed to the large amount of energy it can absorb due to its position near to the boarder of the sample. This makes it easy to distinguish from the background, even though it does not lie in the focus plane of the detector ($7 \text{ mm} \rightarrow 4.7 \mu\text{s}$).

The tube lying in this focus point is hardly visible, which can mostly be attributed to the amount of light entering these deep regions of the sample. The tube lying the deepest is not visible at all. This can be quite easily explained by the consideration of both the distance from the samples surface and its distance to the focus point of the detector. Both are too large to make this tube visible.

Going on to the signal received from the simulation performed for an excitation beam with a wavelength of 800 nm, one can immediately tell a difference. Since this simulation was run with the parameters provided by using the contrast agent ICG, the signals of the tubes are much higher. This is especially apparent, comparing the signal of the first tube to the signal stemming from the background tissue. When performing the simulation for a wavelength of 532 nm, these signals were roughly equal in height. This problem was mitigated profoundly by taking the longer wavelength and using a contrast agent, which makes the actual signal of interest stand out more.

A further benefit of using this way of measuring the signals is the detection of the second signal, which stands out very clearly in this case. Solely the deepest lying feature is still not visible in this simulation, probably caused by the same reasons as before.

The last simulation, for which an excitation beam with a wavelength of 1064 nm was used, shows some further effects. The difference in absorption between the surrounding material and the features is rather small in this case, which means that the signals of the tubes do not stand out as well as they did for the other wavelengths. This leads to the signal from the first feature melting into the signal gained from the background absorption. The second feature is still visible, better than it was for the simulation with the 532 nm beam but it appears to be elongated. This might be caused by the deeper penetration of the longer wavelength light into the tube itself. The tube gets more fully lit, which in turn lets it appear larger overall. In this case this is beneficial for generating signals that can be reconstructed correctly.

Overall, it can be concluded, that the simulations have supported the claims made by the theoretical description of the problem. Many effects play into the generation of images using photoacoustic techniques and it is important to consider each application individually and choose the used setup accordingly. For example: If high resolution is of utmost importance and the penetration depth is not one of the key interests, a shorter wavelength and a tightly focusing setup are probably best suited for the examination. The exact opposite might be the case, if a large volume has to be studied and the penetration depth therefore becomes a major variable.

Of course every technique has its limits, as was seen in the last simulations. The deepest lying feature was never recorded and therefore would not have been visible in an image either. One could try to tweak the system in a way to change that but most probably would only succeed in doing so by sacrificing something else.

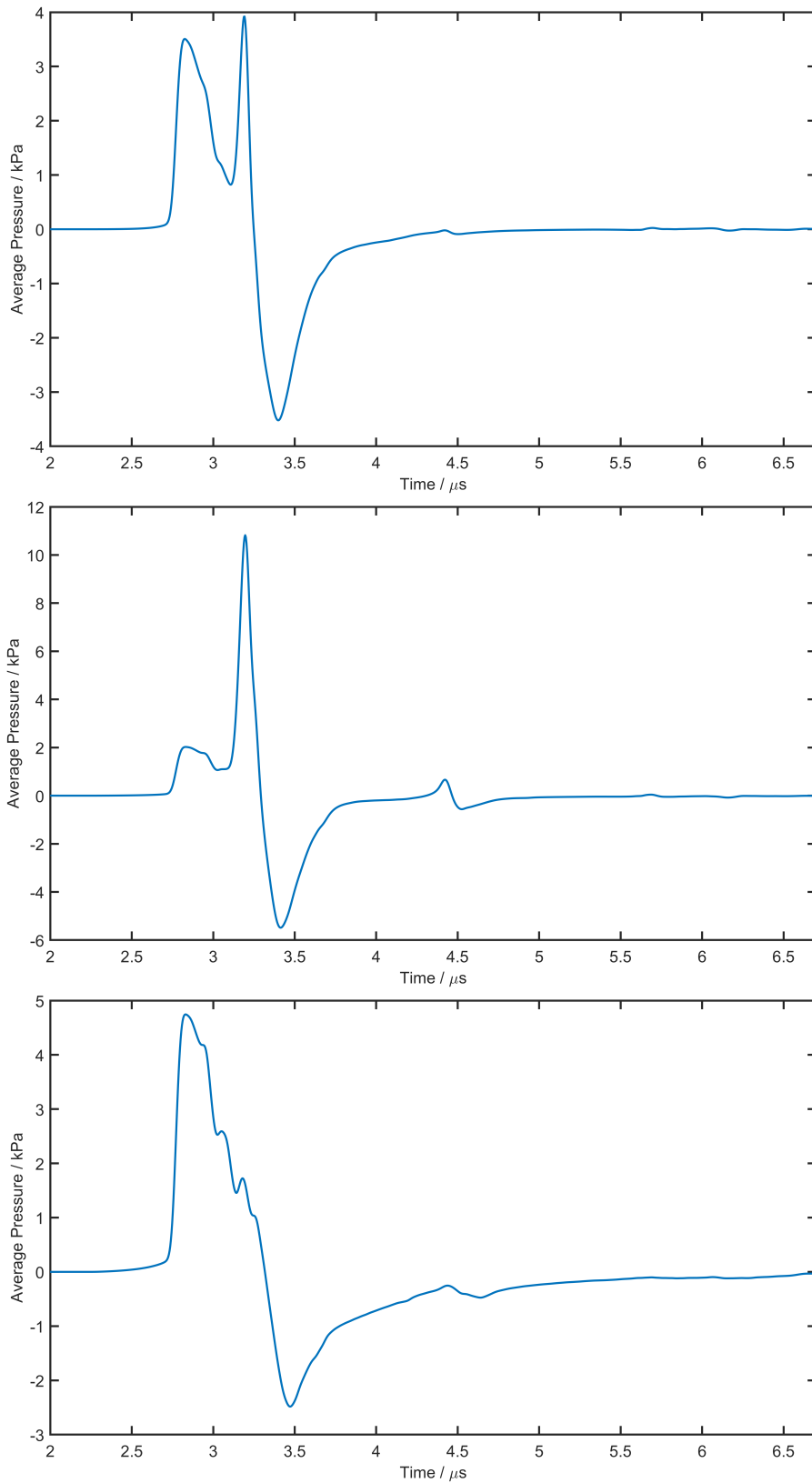


Figure 3.18.: Signals of the focused sensor simulations, 532 nm (top), 800 nm (with ICG, middle) and 1064 nm (bottom).

3.4.3. Depth dependence for planar sensor

After having simulated a focused sensor with several absorbers at once, another look was taken at a similar scenario, now involving a planar sensor replacing the focused one. This was done in order to investigate the dependence of the signals from such a sensor on the position of an absorber, regarding different wavelengths.

First, an absorbent sphere (diameter = 0.5 mm), with the optical and acoustic properties of blood, was embedded inside of a medium with the properties of liver tissue (see table 3.2 and 3.3). The computational grid was $236 \times 236 \times 236$ voxels large (without PML), with dimensions of $8 \times 8 \times 8$ mm³, giving room for a 6×6 mm² planar sensor. The sensor was placed at a distance of 0.5 mm from the liver tissue.

The simulation was run for three wavelengths ($\lambda = \{532 \text{ nm}, 800 \text{ nm}, 1064 \text{ nm}\}$). For each wavelength ten calculations were performed, each with the sphere at a different distance to the sensor, starting with 0.8 mm up to 3.5 mm, in equidistant steps. Once again, for the simulations with a wavelength of 800 nm, the addition of ICG as a contrast agent into the blood sphere was assumed.

In order to compare the signals quantitatively, the ten signals calculated for one wavelength were combined. This was done by taking the maximal value of all the signals at each point in time, thereby highlighting the peaks caused by the respective embedded sphere. The final result of these simulations can be seen in figure 3.19.

First, it is obvious that the pressure amplitude is high enough to be measured with conventional sensors, at least when using 532 nm or 800 nm (ICG) as excitation wavelengths and regarding spheres not too distant from the sensor array. As was already mentioned while looking at other simulations for a wavelength of 1064 nm, these signals are very weak, mainly caused by the low absorption at this wavelength.

Regarding the other two wavelengths another interesting effect was noticed. Taking a look at the peaks of the signals, which are indicated by triangular pointers and represent the positions of the absorbers, the ones for 532 nm are higher in the beginning, meaning that they can be more easily detected. This changes at a distance of approximately 1.7 mm from the sensor, where the amplitude of the peaks is almost equal. Going beyond this depth the peaks for the shorter wavelength vanish, while the ones for the longer wavelength are visible much further along the signal.

It should also be mentioned that there is a wider underlying signal, coming from the absorption of the material the spheres were embedded in. This causes a general background for all signals, especially the drop in intensity at around 3.5 mm can be explained by this.

One can draw the conclusion that the optimal procedure depends on the application. Being interested in very shallow regions of tissue, a short wavelength should probably be considered and no real benefit may be gained by using a contrast agent. This drastically changes when looking into deeper tissue regions, where it is highly beneficial to use longer wavelengths and combining them with contrast agents might become a necessity.

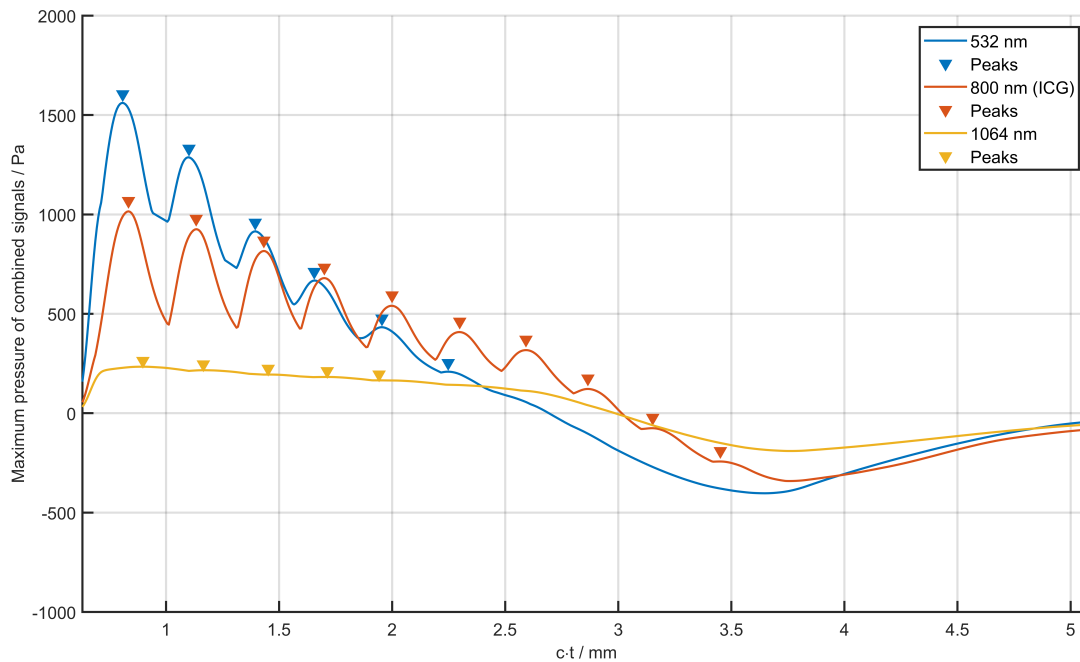


Figure 3.19.: *Depth dependence of pressure signals for a planar sensor for different wavelengths. Triangles indicating the assumed positions of the blood filled spheres.*

3.4.4. Negative contrast

Up to this point only positive contrast was examined. This means that the features, which were embedded into the homogeneous liver tissue, had higher absorption coefficients than their surrounding material. This does not always have to be the case. Sometimes these features exhibit a lower absorption than the surrounding material, this is then referred to as negative contrast.

One example for this is water, which is almost non absorbing, regarding the visible spectrum (1064 nm light is excluded here, since water starts to absorb well in this regime again). Some results of such simulations, using parameters for water instead of blood (no ICG was used here), can be seen in figure 3.20.

Although not nearly as prominent as the positive signals, some negative peaks can be found for absorbers close to the sensor. These do coincide with the positions at which the water spheres were placed inside of the sample. This in turn means that not only highly absorbing features can be imaged using the techniques discussed above but also low absorbing ones. As long as there is sufficient contrast between the surrounding material and the embedded object, a usable signal should be measurable.

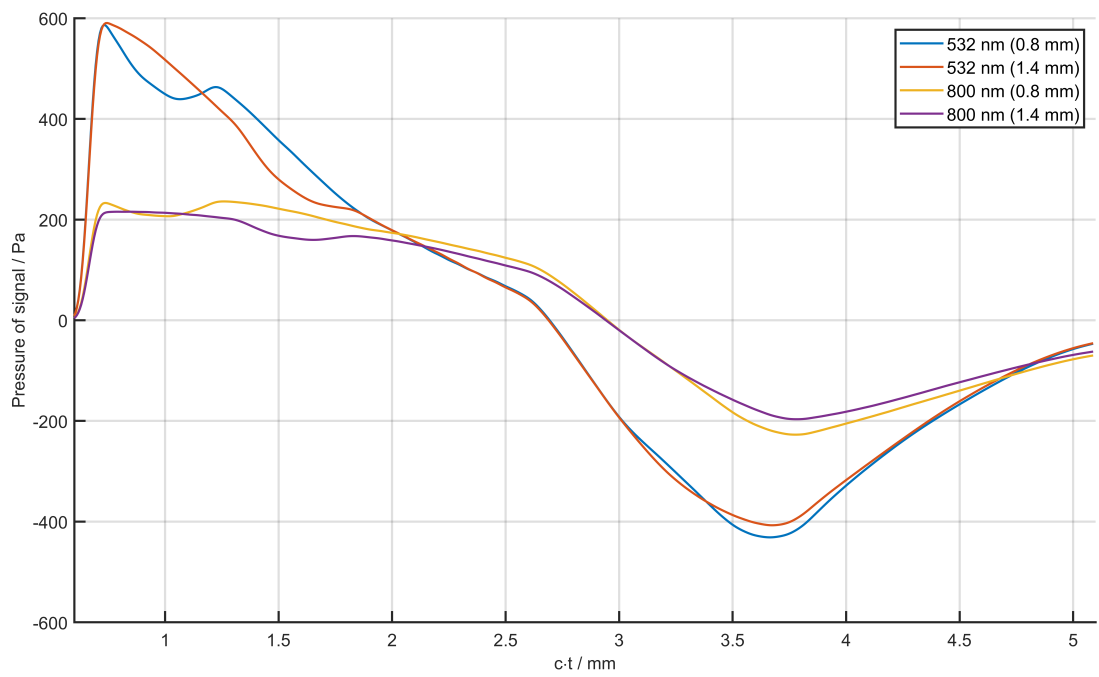


Figure 3.20.: *Depth dependence of pressure signals for a planar sensor with negative contrast for different wavelengths. The values in brackets correspond to the distance of the according absorber to the sensor.*

4. Experimental study of photoacoustic microscopy

The previous chapters mainly were aimed at a theoretical description of the matter at hand and the visualization and confirmation of these theoretical results by simulations. Although the gained insights are already useful, an experimental examination of some of the effects is crucial, since the main purpose of utilizing the underlying physical effects lies in the study of various samples under real world conditions.

As was seen in section 2.5, different experimental setups can be used, each with its own benefits and drawbacks. Caused by the large amount of parameters, choosing the right type of setup for the problem at hand can prove difficult. The first thing that should be discussed in this chapter is the main setup, which was used for recording the signals during the experiments. This setup was based on the idea of a coaxial configuration based on an opto-ultrasound beam combiner, it can be seen in figure 2.12. One of its main benefits is that it can be used for both, AR-PAM and OR-PAM. This makes it very versatile and even allows building a hybrid device, capable of both AR-PAM and OR-PAM [30].

Having talked about the setup and having characterized some of its key parameters, experiments were conducted showing its capabilities in more detail. The thereby generated datasets were examined thoroughly and some of the algorithms described above were used to improve the results.

4.1. Experimental setup

As was already briefly mentioned in the introduction to this chapter, the main setup used for the experiments consisted of a device utilizing an opto-ultrasound beam combiner. A picture of the setup can be seen in figure 4.1. There are two excitation paths, which can be used independently from each other. The one coming from the top utilizes a single mode waveguide ($\varnothing = 3.6 \mu\text{m}$ core diameter) that gets imaged onto the sample via an array of optical elements. This optical path is used when an OR-PAM setup is needed, since the diameter of the laser beam at the sample is way smaller than the focus diameter of the acoustic lens ($\varnothing \approx 100 \mu\text{m}$). In order to use this path the mirror-cube, which can be seen in the center of the setup, has to be removed.

The laser used for this part of the setup is a Laser-export Co. Ltd LCM-DTL-319QT (532 nm) laser. The power of this laser is controlled by neutral density filters. Since this

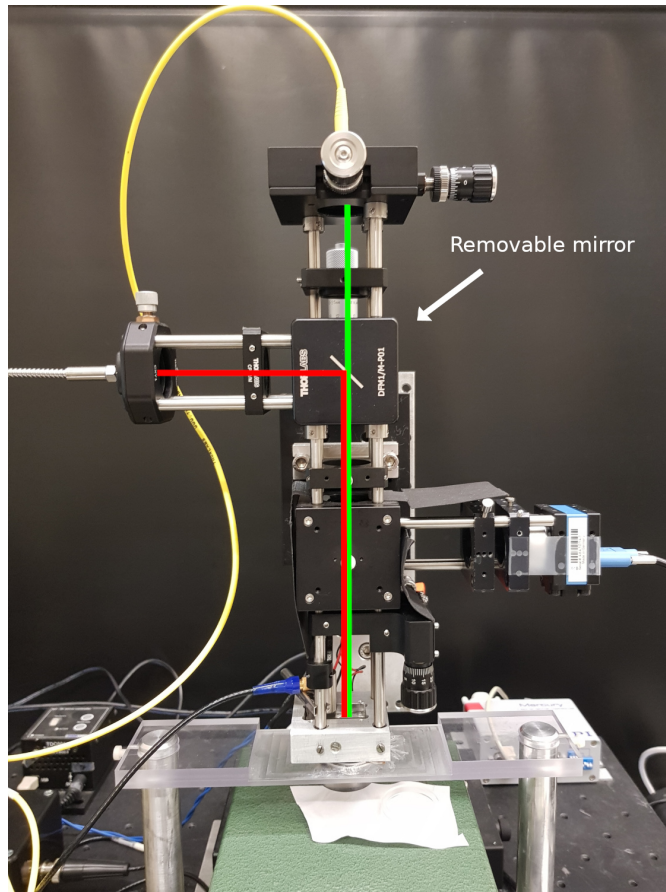


Figure 4.1.: *Picture of the hybrid setup used for the data acquisition. Beam path of the AR-PAM (red) and OR-PAM (green).*

thesis mainly concentrates on AR-PAM, this part of the setup will not be the main area of focus.

The AR-PAM mode of this setup can be described in a similar fashion. The multi-mode optical fiber is brought into the setup from the left side and is deflected downwards by a mirror. Contrary to the single mode fiber, which is assumed to produce a Gaussian-shaped beam profile, it yields a more uniform circular disc profile. The measurement of this profile was done by the knife-edge technique and will be discussed in more detail later on. This optical path was powered by a SpitLight DPSS EVO I OPO laser. This laser has some great advantages over the monochromatic laser used for the OR-PAM mode of this setup, since its wavelength can be adjusted. This allows for wavelength-dependent photoacoustic microscopy, thereby gaining spectral information about the samples.

The setup further incorporates a beam splitter, which allows a camera to be used for taking close up pictures of samples. Further, it would be possible to attach a photo diode to it, measuring the energy for each laser pulse. This is not absolutely necessary for the

AR-PAM setup, since the SpitLight laser has a dedicated energy monitor output.

The most important part of the setup is the beam combiner, which sits in the metal frame of the scan head. A detailed view of this structure can be seen in figure 4.2. Its main purpose is the separation of the ultrasound transducer (Olympus V214-BB-RM 50 MHz) from the laser beam. This is accomplished by combining a prism and a rhombohedron with a layer of index matching liquid between them. This ensures that the laser beam is not altered by this optical element significantly, while the backtraveling sound waves are deflected.

Sound waves generated inside of the sample are spherical longitudinal and get transformed into plane waves by the acoustic lens (45-008 from Edmund Optics). A mode conversion of this longitudinal wave into a transversal wave happens at the first reflection at the boundary between the rhombohedron and the prism. This conversion is reversed by the reflection at the rhombohedron-air interface (the whole path is called *Path A*). There is also a *Path B*, which, as can be seen in the depiction, only contains longitudinal waves. These can not be detected by the ultrasound transducer, since the reflections reduce the signals amplitude by a large amount [57].

The signal generated by the ultrasound transducer is amplified by 48 dB ($2 \times$ Mini-Circuits ZFL-500LN+), in order to be recorded by a Spectrum M3i.4140-exp DAQ. The movement of the scan head is made possible by two independent mechanical stages (x-direction: PI M-605 with C-863 controller and y-direction: Thorlabs MT1-Z8 with TDC001 controller).

The setup depicted in figure 4.1 is operated via a LabView script run in unison with some `Matlab` code on a PC. While the laser used for the OR-PAM is triggered externally by an Arduino, the AR-PAM laser runs freely at 500 Hz. Both lasers provide a trigger output, which is used in order to start the acquisition of a signal at the PC. This is done with a sampling rate of 250 MHz. A delay between this trigger pulse and the actual signal has to be introduced, in order to capture the PA signal. This delay is usually set to 13 μ s, since the time it takes a signal from the focus plane to reach the sensor was estimated to be 14.7 μ s (calculations yielded a value of 14.26 μ s [57]). One A-scan is usually set to be 3.2 μ s long, placing the focus plane roughly in the center of this scan.

Additionally, a value proportional to the energy of each pulse is recorded, which can be done using the energy monitor output of the SpitLight laser. These values can be used to normalize the results, regarding some energy fluctuations of the laser.

The stages moving the scan head are operated by the same script. While the stage moving in the x-direction moves continuously (B-scans), the one moving in the y-direction moves in discrete steps. Considering the free running laser, this movement can cause some deviation in the x-direction between B-scans. It is therefore important to set the stepsize below the achievable resolution, since otherwise these inconsistencies might become visible in the final image.

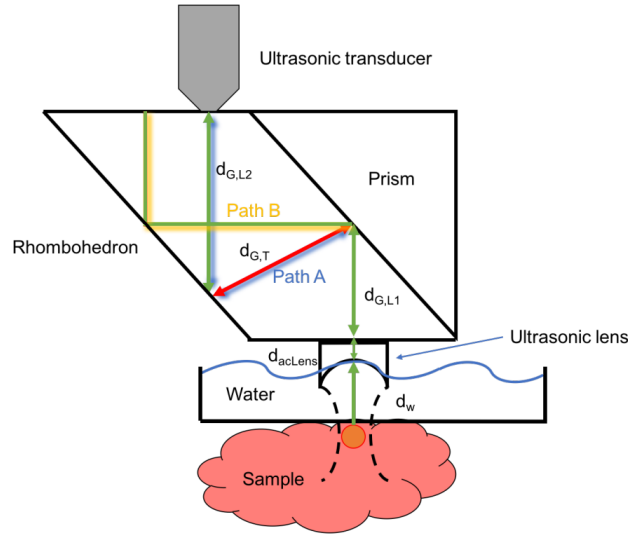


Figure 4.2.: Schematic of the beam combiner, showing the different paths of the ultrasonic waves. Green lines mark longitudinal acoustic waves while red lines mark transversal ones. d_i indicate the distances traveled through different media, where $i \in \{W, acLens, G\}$ stands for water, acoustical lens and glass, respectively [57].

4.1.1. Beam characterization

One very important aspect of the photoacoustic microscopy setup was the laser beam. Its mean power combined with its repetition rate and the focus area are main parameters when determining the fluence hitting the samples surface. This property has to be monitored in order to ensure a harmless operation considering biological materials.

While the repetition rate is given by the laser (500 Hz) for both systems and the power can be adjusted by various optical elements and measured directly by using a power meter (THORLABS PM100A with S120VC sensor), the beams size at the samples surface is not so easily measured. For the AR-PAM setup this can be done using the so-called knife-edge technique. This experiment involves a photo-diode or in the case at hand a power meter and some sort of sharp edge. This sharp edge, a razor blade was used here, is brought into the path of the laser beam and its position is varied, cutting off a smaller and smaller part of the beam. The power of the transmitted light is measured. The values gained by this describe the curve of the integral of the marginal distribution. Since the derivative of such a measured curve is usually very unstable, it was decided to fit the curve directly. This was done assuming that the beam left the optical fiber producing a uniform disc shape, which can be described by the following equation:

$$A \propto r^2 \arccos\left(1 - \frac{x}{r}\right) - (r - x)\sqrt{2rx - x^2} \quad \text{if } x \leq r \quad (4.1)$$

Where A is the area of the beam, r is the radius of the beam and x is the height of the exposed circular segment. For the second half of the circle (i.e., $x > r$) the formula is simply used to subtract the according area from the full circle.

Using this method the data depicted in figure 4.3 was attained. The beam diameter was estimated to be $d = (1.3 \pm 0.1)$ mm.

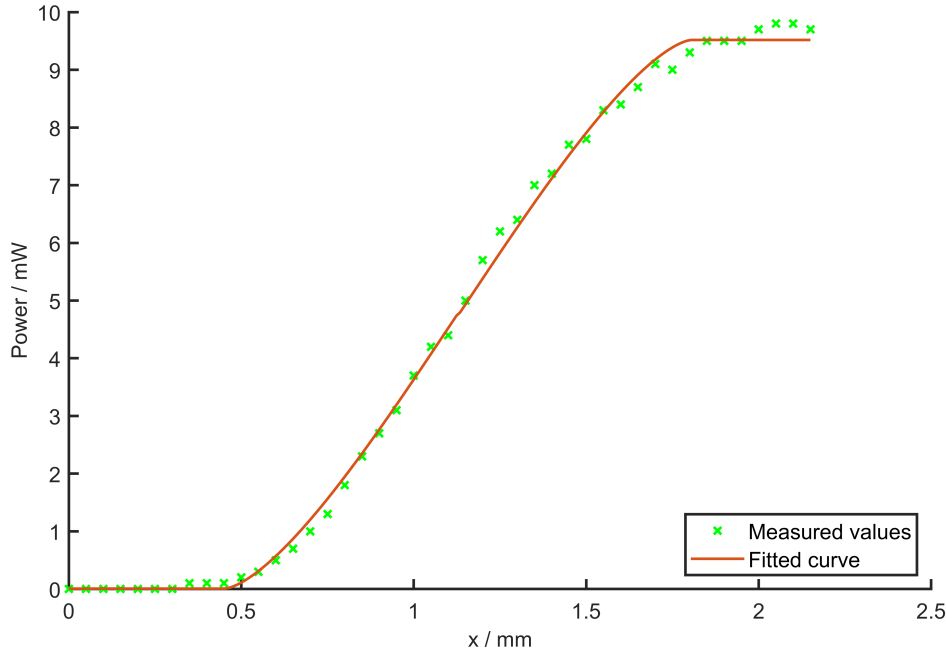


Figure 4.3.: *Fitted curve for determining the lasers beam diameter, gained from scanning the beam over a sharp opaque edge (uncertainties contained within plot markers).*

4.2. Measurements and evaluation

The described setup was used to perform a series of measurements on different samples. Some of these measurements were used for an analytical evaluation of the setups parameters, especially the best achievable resolution by using it. First, a general dataset was captured, which was used to check the function of the setup in principle. Further, some measurements tailored to specific problem sets were captured and analyzed. This helped in gaining an understanding of the fundamental capability of the AR-PAM setup at hand.

This section will be used to discuss all of these measurements and their compliance with the results gained from theory and simulations.

4.2.1. Initial measurement on an artificial leaf

For this first experiment, which can be seen as a proof of concept for the used setup, an artificial leaf made out of a synthetic material was used. This leaf had a net-like structure with the individual fibers being black in color. This meant that the leaf should be absorbing for a large bandwidth in the optical spectrum of light.

For this measurement the laser was set to a wavelength of 500 nm and a stepsize of 20 μm was used for the scanning. If not mentioned otherwise, this stepsize was used for all experiments. An effort was made to place the quasi two-dimensional leaf into the area of focus regarding the acoustic lens, although this was not managed perfectly. The captured area was comparatively large at $6 \times 6 \text{ mm}^2$.

Considering the laser frequency of 500 Hz, such a measurement takes approximately 15 min to finish. This time horizon can pose a problem for living and/or changing samples but was of no concern for this probe.

Considering the repetition rate of the laser (500 Hz) this measurement should theoretically be possible in 3 min (300×300 pulses). There is however some room for improvement, considering that the actual measurement took about five times as long. First, the B-scans are only taken while moving in one direction, which about doubles the total acquisition time. Secondly, the interplay between LabView and Matlab is slow and some plots are generated during the measurement, slowing it down even further. Further, some data is stored in Matlab during the measurement, decreasing the speed even more. Resolving some or all of these issues would clearly be beneficial, especially when working with living samples where natural movement is an issue.

After capturing the raw data, some small improvements were made. First, a small correction for the change in energy of the laser output was considered. The recorded signals were normalized with respect to this oscillating output energy. Secondly, the reconstruction algorithm was applied, although no major improvement was expected to be made by this, since this algorithm mainly benefits three-dimensional structures, which have signals coming from out of focus regions.

Nevertheless, both of these calculations together managed to enhance the final result by a visible amount.

To check the results gained from this measurement an optical microscope (Motic SMZ-171 with Moticam 5.0 MP) was used to capture an image of the leaf additionally. Then a MAP of the final signals gained from the photoacoustic measurement was generated. These two images were compared by superimposing them digitally, the result of which can be seen in figure 4.4.

Although the image coming from the conventional microscope is clearly sharper, which was expected in this case, it can be seen quite clearly that the two techniques result in corresponding images. This leads to the conclusion that, although certainly not being the best method for this special case, the AR-PAM setup yields usable results, which can be confirmed through other methods.

The case at hand could not show the main benefit of PAM compared to conventional microscopy, which lies in its ability to produce sharp images of features in turbid media. An example for a measurement showcasing this ability can be seen in section 4.2.4.

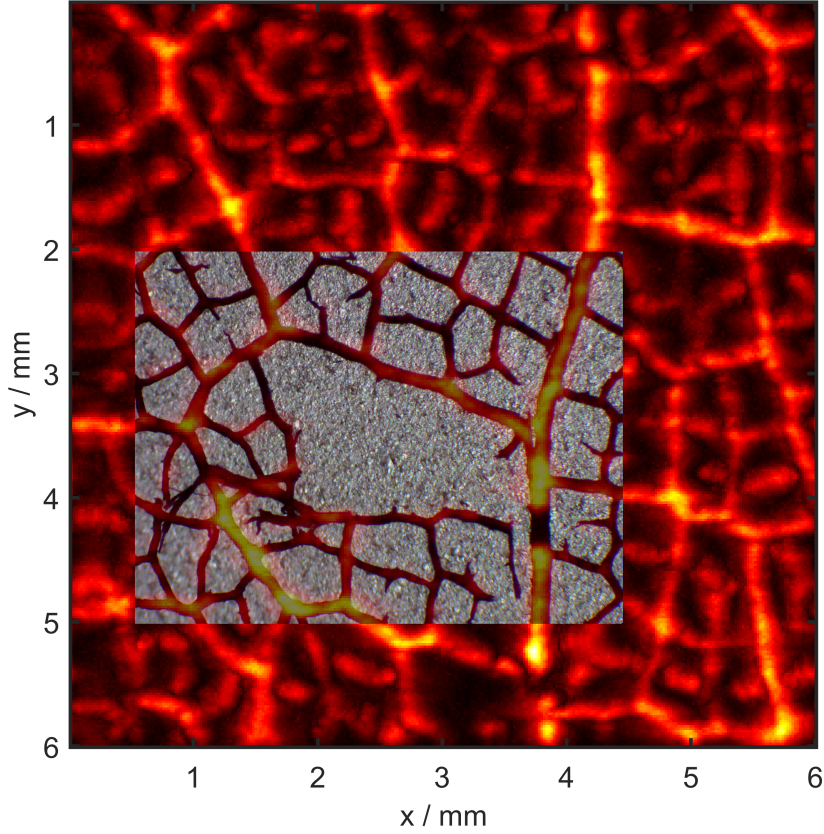


Figure 4.4.: *Superposition of MAP and light-microscope image of an artificial leaf. The background (red to yellow color scheme) being the MAP and the smaller (gray) overlay coming from the light-microscope.*

4.2.2. Resolution characterization

One of the most important parameters of any microscope is its achievable resolution. The theoretical framework behind this, regarding photoacoustic microscopes, was discussed in section 2.5.1. There the spatial lateral resolution of a PAM was mentioned to be calculated by [25]:

$$LR_{AR-PAM} = 0.71 \frac{c_0}{NA_a \cdot f_c} \quad (4.2)$$

Where c_0 is the speed of sound, NA_a is the numerical aperture of the acoustic lens and f_c is the center frequency of the ultrasound transducer. Using this formula and plugging

in the parameters of the used setup ($c_0 = 1500 \frac{\text{m}}{\text{s}}$, $NA_a \approx 0.46$ and $f_c = 50 \text{ MHz}$), one ends up with a theoretically achievable resolution of:

$$LR_{AR-PAM} = 46 \mu\text{m} \quad (4.3)$$

In order to measure the resolution of the setup experimentally the edge-spread function (ESF) was determined. The FWHM of its derivative can then be seen as the best possible resolution [49].

To measure such an ESF a defined target had to be used. In this case a resolution target (Edmund optics USAF 1951) was utilized. Since in theory only one edge was needed, a large feature of this target was chosen to perform the measurement. A MAP of this measurement, after corrections, can be seen in figure 4.5. The experiment was performed using a wavelength of 500 nm and a step-size of 10 μm in each direction. The resolution target was positioned inside of the focal plane.

The MAP shows three distinct stripes, which yields several edges for the evaluation of the measurement. To perform this assessment a profile was chosen at a specific y-position. This profile is depicted in figure 4.6.

To get a good estimate of the actual resolution achievable with the used setup, a part of this profile was fitted with a seventh degree polynomial (`Matlab` function `polyfit`). This is depicted as the black curve in figure 4.6 and approximates the measured values (green dashed line) quite well. This fitted edge is the ESF of the PAM. Being a polynomial one gains the advantage that this function is now analytically differentiable. By this operation one gains the line-spread function (LSF), which in turn can be used to evaluate the final resolution by measuring its FWHM [49]. Most of this derivative is also shown in the figure (red line).

The procedure was repeated several times in order to check for any large inconsistencies within the measured dataset. The achievable resolution was evaluated to be:

$$LR_{AR-PAM} = (100 \pm 10) \mu\text{m} \quad (4.4)$$

This measured resolution differs from the theoretical resolution by a factor of roughly two. Some effort was put into improving this experimentally observed resolution and some enhancement was made, although only after performing the experiments showcased in this thesis. By cleaning the opto-ultrasound beam combiner and realigning the beam path, the resolution was improved to approximately 80 μm . It is assumed that some index matching oil got onto the prism where the sound waves are deflected the second time, thereby indirectly reducing the numerical aperture of the acoustic lens.

In addition to the edge-spread function technique some smaller features of the resolution target were examined. These investigations lead to roughly the same results. Although the resolution in the y-direction is slightly better, the limit approximately lies at the value given above.

To improve this resolution one could either increase the numerical aperture or the detection frequency of the ultrasound detector, as was already mentioned in the theory

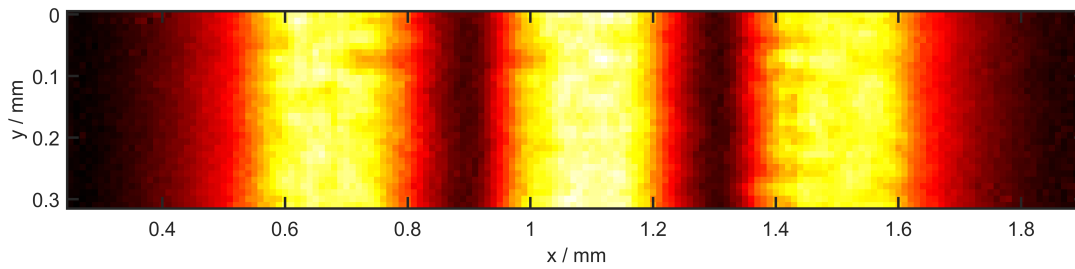


Figure 4.5.: *MAP of a large structure on the resolution target.*

chapter. Both adaptations would come with some drawbacks and do not necessarily post an acceptable solution. Nevertheless, the result lies within a usable range for many applications. If a higher resolution is necessary one might need to use the OR-PAM included in the overall setup.

4.2.3. Evaluation of reconstruction algorithm

After the experimental measurement of the lateral resolution, the reconstruction algorithm, which was described in section 2.6.2, was tested experimentally. The setup was therefore again used to image the resolution target (Edmund optics USAF 1951). For this characterization the sample was measured three times. While the field of view remained roughly the same for all measurements ($6 \times 6 \text{ mm}^2$), the z-position was varied relative to the focus plane. One image was taken as close as possible to the focal plane, another one was taken 1 mm above and one 1 mm below this plane.

This led to three datasets, the one taken in focus was not affected by the artifacts discussed in section 2.6.1, while the other two were. The results of these measurements can be seen in the first row of figure 4.7 in the form of MAPs.

While it can easily be seen that all three images show the same region of the resolution target, the middle one, taken at focal distance, is the clearest image. The picture to the left, taken with the sample above the focal distance, shows distortions similar to the picture to the right, taken with the sample below the focal distance.

Subsequently the reconstruction algorithm was performed on all three datasets, considering a measured speed of sound in water of $1.49 \frac{\text{mm}}{\mu\text{s}}$. The results of these reconstructions are depicted in the second row MAPs in figure 4.7.

While the center image does not show major improvements, the out of focus measurements were improved noticeably. Although slight differences between the three MAPs are still visible, they offer roughly the same amount of detail after the reconstruction. This is exactly what the reconstruction algorithm was programmed to achieve. It was thereby shown, that nearly all the information of a sample can be regained, even for features not lying exactly in the plane of focus.

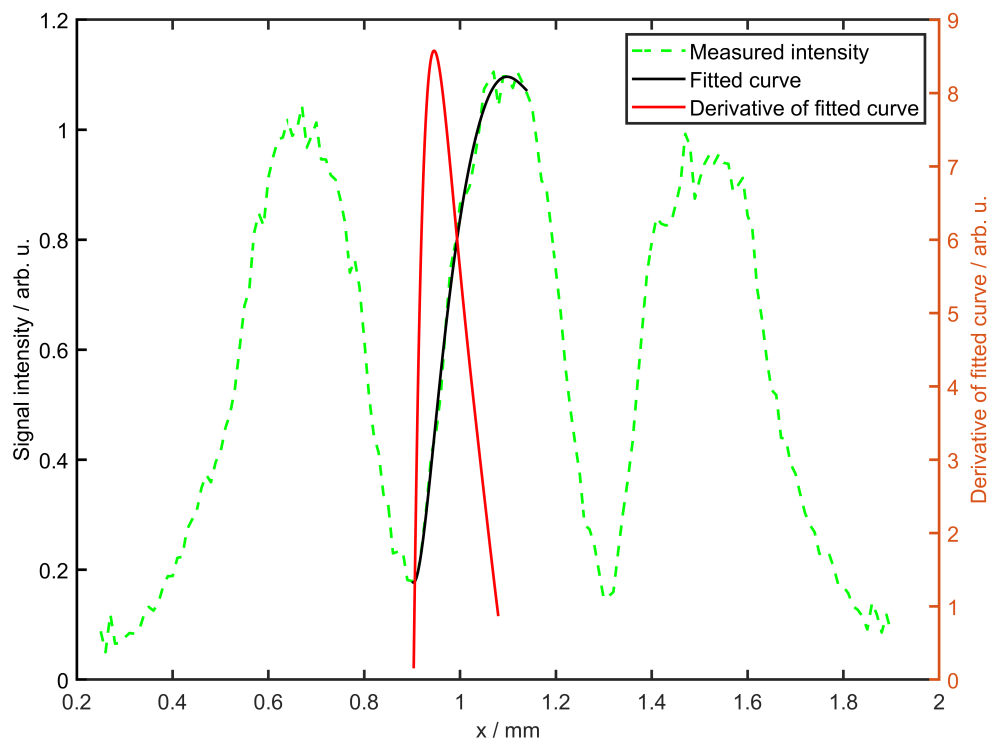


Figure 4.6.: *One profile of the resolution target shown in figure 4.5, with corresponding fit and derivative of that fit.*

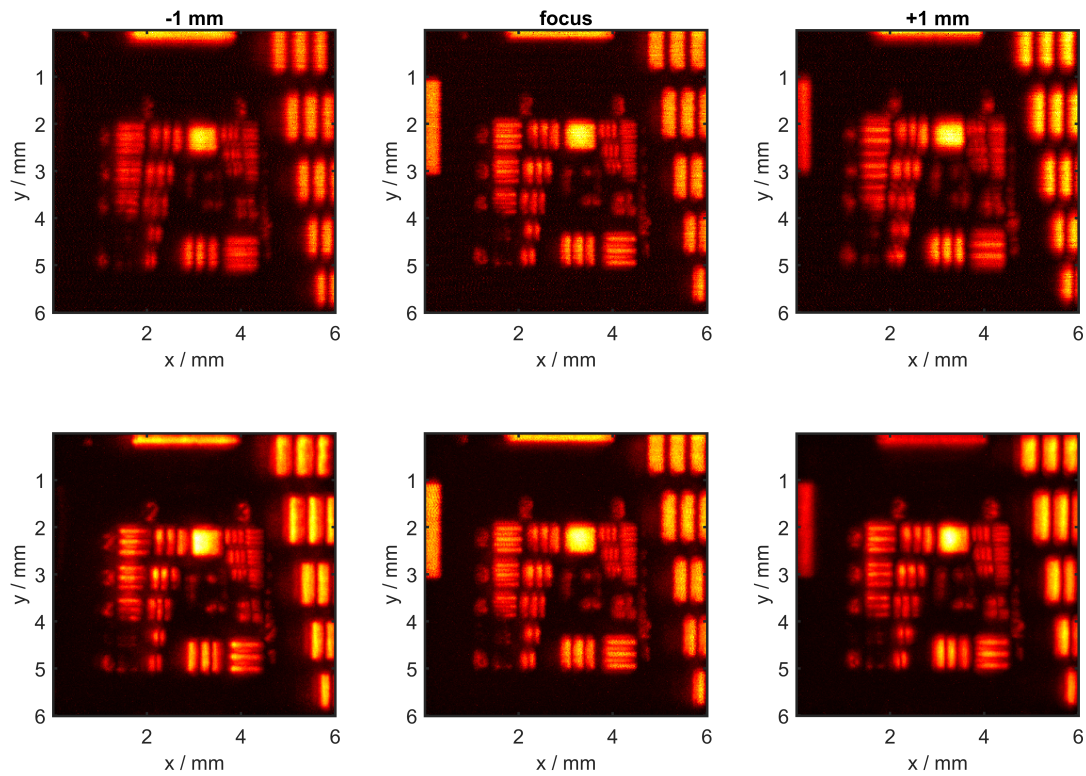


Figure 4.7.: *Comparison of MAPs of a resolution target before (top) and after (bottom) applying the reconstruction algorithm. Sample lying within the focal plane (middle), 1 mm above the focus plane (left) and 1 mm below the focus plane (right).*

4.2.4. Investigation of the multispectral capabilities

As was already mentioned several times, a huge benefit of photoacoustic imaging techniques is the capability to use different wavelengths of light to excite the sample under investigation. The laser system utilized for the setup at hand (SpitLight DPSS EVO I OPO by Innolas) enables the fast switching of this wavelength via an OPO crystal. This was exploited to perform an analysis on a single sample with different wavelengths, in order to show the effect such changes can have on the gained signals.

The sample thus had to be created in a way which made the effect visible. For this purpose several plastic foils of different colors were used (red, green and black). These thick foils were cut into small pieces and embedded into an agarose substrate, which was additionally mixed with an intralipid solution (distilled water with 2% agarose and 2% intralipid solution). In the end this mixture turns into a hard jello. Due to the scattering properties of the lipid emulsion it approximates turbid biological tissues to a certain degree. Experiments performed on this sample did therefore not only show the

effects of different excitation wavelengths but did show the general benefit of working with PAM in turbid media as well. A picture of this sample can be seen in figure 4.8. Although the crossed pieces of plastic foil are visible, it is apparent that a high resolution can probably not be achieved with conventional light microscopes, due to the depth in which the features lie within the sample.

The wavelengths at which the sample was investigated were chosen according to the colors of the foils. The black foil should absorb most of the wavelengths pretty well and can therefore be seen as a control object. The other two features were assumed to be quasi non-absorbent regarding the color they appear in. The outcome of the three measurements can be seen in figure 4.9, except for the wavelength the settings stayed the same for all three measurements.

Performing the measurement at 450 nm all three foil pieces were assumed to provide a signal of some strength. This was indeed the case, as can be seen in the leftmost depiction in figure 4.9.

Using a wavelength of 520 nm, the green foil, going from the top left to the bottom right is still visible but has clearly lost a lot of its intensity, especially compared to the red piece, running from the top straight to the bottom.

This behavior changes drastically when using an excitation wavelength of 620 nm. For this part of the visible spectrum the red feature becomes almost invisible, indicating that it did not absorb the light at all. The green feature on the other hand is highly visible.

Although being a very simple example, this investigation proved that the theory of the spectral properties of materials can be exploited using PAM techniques. As was already mentioned in section 2.5, this for example is being used to distinguish between oxygenated and non-oxygenated blood [49].

Additionally, the results presented in figure 4.9 provide a much clearer image than the photo depicted in figure 4.8. This can be seen as another indication for the benefits of PAM compared to conventional light microscopy. Since the detected sound waves are not influenced by the scattering, the resolution of the images is not affected by adding the intralipid solution to the agarose sample, contrary to the photograph.

4.2.5. In vivo experiments

The final experiments that were conducted for this thesis involved the imaging of human skin. For this purpose the palms of two volunteers were used as samples. This part of the human skin has three advantages, which are beneficial to the measurement regarding the setup used here. First, the hand can easily be placed inside of the microscope in a position allowing the participant to hold still for the duration of the data capture. Secondly, the skin of the palm is comparatively translucent and traversed by many thin blood vessels. Further, there is a low melanin content in the epidermis. This melanin could otherwise block the incoming beam of light and prohibit an adequate measurement.

The wavelength used for these measurement was chosen to be 532 nm. Special care was



Figure 4.8.: *Photograph of the multispectral sample.*

taken to keep the fluence of the beam under the ANSI limit of $20 \frac{\text{mJ}}{\text{cm}^2}$. The highest measured power output lead to a calculated fluency which never reached this value.

One of the main problems for the measurement on living organs is the movement involved with them. In the case at hand this motion had several causes: The pulse and breathing of the participant played a major role but also some inadvertent movements by the participant contributed to unwanted effects.

These discontinuities were mainly visible between individual B-scans and had no visible effect within one singular B-scan. One concern was the correct reconstruction of these datasets. They could not be reconstructed by applying the algorithm discussed in section 2.6.2 for all dimensions. Instead, a similar algorithm was used, only considering two dimensions. In other words, all B-scans were reconstructed independently without influencing one another. This did not resolve the discontinuities between the B-scans but lead to a better result overall.

A representation of the results from the first measurement can be seen in figure 4.10. This MAP image shows some structures which resemble blood vessels, although this can not be said with certainty. Nevertheless, there is a clear contrast within the picture, showing some structures. This at least proves the applicability of the used method to in vivo experiments to some degree.

A further investigation of such a measurement was carried out for the second participant. Looking at figure 4.11, one can see a MAP similar to the one of figure 4.10. The information contained in this MAP image is limited, therefore two B-scans (indicated by the red and green lines) were taken and depicted separately. Looking at these B-scans, one can more clearly see the information gained by performing this measurement. The uppermost layer of the skin is clearly visible at a depth of around 1.5 mm, slanting down

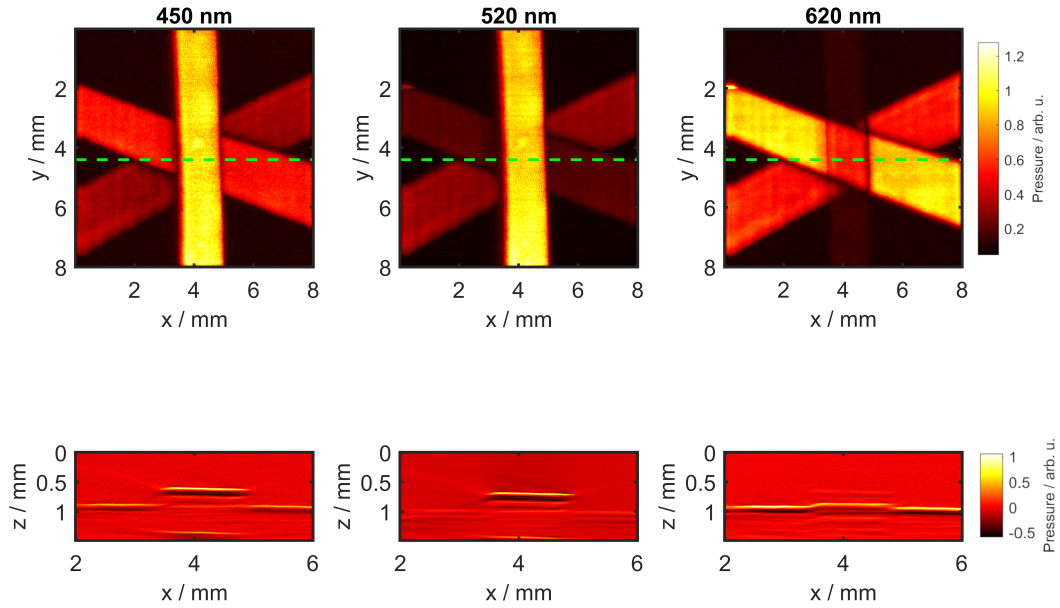


Figure 4.9.: MAPs of the multispectral sample for different excitation wavelengths (top row). 450 nm (left), 520 nm (middle) and 620 nm (right). B-scans corresponding to the green line (bottom row).

slightly to the right side. The signals visible in this part of the image likely stem from melanin inside of the epidermis (for reference see figure 4.12). Looking at deeper layers of the sample, one can again make out very distinct signals coming from a depth of about 2 mm. These signals are more localized and comparing them to the depiction of the structure of human skin, they are most probably caused by blood vessels. Some larger features can be found in yet deeper regions of the skin.

Some effort was put into removing the signal stemming from the epidermis, in order to get a clearer MAP. Although this removal was partly successful, it did not enhance the image quality noticeably.

The in vivo experiments on human skin can be seen as a successful first step into the direction of imaging organs which are to be transplanted. Gaining information of thin blood vessels inside of these organs might prove to be very beneficial to the endeavor of determining and extending the life time of these samples. This plays a critical role in the medical application of the method used during the experimental part of this thesis.

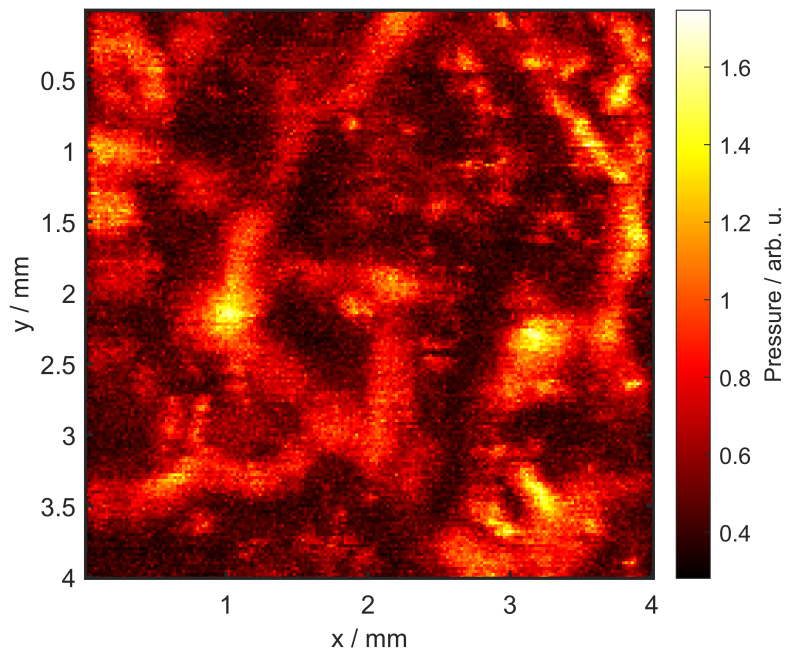


Figure 4.10.: *MAP of an in vivo measurement on a human palm.*

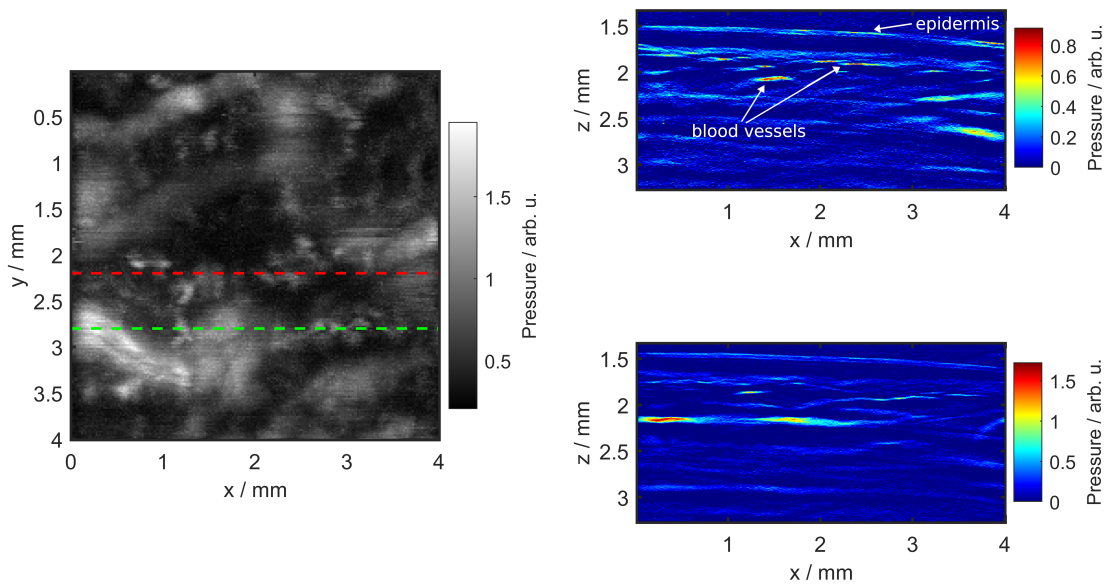


Figure 4.11.: *Map of an in vivo measurement on a human palm (left) with according B-scan images (right; top red, bottom green). The recorded signal intensity is proportional to the initial pressure distribution.*

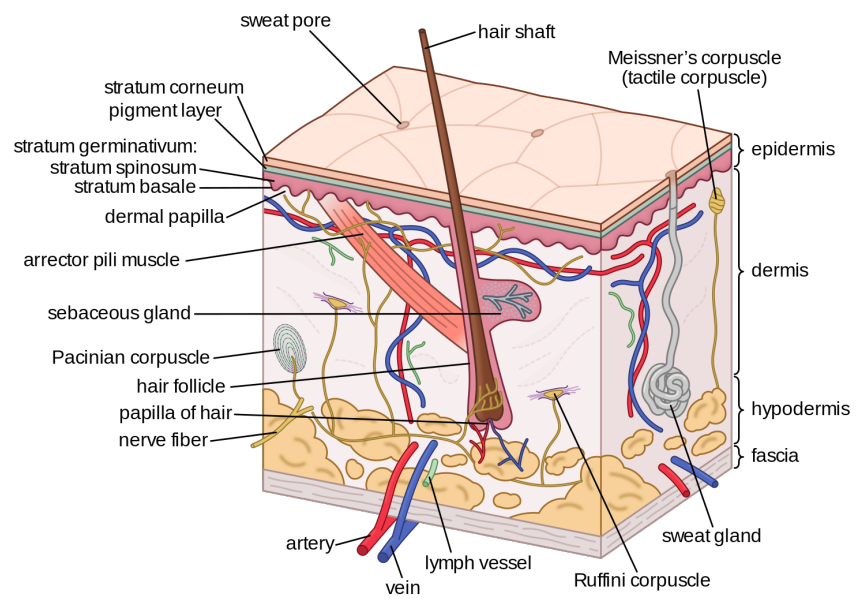


Figure 4.12.: *Schematic of the structure of human skin [58].*

5. Conclusion and outlook

The goal of this thesis was the evaluation of photoacoustic techniques in general, while the focus was put on acoustical resolution photoacoustic microscopy (AR-PAM). The main motivation for these investigations was the possibility to image small structures in biological materials. One use case, which is of special interest, is the monitoring of harvested organs before their transplantation. Using AR-PAM, it is assumed that it is possible to image small blood vessels inside of the liver tissue. This information could then be used to monitor the decay of the liver tissue, giving an indication for the quality of the liver overall.

In order to analyze the problem to its full extent, a thorough look into the theory behind photoacoustics had to be taken. The two main physical effects, the light interaction with turbid media and the wave propagation, were treated individually.

First, the excitation of the sample with intense light beams was discussed. This effect was shown to be essential to the contrast of the method, since different parts of the sample absorb light differently. This also depends highly on the used wavelength, yielding the opportunity to gain spectral information from the measurement.

The simulation of this effect was performed by implementing a Monte-Carlo algorithm. The results of these calculations matched the expected outcomes.

It was then possible to use the results from these Monte-Carlo simulations as an input to the wave propagation simulations. These simulations were based on classical fluid mechanics and were performed using the free-to-use k-wave toolbox. The results of these calculations approximate signals, which would be gained by real measurements. These signals also include some artifacts that are intrinsic to techniques using a focused sensor and a raster scanning approach.

Although there are several ways in which such artifacts could be reconstructed, one specific method, utilizing properties of the Fourier domain, was implemented. This reconstruction algorithm proved to be very efficient and effective for the simulated as well as the experimental signals.

Overall, it was possible to simulate the entire problem by taking the two steps explained above. This enabled a detailed analysis of the proposed theory, especially of the wavelength dependent absorption of the blood vessels inside of the liver tissue. The outcomes of the simulations were in correspondence to the theoretical results.

Finally, some experiments were conducted, checking the theory and the simulated data against some real world investigations. While some of the experiments, for example the analysis of the achievable resolution, deviated from the theoretically achievable mea-

surements by a significant amount, the general results did not refute the theoretical framework. Overall, the conducted experiments confirmed the initial concepts and can be seen as a successful implementation of the method. It can further be stated that the in vivo experiments on human skin provided promising results which hopefully can be translated to a clinical setup easily.

The next steps mainly include a more thorough experimental investigation of samples which approximate a real medical setting more closely. A first step in this direction would be to do measurements on phantoms, including some tubing with different solutions (approximating blood) being pumped through them. While still being well defined, these probes would approximate real organs closely. Going on, experiments on real biological organs with intact blood vessels should be conducted before implementing any setup in a clinical environment.

A. Measurement class

```
1 classdef PAM_mes < handle
2     %PAM_mes Object for one full 3D PAM measurement
3     % This object is used for measurements with a scanning PAM
4     %   setup,
5     %   where every B-Scan is appended to the object one after
6     %   the other.
7     %   It includes the most important properties of the setup,
8     %   at the time
9     %   of the measurement, as well as methods for the
10    %   enhancement of the
11    %   acquired signal and for the reconstruction of the former
12    .
13
14    properties
15        cs % speed of sound [m/s] (standard is cs in tissue)
16        x  % x-vector (measurement points) [length]
17        y  % y-vector (measurement points) [length]
18        z  % z-vector (from sampling rate [time signal]) [length
19        ]
20        time % time-vector (should be convertible to z vector)
21        [time]
22        focus % position of focus point from top [length]
23        energy_mat % matrix of energy values for each pulse [
24        energy]
25        signal_raw % matrix of raw data values
26        signal_imp % signal after some improvement has been
27        done
28        image_rec % reconstructed signals (finished images)
29
30        dimension % structure to store used dimensions in
31
32    end
33
34    %dependent properties
35    properties (Dependent)
36        dx % distance between point in x direction
37        dy % distance between point in y direction
```

```

28         dz % distance between point in z direction
29         dt % conversion of dz into the time domain
30     end
31
32     methods
33         % Creation methods
34         

---


35         function obj = PAM_mes(x, y, z, time, focus, cs,
36             dimension)
37             %PAM_mes Construct an instance of this class
38             % Generally this is only used to initialize the
39             % object, no
40             % signals are saved, since they are appendend
41             % during the
42             % measurement process. Only system parameters are
43             % stored.
44             if nargin < 7 || isempty(dimension)
45                 dimension = struct('length', 'mm', 'time', 'us')
46                 ;
47             end
48             if nargin < 6 || isempty(cs), cs = 1540; end % if
49             % no sos is given use sos in tissue
50             if nargin < 5 || isempty(focus), focus = z(round(end
51                 /2)); end % if no focus is given assume focus in
52             % middle plane
53             obj.x = x;
54             obj.y = y;
55             obj.z = z;
56             obj.time = time;
57             obj.focus = focus;
58             obj.cs = cs;
59             obj.dimension = dimension;
60
61         end
62
63         function append_bscan(obj, bscan)
64             %APPEND_bscan appends one further 2D B-scan to the
65             % raw signal matrix
66             % Used mainly during measurement for filling up
67             % the 3D matrix
68             % with the recorded B-scans.
69             if isempty(obj.signal_raw) % first signal to be
70                 % appended
71                 obj.signal_raw = bscan;

```

```

60     elseif numel(size(obj.signal_raw)) == 2 % second
        signal to be appended
61         new_mat = cat(3, obj.signal_raw, bscan);
62         obj.signal_raw = permute(new_mat, [2,3,1]);
63     else % n-th slice added
64         old_mat = permute(obj.signal_raw, [3,1,2]); %
            change dimensions for concatenation
65         new_mat = cat(3, old_mat, bscan); % concatenate
66         obj.signal_raw = permute(new_mat, [2,3,1]);
67     end
68 end
69
70 function append_energy(obj, energy)
71     %APPEND_ENERGY appends a vector of energy values for
        each pulse
72     %along a bscan. This can be used to correct for
        fluctuations in
73     %the intensity of the beam.
74     if isempty(obj.energy_mat) % first values
75         obj.energy_mat = energy;
76     else % additional vectors
77         obj.energy_mat = [obj.energy_mat;energy];
78     end
79 end
80
81 % Signal improvement


---


82 function improve_en(obj)
83     %IMPROVE_EN uses the stored energy values of the
        laser pulses
84     %to improve the recorded signals; saves them as
        improved
85     %signals since this operation is reversible
86     en_mat = obj.energy_mat./max(obj.energy_mat(:)); %
        normalized energy matrix
87
88     % trying different methods
89     if 1==1
90         % deal with extreme values
91         avg = mean(en_mat(:)); % average value
92         limit = 1*std(en_mat(:)); % limit to where values
            get accepted
93         en_mat(en_mat > avg+limit) = avg+limit; % above
            limit

```

```

94         en_mat(en_mat < avg-limit) = avg-limit; % below
           limit
95     end
96     if 1 == 0
97         en_mat(en_mat < 0.01) = 0.01;
98     end
99     en_mat = repmat(en_mat.',1,1,numel(obj.z)); %
           replicate for right dimensions
100
101     obj.signal_imp = obj.signal_raw./en_mat; % correct
           signals
102     obj.signal_imp = obj.signal_imp./max(obj.signal_imp
           (:)); % normalize corrected signal
103 end
104
105 % Reconstruction methods
           _____
106 % (separate files)
107 fourier3d(obj); % three dimensional fourier
           reconstruction method
108
109 % Dependent properties
           _____
110
111 % get methods for point distances
112 function dx = get.dx(obj)
113     dx = obj.x(2)-obj.x(1);
114 end
115 function dy = get.dy(obj)
116     dy = obj.y(2)-obj.y(1);
117 end
118 function dz = get.dz(obj)
119     dz = obj.z(2)-obj.z(1);
120 end
121 function dt = get.dt(obj)
122     dt = obj.time(2)-obj.time(1);
123 end
124 end
125 end

```

B. Fourier Domain reconstruction algorithm

```
1 %3D-Fourier-Reconstruction from pressure-matrix (signals)
2 function fourier3d(obj)
3 %FOURIER3D calculates a reconstructed image based on a three
4   dimensional
5   %fourier domain based algorithm. It is intended to be used with
6   objects of
7   %the type PAM_mes.
8   tic
9   h = waitbar(0, '3D-Fourier-Reconstruction in progress. Please
10    wait... '); % initialize waitbar
11 %loop over regions (1 - lower, 2 - upper)
12 for region = 1:2
13 %% define signals to use
14 if isempty(obj.signal_imp)
15     sig_mat = obj.signal_raw; % use raw signal
16 else
17     sig_mat = obj.signal_imp; % use improved signal if existent
18 end
19 %% get upper and lower region
20 focInd = floor(obj.focus/obj.dz); % index of focus plane
21 if region == 1
22     signals = sig_mat(:, :, focInd+1:end);
23 else
24     waitbar(1/2) % set waitbar to half finished
25     signals = flip(sig_mat(:, :, 1:focInd), 3);
26 end
27 % clear variable for more space
28 clear sig_mat
29 % Expand data to avoid backconvolution
30 signals = cat(3, signals, flip(signals, 3));
31 [X,Y,Z]=size(signals); % get size of matrix
```

```

32 % apply zero padding
33 if max([X,Y]) < 128
34     SigErw=zeros(128,128,Z);
35     SigErw(end/2-X/2:end/2+X/2-1,end/2-Y/2:end/2+Y/2-1,:)=
        signals;
36 elseif max([X,Y]) < 256
37     SigErw=zeros(256,256,Z);
38     SigErw(end/2-X/2:end/2+X/2-1,end/2-Y/2:end/2+Y/2-1,:)=
        signals;
39 else
40     Nerw=round(1.1*max([X,Y])/2)*2;
41     SigErw=zeros(Nerw,Nerw,Z);
42     SigErw(end/2-X/2:end/2+X/2-1,end/2-Y/2:end/2+Y/2-1,:)=
        signals;
43 end
44
45 % set signals to new matrix
46 signals = SigErw;
47 clear SigErw
48 %% perform Fourier transformation
49 FP = fftshift(fftshift(signals));
50 clear signals % clear variable for more space
51 FI = zeros(size(FP)); % allocate memory FI: Fourier-
    Transformierte des Bildes
52 [XF,YF,ZF] = size(FP); % sizes of fourier domain
53
54 %% define spatial frequency components
55 kxi = 1:XF;
56 kyi = 1:YF;
57 kzi = 1:ZF;
58
59 kx = (kxi-XF/2-1)/(XF*obj.dx);
60 ky = (kyi-YF/2-1)/(YF*obj.dy);
61 kz = (kzi-ZF/2-1)/(ZF*obj.dz);
62 [kx,ky,kz] = meshgrid(kx,ky,kz);
63 %% apply dispersion relation
64 % define new z indices and prefactor
65 w = obj.cs*sign(kz).*(sqrt(kz.^2+kx.^2+ky.^2));
66 wi = round(ZF/2+1+ZF*w*obj.dt);
67 prefakt = 2*kz./w;
68
69 % get logial matrix
70 logi = (wi > 0) + (wi == 0) + (wi < ZF); % only take usefull
    entries

```

```

71 % clear variables for more space
72 clear kx ky kz w
73 logi = (logi - 3) == 0;
74 [KXI, KYI, ~] = meshgrid(kxi, kyi, kzi); % get indices for all
      combinations
75
76 lin_ind = sub2ind(size(FP), KXI(logi), KYI(logi), wi(logi)); %
      get linear indices for indexing w/o loop
77
78 FI(logi) = FP(lin_ind); % fourier image
79 %clear variables for more space
80 clear FP
81 prefakt(~logi) = 1; % only define logi where it is usefull
82 FI = prefakt.*FI; % apply prefactor
83
84 if region == 1
85     waitbar(0.4) % set waitbar to almost finished
86 else
87     waitbar(0.95)
88 end
89
90 if region == 1
91     lower = real(ifftn(ifftshift(FI))); % backtransformation
92     lower = lower(end/2-Y/2:end/2+Y/2-1, end/2-X/2:end/2+X/2-1,
        1:(numel(obj.z)-focInd)); % reduce image size to initial
        image size
93     % clean up everything not needed for next region
94     clearvars -except obj lower h
95 else
96     upper = real(ifftn(ifftshift(FI))); % backtransformation
97     upper = upper(end/2-Y/2:end/2+Y/2-1, end/2-X/2:end/2+X/2-1,
        1:focInd); % reduce image size to initial image size
98 end
99
100 end
101 % put together final reconstruction
102 obj.image_rec = cat(3, flip(upper, 3), lower);
103 obj.image_rec = permute(obj.image_rec, [2, 1, 3]); % right
      direction (change x<=>y)
104
105 waitbar(1)
106 close(h) % close waitbar
107 dur = toc;
108 disp(['The reconstruction took ', num2str(dur), ' s.'])

```


Bibliography

- [1] A. G. Bell, “On the production and reproduction of sound by light,” *American Journal of Science*, vol. s3-20, pp. 305–324, oct 1880.
- [2] D. W. Ball, “Photoacoustic spectroscopy,” *Spectroscopy Online*, 2006.
- [3] P. Beard, “Biomedical photoacoustic imaging,” *Interface Focus*, vol. 1, pp. 602–631, jun 2011.
- [4] R. Nuster, G. Zangerl, M. Haltmeier, and G. Paltauf, “Full field detection in photoacoustic tomography,” *Optics Express*, vol. 18, p. 6288, mar 2010.
- [5] R. Nuster, P. Slezak, and G. Paltauf, “High resolution three-dimensional photoacoustic tomography with ccd-camera based ultrasound detection,” *Biomedical optics express*, vol. 5, no. 8, pp. 2635–2647, 2014.
- [6] G. Paltauf, R. Nuster, and M. Frenz, “Progress in biomedical photoacoustic imaging instrumentation toward clinical application,” *Journal of Applied Physics*, vol. 128, p. 180907, nov 2020.
- [7] S. Chandrasekhar, *Radiative Transfer*. DOVER PUBN INC, 1960.
- [8] G. F. Bassani, *Encyclopedia of condensed matter physics*. Amsterdam: Elsevier, 2007.
- [9] W. Cheong, S. Prahl, and A. Welch, “A review of the optical properties of biological tissues,” *IEEE Journal of Quantum Electronics*, vol. 26, no. 12, pp. 2166–2185, 1990.
- [10] L. Wang, *Biomedical optics : principles and imaging*. Hoboken, N.J: Wiley-Interscience, 2007.
- [11] L. Wang, S. L. Jacques, and L. Zheng, “Mcm1—monte carlo modeling of light transport in multi-layered tissues,” *Computer methods and programs in biomedicine*, vol. 47, no. 2, pp. 131–146, 1995.
- [12] E. S. Benjamin A. Stickler, *Basic Concepts in Computational Physics*. Springer-Verlag GmbH, 2016.
- [13] L. G. Henyey and J. L. Greenstein, “Diffuse radiation in the galaxy,” *The Astrophysical Journal*, vol. 93, pp. 70–83, 1941.
- [14] “Drunkard (computation unit, advanced design studies, the university of tokyo).”

- [15] T. L. Szabo, “Time domain wave equations for lossy media obeying a frequency power law,” *The Journal of the Acoustical Society of America*, vol. 96, no. 1, pp. 491–500, 1994.
- [16] A. D. Pierce, *Acoustics*. Springer-Verlag GmbH, 2019.
- [17] P. Filippi, *Acoustics : basic physics, theory, and methods*. San Diego: Academic Press, 1999.
- [18] B. T. Cox and P. C. Beard, “Fast calculation of pulsed photoacoustic fields in fluids using k-space methods,” *The Journal of the Acoustical Society of America*, vol. 117, pp. 3616–3627, jun 2005.
- [19] B. E. Treeby and B. T. Cox, “k-wave: MATLAB toolbox for the simulation and reconstruction of photoacoustic wave fields,” *Journal of Biomedical Optics*, vol. 15, no. 2, p. 021314, 2010.
- [20] B. Fornberg, “Generation of finite difference formulas on arbitrarily spaced grids,” *Mathematics of Computation*, vol. 51, no. 184, pp. 699–699, 1988.
- [21] M. Tabei, T. D. Mast, and R. C. Waag, “A k-space method for coupled first-order acoustic propagation equations,” *The Journal of the Acoustical Society of America*, vol. 111, pp. 53–63, jan 2002.
- [22] B. T. C. Bradley E. Treeby and J. Jaros, *Manual: k-Wave A MATLAB toolbox for the time domain simulation of acoustic wave fields*, 2016.
- [23] B. Fornberg, “High-order finite differences and the pseudospectral method on staggered grids,” *SIAM Journal on Numerical Analysis*, vol. 27, pp. 904–918, aug 1990.
- [24] J.-P. Berenger, “A perfectly matched layer for the absorption of electromagnetic waves,” *Journal of Computational Physics*, vol. 114, pp. 185–200, oct 1994.
- [25] S. Jeon, J. Kim, D. Lee, J. W. Baik, and C. Kim, “Review on practical photoacoustic microscopy,” *Photoacoustics*, vol. 15, p. 100141, sep 2019.
- [26] J. Yao and L. V. Wang, “Photoacoustic microscopy,” *Laser & Photonics Reviews*, vol. 7, pp. 758–778, jan 2013.
- [27] B. Amos, “Lessons from the history of light microscopy,” *Nature Cell Biology*, vol. 2, pp. E151–E152, aug 2000.
- [28] S. Prahl, “Optical absorption of hemoglobin,” 1999.
- [29] R. L. Shelton and B. E. Applegate, “Off-axis photoacoustic microscopy,” *IEEE Transactions on Biomedical Engineering*, vol. 57, pp. 1835–1838, aug 2010.
- [30] S. Jeon, J. Kim, and C. Kim, “In vivo switchable optical- and acoustic-resolution photoacoustic microscopy,” in *Photons Plus Ultrasound: Imaging and Sensing 2016* (A. A. Oraevsky and L. V. Wang, eds.), SPIE, mar 2016.
- [31] M. Schwarz, *Multispectral Optoacoustic Dermoscopy: Methods and Applications*. PhD thesis, Technische Universität München, 2017.

- [32] J. Y. Kim, C. Lee, K. Park, G. Lim, and C. Kim, “Fast optical-resolution photoacoustic microscopy using a 2-axis water-proofing MEMS scanner,” *Scientific Reports*, vol. 5, jan 2015.
- [33] O. NDT, “What is linear scanning,” 2020.
- [34] M. Vallet, F. Varray, M. A. Kalkhoran, D. Vray, and J. Boutet, “Enhancement of photoacoustic imaging quality by using CMUT technology: Experimental study,” in *2014 IEEE International Ultrasonics Symposium*, IEEE, sep 2014.
- [35] A. Barkefors, “3d synthetic aperture technique for ultrasonic imaging,” 2010.
- [36] J. Park, S. Jeon, J. Meng, L. Song, J. S. Lee, and C. Kim, “Delay-multiply-and-sum-based synthetic aperture focusing in photoacoustic microscopy,” *Journal of Biomedical Optics*, vol. 21, p. 036010, mar 2016.
- [37] L. V. Guimaraes and A. W. Elbern, “Synthetic aperture focusing technique for image restoration,” in *International Symposium on NDT Contribution to the Infrastructure Safety Systems*, vol. 5, 1999.
- [38] H. B. Lim, N. T. T. Nhung, E.-P. Li, and N. D. Thang, “Confocal microwave imaging for breast cancer detection: Delay-multiply-and-sum image reconstruction algorithm,” *IEEE Transactions on Biomedical Engineering*, vol. 55, pp. 1697–1704, jun 2008.
- [39] G. Matrone, A. S. Savoia, G. Caliano, and G. Magenes, “The delay multiply and sum beamforming algorithm in ultrasound b-mode medical imaging,” *IEEE Transactions on Medical Imaging*, vol. 34, pp. 940–949, apr 2015.
- [40] Y. Xu, D. Feng, and L. Wang, “Exact frequency-domain reconstruction for thermoacoustic tomography. i. planar geometry,” *IEEE Transactions on Medical Imaging*, vol. 21, pp. 823–828, jul 2002.
- [41] R. Schulze, G. Zangerl, M. Holotta, D. Meyer, F. Handle, R. Nuster, G. Paltauf, and O. Scherzer, “On the use of frequency-domain reconstruction algorithms for photoacoustic imaging,” *Journal of Biomedical Optics*, vol. 16, no. 8, p. 086002, 2011.
- [42] M. Jaeger, S. Schüpbach, A. Gertsch, M. Kitz, and M. Frenz, “Fourier reconstruction in optoacoustic imaging using truncated regularized inverse k -space interpolation,” *Inverse Problems*, vol. 23, pp. S51–S63, nov 2007.
- [43] F. Spadin, M. Jaeger, R. Nuster, P. Subochev, and M. Frenz, “Quantitative comparison of frequency-domain and delay-and-sum optoacoustic image reconstruction including the effect of coherence factor weighting,” *Photoacoustics*, vol. 17, p. 100149, mar 2020.
- [44] MathWorks, *Matlab Object-Oriented Programming*, 2021.
- [45] S. L. Jacques, “Corrigendum: Optical properties of biological tissues: a review,” *Physics in Medicine and Biology*, vol. 58, pp. 5007–5008, jun 2013.

- [46] I. Carneiro, S. Carvalho, R. Henrique, L. Oliveira, and V. V. Tuchin, “Measurement of optical properties of normal and pathological human liver tissue from deep-UV to NIR,” in *Tissue Optics and Photonics* (Z. Zalevsky, V. V. Tuchin, and W. C. Blondel, eds.), SPIE, apr 2020.
- [47] M. Friebel, A. Roggan, G. Müller, and M. Meinke, “Determination of optical properties of human blood in the spectral range 250 to 1100 nm using monte carlo simulations with hematocrit-dependent effective scattering phase functions,” *Journal of Biomedical Optics*, vol. 11, no. 3, p. 034021, 2006.
- [48] M. L. Landsman, G. Kwant, G. A. Mook, and W. G. Zijlstra, “Light-absorbing properties, stability, and spectral stabilization of indocyanine green,” *Journal of Applied Physiology*, vol. 40, pp. 575–583, apr 1976.
- [49] L. Wang, *Photoacoustic imaging and spectroscopy*. Boca Raton: CRC Press, 2009.
- [50] K. Giering, I. Lamprecht, and O. Minet, “Specific heat capacities of human and animal tissues,” in *Laser-Tissue Interaction and Tissue Optics* (G. P. Delacretaz, R. W. Steiner, L. O. Svaasand, H. Albrecht, and T. H. Meier, eds.), SPIE, jan 1996.
- [51] B. Hill, Ter Haar, *Physical Principles of Medical Ultrasonics*. John Wiley and Sons, 2004.
- [52] B. Soroushian, W. M. Whelan, and M. C. Kolios, “Study of laser-induced thermoelastic deformation of native and coagulated ex-vivo bovine liver tissues for estimating their optical and thermomechanical properties,” *Journal of Biomedical Optics*, vol. 15, no. 6, p. 065002, 2010.
- [53] D.-K. Yao, C. Zhang, K. Maslov, and L. V. Wang, “Photoacoustic measurement of the grüneisen parameter of tissue,” *Journal of Biomedical Optics*, vol. 19, p. 017007, jan 2014.
- [54] C. Sehgal, G. Brown, R. Bahn, and J. Greenleaf, “Measurement and use of acoustic nonlinearity and sound speed to estimate composition of excised livers,” *Ultrasound in Medicine & Biology*, vol. 12, pp. 865–874, nov 1986.
- [55] N. F. Maklad, J. Ophir, and V. Balsara, “Attenuation of ultrasound in normal liver and diffuse liver disease in vivo,” *Ultrasonic Imaging*, vol. 6, pp. 117–125, apr 1984.
- [56] J. Cutnell, *Physics*. Hoboken, NJ: Wiley, 2012.
- [57] F. Taffner, “Grüneisen relaxation photoacoustic microscopy (gr-pam),” Master’s thesis, Karl-Franzens-University of Graz, 2018.
- [58] T. Kebert, “Human skin structure,” 2020.

List of Figures

1.1.	Schematic drawing of Bells photophone	2
1.2.	Maximum amplitude projection of the hind leg of an imaged mouse	3
2.1.	Schematic of the general process used by photoacoustic imaging devices [6].	6
2.2.	Schematic of the general processes happening during the interaction of light with matter.	7
2.3.	Picture of a flashlight shining through a hand.	7
2.4.	Schematic of the geometrical dependence of the deflection angle θ on the scattering event.	10
2.5.	Drunkard problem compared to a simple Monte-Carlo simulation	13
2.6.	Schematic of the photon propagation Monte-Carlo algorithm	14
2.7.	Snapshot of a calculated wavepropagation	17
2.8.	Schematic of the calculation of spatial gradients in one dimension	18
2.9.	Schematic showing the staggered grid for solving differential equations . .	19
2.10.	Graphs showing the behavior of the PML for different thicknesses and absorption coefficients	20
2.11.	Molar extinction coefficient for Hemoglobin dependent on the wavelength of light	22
2.12.	Schematic depictions of different PAM setups	22
2.13.	Schematic depiction of a sample indicating the definitions of A-scan, B-scan, C-scan and L-scan	23
2.14.	Schematic showing the definitions of lateral and axial resolution	24
2.15.	Graphical representation of sensor-feature distance relationship	27
2.16.	Schematic showing the concept of the virtual detector	28
2.17.	AR-PAM images of a mouse leg	29
2.18.	Schematic showing the principle behind the Fourier domain reconstruction algorithm	31
2.19.	Maximum amplitude projections of the optoacoustic signal of gold wires . .	32
3.1.	Graphical representation of a circular beam with an angle of incidence . .	37
3.2.	Positions of photons at the samples surface	38
3.3.	Light simulation results for different wavelengths	42
3.4.	One-dimensional profile of absorbed energy density	43
3.5.	Absorbed light energy for a sample with three spheres	43
3.6.	Schematic overview of the input structures necessary for calculating the wave propagation	47
3.7.	Results of a wave propagation simulation in two spacial dimensions	49

3.8.	Time dependent normalized pressure signal of one distinct point-like sensor	50
3.9.	Experimentally measured pressure signal captured from a highly absorbing sample	51
3.10.	Pressure signal simulated for a spherical initial pressure distribution using a focused sensor	51
3.11.	Fourier spectrum of the simulated signal and used convolution kernel . . .	52
3.12.	Three-dimensional depiction of the four spheres used as pressure sources .	54
3.13.	Comparison of raw data and reconstructed image (without light simulation)	56
3.14.	Three-dimensional depiction of the three cylinders used for the simulation of blood vessels	57
3.15.	Absorbed light energy for three cylinder sample	58
3.16.	Comparison of raw data and reconstructed image (with light simulation) .	59
3.17.	Three-dimensional depiction of the focused sensor simulation setup	61
3.18.	Signals of the focused sensor simulations	63
3.19.	Depth dependence of pressure signals for a planar sensor	65
3.20.	Depth dependence of pressure signals for a planar sensor with negative contrast	66
4.1.	Picture of the hybrid setup used for the data acquisition	68
4.2.	Schematic of the beam combiner setup	70
4.3.	Fitted curve for determining the lasers beam diameter	71
4.4.	Superposition of MAP and light-microscope image of an artificial leaf . . .	73
4.5.	MAP of a large structure on the resolution target	75
4.6.	One profile of the resolution target shown in figure 4.5	76
4.7.	Comparison of MAPs of a resolution target before and after applying the reconstruction algorithm	77
4.8.	Photograph of the multispectral sample	79
4.9.	MAPs of the multispectral sample for different excitation wavelengths . .	80
4.10.	MAP of an in vivo measurement on a human palm	81
4.11.	Map of an in vivo measurement on a human palm with according B-scan images	81
4.12.	Schematic of the structure of human skin	82

List of Tables

3.1. Necessary input values for different beam geometries.	36
3.2. Optical parameters for liver tissue and blood	39
3.3. Acoustic parameters for liver tissue and blood	48